ENERGY DEPENDENT
CHARGE SPREAD FUNCTION
IN A DEDICATED SYNCHROTRON BEAM
pnCCD DETECTOR

DISSERTATION

Zur Erlangung des Grades eines Doktors

Der Naturwissenschaften

Vorgelegt von

Hazem Yousef

Eingereicht beim Fachbereich Physik

Der Universität Siegen

Siegen 2011

Gutachter der Dissertation : Prof. Dr. A.H. Walenta

Datum der Disputation: **20th Mai 2011**

Prüfer: **Prof. Dr. U. Pietsch**

Prof. Dr. H.D. Dahmen

Zusammenfassung

Um die Größe der Elektronenwolke in einem pnCCD-Röntgendetektor auflösen zu können, wurden an der EDR-Beamline des Synchrotrons BESSY II in Berlin mit einem Nadelstrahl die Pixelkanten des Detektors abgetastet.

Der Radius der Elektronenwolke wird in Abhängigkeit von der Photonenenergie und des Einstrahlwinkels des Röntgenstrahls zur Oberfläche des Detektorchips analysiert. Die Messungen werden durch entsprechende numerische Modelle in einer Simulation bestätigt.

Für verschiedene Einstrahlrichtungen ergeben sich aus der Spur der Röntgenstrahlung im Volumen des Detektorchips unterschiedliche Verteilungen der Elektronenwolke über mehrere Pixel. Dazu wurde ein kollimierter Röntgenstrahl der Energie 12,4 keV unter den Eingangswinkeln 30° und 40° benutzt.

Es wird gezeigt, dass die zwei Effekte zur Verbreiterung der Elektronenwolke, Diffusion und elektrostatische Abstoßung, aus den Messdaten separiert werden können. Desweiteren wird beobachtet, dass die elektrostatische Abstoßung die Verbreiterung der Elektronenwolke während der Drift der Elektronen dominiert.

Aus den Daten bei senkrechter Bestrahlung wird der Radius der Elektronenwolke in Abhängigkeit von der Photonenenergie bestimmt. Die Ergebnisse zeigen, dass im Energiebereich von (5,0 - 21,6) keV die Elektronenwolke kleiner als die Pixelgröße von (75 * 75) μm^2 ist.

Abstract

A scan on the pixel edges is the method which is used to resolve the electron cloud size in the pixel array of the pnCCD detector. The EDR synchrotron radiation in BESSY is the source of the X-ray photons which are used in the scans. The radius of the electron cloud as a function of the impinging photon energy is analyzed. The angle of incidence of the X-ray beam is employed in the measurements. The measurements are validated by the numerical simulation models.

The inclined X-ray track leads to distribute the electron clouds in a certain number of pixels according to the incident angle of the X-ray beam. The pixels detect different electron clouds according to their generation position in the detector bulk. A collimated X-ray beam of 12.14 keV is used in the measurements with 30° and 40° entrance angles. It is shown that the two factors that leads to expand the electron clouds namely the diffusion and the mutual electrostatic repulsion can be separated from the measured electron clouds. It is noticed as well that the influence of the mutual electrostatic repulsion dominates the cloud expansion over the diffusion process in the collection time of the detector.

The perpendicular X-ray track leads to determine the average radius of the electron cloud per photon energy. The results show that the size of the electron clouds (RMS) in the energy range of [5.0-21.6] keV is smaller than the pixel size.

Contents

Zusammenfassung I
Abstract II
Contents III
Introduction VI
1. The pnCCD Structure: Device and Readout Design 1
A. The pnCCD Architecture 2
A.1- The Design of the Register Side 3
A.2- The Metal Insulator Semiconductor structure (MIS) 4
A.3- The back side and the substrate of the detector 5
A.4- Single Register Storage 6
A.5 Frame-Store Scheme of the pnCCD Array 7
B. The Readout Process and the associated electronics 7
B.1- Three Phase Charge Transfer Mechanism 9
B.2- The Front- End Electronics 10
B.3- The CAMEX Chip 11
C. Related Semiconductor Physics Relations 12
C.1 The Reverse Bias PN Junction and the Depletion Voltage 13
C.2- The Metal-Oxide Semiconductor Capacitor 17
D. The Potential Profile in the Silicon Substrate 21
2. Characterization and Operational Parameters of the pnCCD 23
A. Attenuation of Photon Beam in Silicon 23
B. The Position Resolution and Charge Sharing 24
C. Energy Resolution 29
D. The Quantum Efficiency 29
E. Leakage Current and Readout Noise 30
F. Common Mode Noise 30

G. Charge Transfer Noise 31

H. Pile-up Events.. 31

I. Parallax Effect.. 32

3. Theoretical Computation and Expectations 34

A. The Detection of the X-rays 34

B. The Computation Process.. 36

C. Charge Collection Time 37

D. Charge Cloud Expansion.. 40

D.1-Primary Charge Cloud Size.. 40

D.2- The Diffusion Process as a Random Walk 40

D.3- Mutual Electrostatic Repulsion.. 42

E. Numerical Model of the Charge Spread 43

F. Expectations from the Numerical Model.. 45

F.1- The Scan Profile for Perpendicular Incoming Beam 48

F.1- Statistical Fluctuations in the Calculated RMS Resolution 49

F.2- Inclined Track of the Incoming X-ray Beam 51

4. Experimental Set-up and Data Handling 55

A. The Objective of the Experiment.. 55

B. The Experimental Technique.. 55

C. The Edge Profiles.. 58

D. Data Handling and Correction Procedure 59

D-1 Offset and Noise Maps.. 59

D-2 Noise Map 60

D-3 Common Mode Noise.. 61

D-4 Gain and Charge Transfer Inefficiency (CTI) 62

5. Measurements and Results.. 63

A. X-ray Spectra and Energy Resolution.. 65

B. Inclined X-ray Beam Track 69

B-1 Measurement with 40° Inclined X-ray Beam 70
B-2 Measurement with 30° Inclined X-ray Beam 77
C. Perpendicular Beam Incidence: Charge Cloud Size as a Function of Photon Energy 81
D. Experimental Challenges 88
C.1- Off Center Hit 88
C.2- Charge Cloud Size for the Piled up Photons 91
6. Conclusions and Outlook 92
References 95
Acknowledgments 97
Curriculum Vitae .... **Error! Bookmark not defined.**

Introduction

Further development of semiconductor detectors and systems are required for experiments with the synchrotron radiation. The high photon rate which is delivered by the synchrotron source requires a detector that is less damaged to the radiation and has high quantum efficiency. A high time resolution of the readout system is essential in order to cope with the high flux.

Fully depleted and back illuminated pnCCD detector is a semiconductor pixelated detector. The pnCCD expands its initial application in astrophysics into a detector suitable for synchrotron radiation related applications. The fast timing characteristics, the resistance to radiation damage and the superior energy resolution are the properties of the detector. Moreover, the position resolution is obtained through the CCD structure since the register side of the detector is a two dimensional array of a defined pixel size.

The detector's wafer thickness is $450\mu m$ and the pixel size is $75\mu m * 75\mu m$. It is useful for X-ray detection in the energy range from 0.1 keV up to 30 keV.

Crystallographic studies and medical imaging application are the objectives of our research. They demand for a detector such as the pnCCD that is able to resolve the incoming dispersive photons and to address their interaction positions simultaneously.

The detector is a multi-parameters system that is optimized to faithfully reproduce images in its array. Being a semiconductor detector, the interaction of photons with the silicon substrate produces an amount of electron-hole pairs that is proportional to the deposited photon energy. The photoelectric effect is the dominant interaction process of the X-ray with the detector. The high electric field which is applied on the detector separates immediately the electrons from the holes. The electrons, which are the majority carriers, drift to the register side and collected there within a defined collection time.

Since the generated electron cloud is point-like, the point spread function (PSF) is the measuring approach that is used to resolve the size of the electron cloud. The PSF in the detector is influenced by:

- Pixel size
- Readout structure
- Charge collection process

The experimental technique proceeds utilizing a pixel scan via a pinhole collimator aligned parallel to the detector's entrance window. When the scan starts from the center of the pixel, the amount of collected

electrons will monotonically decrease in this pixel as the scan progresses toward the pixel's edge and simultaneously increases in the next pixel. Analyzing the slope of the efficiency curves at the edge leads to determine the size of the electron cloud provided no electron loss at the edge between the pixels.

The numerical simulation provides a physical model for understanding the charge collection process according to the detector configuration and its optimized parameters. The primary size of the electron cloud expands to some extent during the collection time. The main reasons for the expansion are the diffusion of the electrons and the mutual electrostatic repulsion. Since the expansion due to the diffusion process is proportional to the $\sqrt{t}$ and the mutual repulsion to the $\sqrt[3]{t}$, the dynamic expansion is treated in the model by taking the root mean square (RMS) radius which is updated every picoseconds time interval up to the total collection time.

Two different models are encoded according to the incident angle of the X-ray beam. The incident angle together with the radius of the electron clouds will define the spatial distribution of the electron cloud in the pixel array.

Finally, the results of the measurements should quantify the spatial response of the detector as a function of the photon energy and they should verify the simulation models. This can be useful for smaller pixel design and further detector development. For image processing, sub-pixel resolution analysis can be considered to enhance the fine structure in the detected images. On the other hand, the simulation models can be used as a spatial deconvolution kernel in the images to obtain the original size of object or to correct for the parallax effect which may occur in the detected images. This is important for experiments such as the Laue experiment since the Laue spots that should reflect the cross section of the sample crystals is enlarged when projected into the detector by the detector's spatial response (PSF).

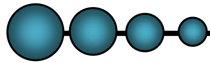

1. The pnCCD Structure: Device and Readout Design

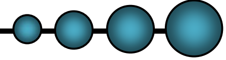

This chapter introduces the pnCCD detector as a new configuration for the known charge-coupled device. The detector architecture and its associated readout electronics will be presented. The operation of the detector and the electrical properties are discussed.

Silicon is the material used in the pnCCD detector. Intrinsic silicon has a crystal structure where a gap separates the conduction band from the filled valance band. The separation gap forms a forbidden band of 1.1 eV. When the electrons in the valance band have energy that is sufficient to cross the forbidden band and reach the conduction band the so called electron-hole pair is created. Two types of currents can be viewed if an electric field is applied across the silicon. *The electron current*; which results from the movement of the free electron in the conduction band in a direction opposite to the electric field lines. The vacancies that are left behind the ejected electrons are filled with other valance electrons. The movement of the valance electrons to fill the holes can be imagined as if the holes are moving parallel to the direction of the electric field lines.

In order to increase the number of the carriers in the current, impurity atoms can be added to the pure silicon. The n-type silicon is a semiconductor material with an increased number of conduction-band electrons as a consequence of adding impurity atoms (e.g. phosphorus) to the pure silicon. The electrons are called the majority carriers in the n-type material and the holes are the minority carriers. If the number of holes is increased in the pure silicon, the p-type silicon material is created with holes being the majority carriers and the electrons are the minority carriers.

Electrons are the majority carriers in the pnCCD detector. Table 1-1 shows the values of the doping concentration for the silicon materials in the pnCCD detector in use [ref.12].

Table1-1: Doping type and concentration values for the pnCCD device

Doping Type	Acronym	Value (cm^{-3})	Used in
High Acceptor concentration [P^{+}]	N_A	$1 * 10^{18}$	Back & Registers Sides
Low donor concentration [n^{-}]	$N_{D_}$	$6 * 10^{11}$	Detector Bulk
High donor concentration [n^{+}]	N_{D_+}	$1 * 10^{14}$	Epitaxial layer& Anode

A. The pnCCD Architecture

The concept of the charge-coupled device (CCD) as a discrete-sampling semiconductor imaging device implies using analog registration for the signal electrons which result from the interaction of the X-ray with the silicon atoms in the detector bulk by storing them in a potential well, and consequentially shift the electron packets in a predetermined path via a defined clock pulses. The fully depleted pnCCD has been designed and fabricated by the semiconductor laboratory of Max Planck Institute (MPI-Halbleiterlabor) for the purpose of X-ray detection in the energy range from 0.1 keV to 30 keV. It is based on the principle of a double-sided wafer process on high purity n-type silicon. A highly doped p-type silicon (N_A) is implanted on a homogenous and weakly doped high resistivity n-type silicon substrate ($N_{D_}$). The total thickness of the wafer is 450µm. The wafer side that is considered to be the entrance window for the X-ray beam, the *back side*, has "unstructured" p^+ type implantation. The *registers side* (*front side)* is the other side of the silicon wafer that has "structured" p^+ -type material which forms the pixel array of the detector [ref.1]. Therefore, the pnCCD substrate can be configured as shown in figure 1-1 by the register-side structure, epitaxial layer, bulk substrate and back-side implant.

The function of the pnCCD is based on the novel scheme of the charge transport in fully depleted semiconductor detector proposed by Gatti and Rehak for the design of the silicon drift detector [ref. 2].

The application of a high negative voltage on the large area rectifying p^+ back contact and low negative voltage to the p^+ transfer gates, both relative to the anode (positive voltage), operates the pnCCD detector in a reverse bias mode. In this way, a full depletion of the detector substrate is achieved. By adjusting the bias voltages, the potential minimum can be shifted close to the register side and can be confined inside the epitaxial layer which has thickness of maximum 10 µm and high doping concentration (N_{D_+}).

The pnCCD is then a pixelated silicon detector which is entirely sensitive to the radiation due to the full depletion feature. Its quantum efficiency is high being semiconductor material and the substantial

thickness. The thin entrance window makes possible the detection of soft X-ray photons. The beam hardening capability is due to the fact that the charge packets are confined in a depth of maximum $10\mu m$ from the registers and the quick transfer within this depth to the readout anode. This will reduce the contribution of the MOS structure in causing damage resulting from the accumulation of the charge on the front surface. These features are described in the following sections as thoroughly explained in [1, 3 &4].

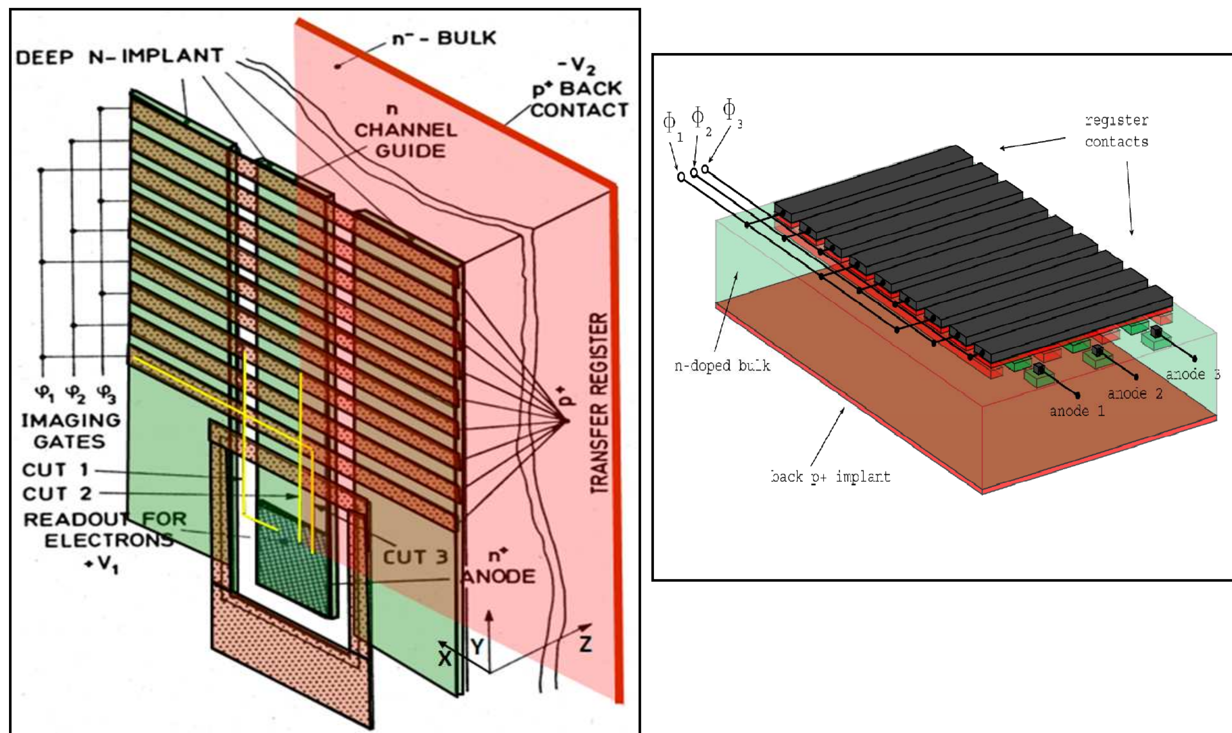

Fig.1-1: Perspective view of a schematically drawn pnCCD

A.1- The Design of the Register Side

Figure 1-1(left) shows a schematic drawing of the pnCCD with the striped structured side composing the register side. In this side, strongly concentrated p-doped silicon (N_A) stripes with silicon oxide in between (SiO_2) are forming the front face of the device. Aluminized contact is covering the upper side of the p^+ stripes as depicted in Fig 1-1(right). Perpendicular implant of deep n-channel (n^+) under the p^+ transfer register and under the SiO_2 insulator constitutes a *guiding channel* for the signal electrons (cut2). The guiding channel implant has phosphorus dopant concentration (N_{D_+}) relative to that concentration in the silicon bulk (N_{D-}). The *channel stop* in the configuration is the absence of this deep n-implantation (cut1) between two neighboring channel guides. Each channel guide ends up with n^+ anode which is in turn connected to a JFET transistor as the first amplifier (First FET). A guard-ring contact with negative

potential surrounds the anode in order to insulate it from the pixel structure and the surrounding silicon substrate.

The advantage of the deep n^+ implantation (epitaxial layer implantation) under the P^+ shift electrodes is to prevent the injection of thermally generated holes into the P^+ back contact and to form a guiding channel for the signal charges.

On the other hand, it is known that the absence of the deep n-implantation provides a potential barrier for lateral spreading of the electrons between two channels guides. Therefore, the width of the channel stop must be large enough to ensure the electrical separation of the neighboring channels, and it must be small enough to reduce punch-through current as much as possible. A gap width of 3 to 5 μm between the neighboring guiding channels would fulfill the above requirements and makes possible creating a potential barriers thus confining the signal charges within the channel guide area.

The potential barrier between the guiding channels works such that the positive donor ions of the n-channel guides attract signal electrons while the negative acceptor ions of the p-channel stops repel the signal electrons.

The pnCCD pixel array can be viewed in cut2 versus cut 3 in Fig.1-1(left). The column of this array represents the charge transfer direction as moving through the channel guide perpendicular to the transfer register reaching the n^+ anode. On the other hand, the row is illustrated with cut 3 as moving through the channel stop parallel to the transfer registers.

Each pixel then can be seen as a set of p-doped ion implant, oxide layer and aluminum contact Fig (1-2). Being a three phase pixel detector, three transfer registers are required to operate one pixel. Provided this pixel structure and the voltages applied on its components, the potential well is delineated along the charge transfer direction with the registers' potentials and in the row direction with the potential barrier of the channel stops. The maximum depth is held within the epitaxial layer thickness ($10\ \mu m$) due to the potential minimum at the interface with the n^- bulk.

A.2- The Metal Insulator Semiconductor structure (MIS)

The MIS component in the pnCCD front side structure is formed by the metal aluminum plate, the oxide layer as an insulator and the n-doped substrate of the detector. The MIS structure works as a capacitor.The thermal electrons generated from the surface defects during the growth of the silicon oxide layer are attracted by the capacitor and thus they will not reach the signal electrons in the potential well. In addition and reference to the device simulation described in reference [1], the additional creation of the

positive SiO_2 interface state will not deteriorate the operation of the pnCCD but will improve the insulation between the P^+ registers due to the implantation of the channel guides. The physical behavior of the MIS capacitor is described in section C.4 of this chapter.

A.3- The back side and the substrate of the detector

The cross section through the channel guide along the Z- direction (cut 2 in Fig.1-1) is depicted in Fig.1-2. The back-side structure consists of a few microns of highly p-doped concentration. This unstructured layer serves as a thin radiation entrance window. It is covered with a very thin homogenous aluminum layer that offers a mask against the light and hardens the X-ray beam. The very thin P^+ surface layer (0.5 μm) is employed as a rectifying contact once the external bias voltage is applied.

The detector substrate has a thickness of 450 μm composed of homogenous and weakly doped n-type silicon (N_{D-}) with an epitaxial growth (N_{D+}) of maximum 10 µm along the charge transfer direction. The bulk substrate is fully depleted thus offers a medium for the photon interaction. The epitaxial layer implant serves to localize the potential well for storing the electron signals underneath the shift registers.

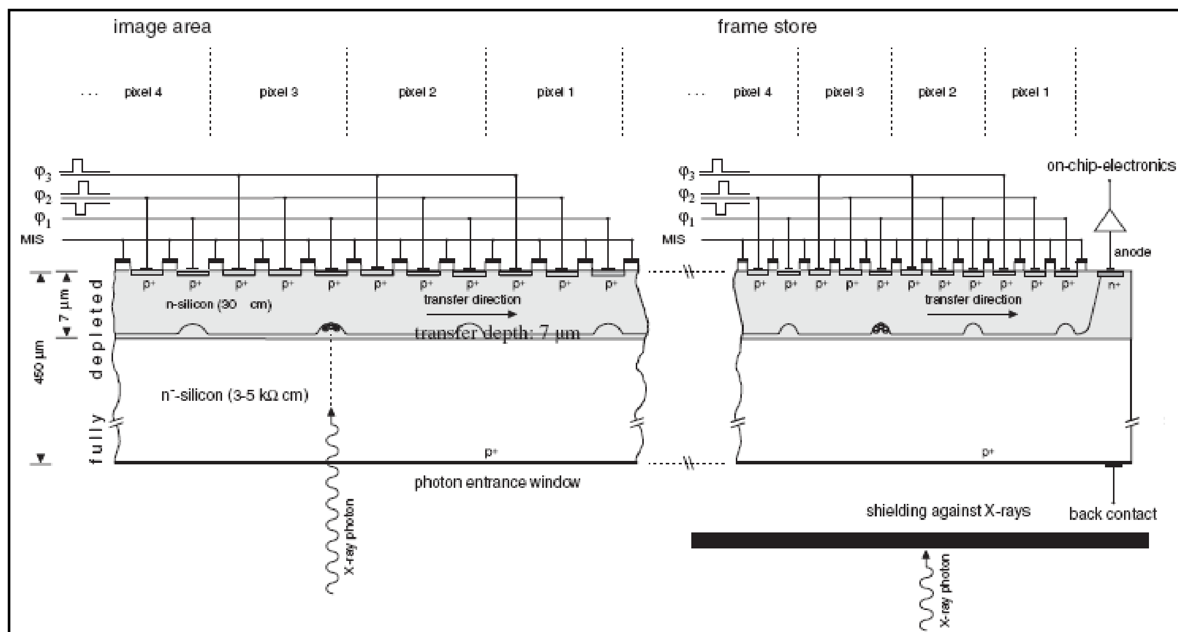

Fig.1-2: Cross section through the detector volume along one transfer channel.

A.4- Single Register Storage

The full depletion in the pnCCD is accomplished by the application of reverse biased voltages as a high voltage applied to the large rectifying P^{+} backside contact and less negative voltage for the register contacts both relative to the anode positive voltage. Therefore, if the incoming photon creates a cloud of electron-hole pairs in the detector, the electrons will be instantaneously subjected to the electric field force driving them from the place of interaction to the register side where they will be stored in the potential well. Meanwhile the holes will move to the opposite direction toward the back side.

The pnCCD is a three phase pixelated detector. Therefore three transfer registers consequently are required to define one pixel and to form the potential well. The fact that the applied voltages are controlled by external means makes it possible to form the potential well underneath single or double registers. For single register (Fig. 1-3, left), if -17V of $\mathrm{V+}$ refers to the voltage that will localize the potential well with respect to -21V for the barrier voltages $(\mathrm{V-})$. The center of the potential well is positioned under the middle register of $\mathrm{V+}$ voltage. Since the pixel size is $75\mu m$ the lateral width of the potential well equals $25\mu m$ while its depth stays maximum within $10\mu m$. Switching the three register voltages in a certain periodic pattern, the signal charge can be transported from the original pixel to the readout n^{+} anode.

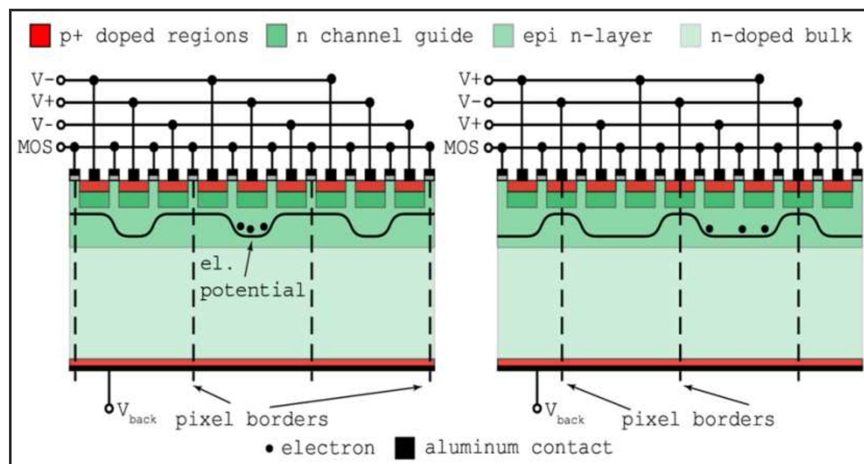

Fig.1-3: Schematic cross section through the fully depleted pnCCD along one transfer channel.

If double registers storage is required (Fig. 1-3(right)), then the application of $\mathrm{V+}$ upon two registers would accomplish this of which the center of the potential well is located under the MOS-gate between

the two registers. The voltage that is applied to the aluminum contacts of the MOS-gates is 0V. According to the applied register voltages, the detector is operated with a single register storage mode.

Table1-2: The pnCCD physical parameters.

Operating mode	Frame store
Pixel Size	75 µm × 75 µm image area 75 µm × 51 µm frame-store area
No. of Pixels/area	256 × 256
No. of Channels	512 (256 on each readout side)
Sensitive Area	19.2 mm × 19.2 mm image area 19.2 mm × 13.1mm Frame store area
Sensitive thickness	450 µm
Frame Rate	126 Hz

A.5 Frame-Store Scheme of the pnCCD Array

The geometrical 2D design of the pnCCD array discussed above is practically divided into two sectors via shielding half of the detector array against the incoming x-rays as shown in figure 1-4. The physical size of the pnCCD is presented in table 1-2. The part of the array that is sensitive to the X-ray photons is called *image area*. This area accumulates the generated electrons during the exposure time. The shielded area against the x-rays is called the *frame-store* which locates a preserved area for the charge packets shifted from the image area waiting for the readout stage. A copper plate is used to protect the frame-store area from the incoming X-ray photons (Fig. 1-4: C). Within 154 µs, the transfer process from the image area to the frame-store area is accomplished. Thereby each row from the image area is transferred to the corresponding row in the frame-store area. The frame data that are preserved in the stored area are henceforth serially read out row by row within 7.35 ms readout time. Once completing the transportation from the image to the frame-store area, the image area is biased again for the integration phase for new signals. Therefore the minimum programmable exposure time that can be defined equals the readout time.

B. The Readout Process and the associated electronics

In order to measure the charge amount contained in the potential well, it has to be converted to voltage. Four phases can be identified. The charge packet has to be transferred to the readout anode at the end of each channel.

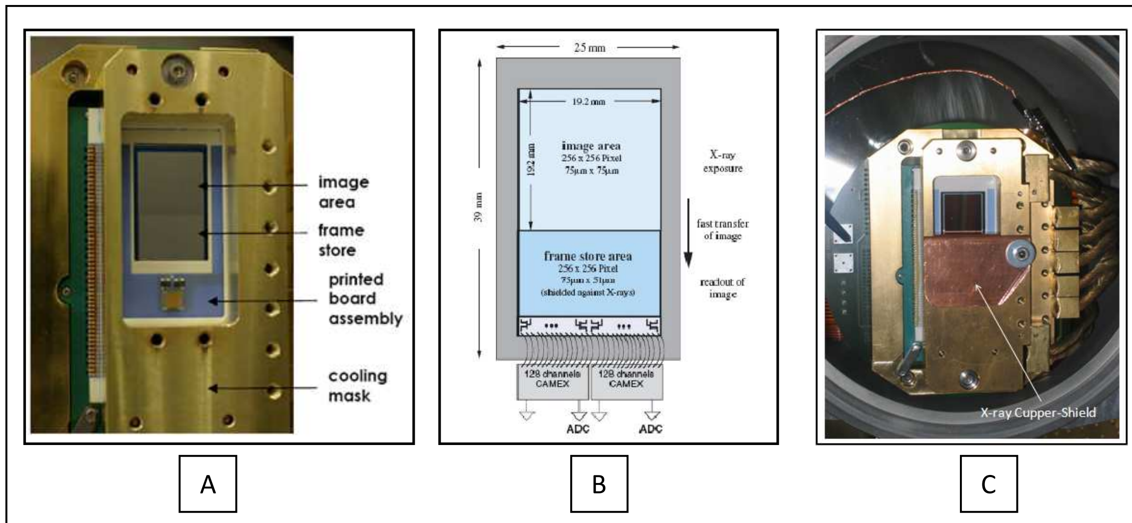

Fig.1-4: Image (A) shows the pnCCD chip as mounted on the inner board with the cooling mask placed on the top of the ceramic board. Image (B) is a drawing of the pixel array sections. Image(C) depicted the structures as mounted inside the vacuum chamber and the cupper plate for shielding the buffer area from the incoming X-ray.

The anode is connected to a JFET for on-chip signal amplification. Further signal processing is performed with two CAMEX chips (**C**MOS **A**mplifier and **M**ultipl**EX**er) which are implanted on a ceramic substrate and bonded to the front-end JFETs. Each CAMEX has 128 channels which are terminated with two multiplexers. The processed signals are driven to the 16-bit ADC cards and converted into corresponding digital values. The readout procedure is therefore parallel in processing the signals from different channels.

The pnCCD controller consists of a DC power supply modules providing 32 voltages for the whole system, a sequencer unit and two ADC cards. The controller is arranged in a crate and connected to the master PC (Data acquisition PC) via a bi-directional optical cable for transferring the data. The internal bus system is the widely used compact-PCI (cPCI) bus.

The external power supply units are utilized to power up the detector and the allied electronics in a controlled order. The modules are connected with the master PC via an Ethernet cable. A software package is written to facilitate the operation. It includes an assigned voltage values that feed the detector and its electronics gradually.

The *sequencer* module is a pattern generator which creates all necessary digital timing signals to synchronize the operation of the system components including the detector, the CAMEX chip and the ADC. All the generated signals are differential for noise immunity reasons. The clocking operation

applied upon the detector follows a time sequences which are written in a script. The command is sent from the master PC to the "sequencer" to acquire the input timings script. The sequencer is connected to the detector and the synchronization follows the defined timing periods. The sequencer has time resolution of 10 ns compromising 64 LVDS output line [ref.7].

The pnCCD and the CAMEX chips are mounted on a printed circuit board inside the vacuum chamber. A *ceramic substrate*, the *pulse drivers*, and the *RC Filter* are the elements of the "inner" board. The chamber is evacuated down to $10^{-6}\, mbar$ and the inner temperature is stabilized at $-\,80\, °C$. The cooling mask is attached to the detector as shown in Fig. 1-4. The inner board is connected to another board located outside the chamber. The "outer" board hosts the digital and analog signal drivers and all the cable connectors.

B.1- Three Phase Charge Transfer Mechanism

The three dimensional structure of the pixel is rather straight forward. The pixel is extended in depth and providing the electron potential minimum in the z-axis. The channel stops provide a physical gap between the channels that prevents any lateral diffusion along the line direction (x-axis). The barrier register voltages make the separation between the pixels available in the charge transfer direction (y-axis).

Once the electron charges are collected inside the potential well, the transfer mechanism into the readout anode at the end of the transfer channel can be processed and handled entirely inside the epitaxial layer. Subsequent transfers of the charge packets from one register to the following ones will couple them as a consequence of the applied storage voltage and barrier voltages of the three registers in each pixel.

The clocking mechanism of the charge transfer is shown in Fig.1-5. The storage register ϕ_2 is set to a voltage of -17V whilst the barrier registers are held at -21V. The readout anode has a 0V. After a certain time period, the following register ϕ_3 increases to -17V. Therefore, two registers at this instance are depleted under the same voltage and the electrons will move under this concentration gradient due to the self-induced field being negatively charged particles. Proceeding by reducing the potential ϕ_2 to -21V, the charge transfer will result in a fringing-field created by the register potential difference, affecting the electrons again and will drive them to be stored under the next register completely. In this respect, the fringing-field is strong and much more efficient in speeding up the electron transit compared with the self-induced field. This sequence may be repeated to move the charge packet through the device to the readout node.

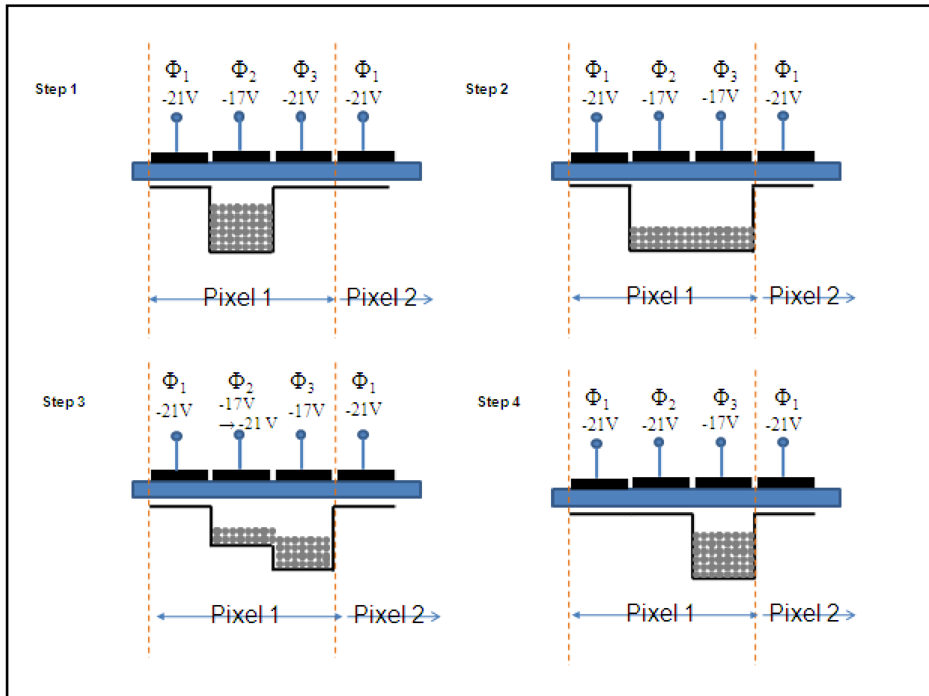

Fig.1-5: The charge transfer process from one pixel to the next delineated with the dash lines

B.2- The Front- End Electronics

In order to drive a high impedance load from the small-capacitance anode toward the CAMEX, a front-end electronics is integrated on the detector and connected with n^+anode via an aluminum layer. Figure 1-6-A depicts the elements of the on-chip electronics which consists of the readout anode (C_d) and the CAMEX (A). In this configuration, the first FET (FF) is a low noise n-channel JFET that is operated as a source follower. The gate of the first FET is connected to the anode. The source-drain current is fixed by the current generator ($F2 - R_s$) which is located on the CAMEX chip . Therefore, the voltage amplitude of the source is approximately the same as the gate input voltage and has the same phase. For amplification factor less than 1 for the source follower, the output voltage will hence drop and vary with the input amount of charge from the anode. Therefore, FF matches the high input impedance of the readout anode to the lower one in the CAMEX chip. The second n-channel JFET is the Reset FET (RF), whose source is connected to the anode, drains the signal charge on the anode after the readout is completed. Figure 1-6-B shows the design of the JFETs. They have n^+ implant for the circularly-shaped drain, p^+ for the ring- shaped gate and n^+ for the ring-shaped source. Further details for the noise sources and calculations are described in [ref.5].

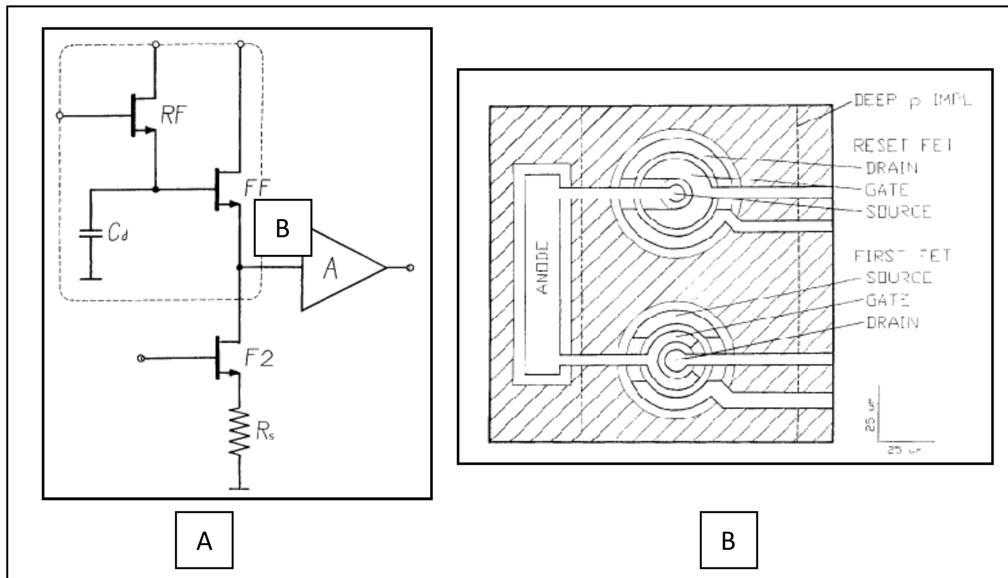

Fig.1-6: Front-end electronics

B.3- The CAMEX Chip

The source follower stage is thereafter connected to the off-board CAMEX chip. The CAMEX is designed for reading-out 128 channels of the detector in parallel. Two CAMEX chips are thus implemented for the pnCCD in use. The chip carries out further signal processing as shown in Fig.1-7. The mechanism starts with the amplification of the signal by the JFET amplifier followed by filtering out the high frequency noise in the low pass filter. Signal filtering is performed by the eight-fold correlated double sampling (CDS).In this stage, the average of 8 consecutive samples is taken to measure the baseline, then 8 samples are taken after the CCD shift to measure the average of baseline plus signal. The difference between the sampling blocks is the CCD charge signal. Having 8-fold CDS performs digital low pass averaging filter and enhances the signal to noise ratio. This stage is programmable and can be used to speed up the readout by reducing the number of sampling folds up to tolerant noise level. The sampled signals are stored in the sample and hold stage and then multiplexed using tow output nodes toward the ADC [ref.6 & 7].

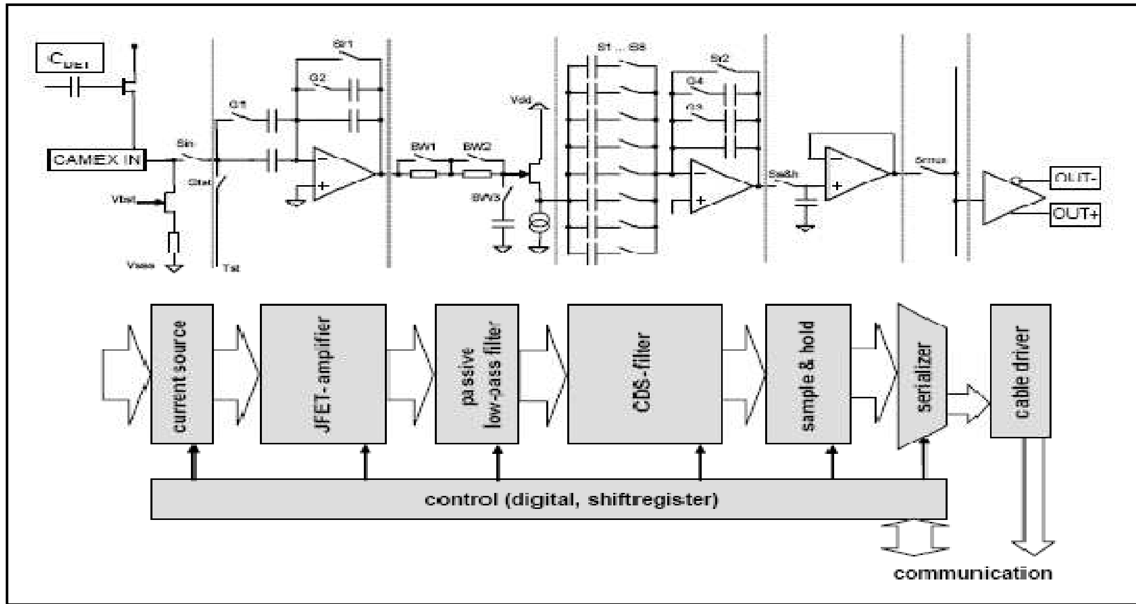

Fig.1-7: The CAMEX chip

C. Related Semiconductor Physics Relations

The voltages applied upon the detector's backside and register side are shown in table1-3. They fulfill the condition of complete depletion for the PN junctions and the charge transfer toward the readout anode.

The pnCCD wafer has PNP structure with two PN junctions. The $P^{+}n^{-}$ is the first PN junction between the rectifying back contact and the bulk. The $P^{+}n^{+}$ is the second one between the registers contact and the thin epitaxial layer. No junction exists between the $n^{-}n^{+}$ since both of them are n-type semiconductor materials. The external voltages are applied upon the pnCCD such that the chip is reversed biased. This is achieved by the application of a high negative voltage V_B on the backside and a low negative voltage on the registers with respect to the positive anode voltage. Reference to the values in table 1-3, full depletion of the detector is achieved and the potential minimum is confined within the epitaxial layer. The electric potential therefore has maximum value at the rectifying back contact and decreases steadily to a minimum value at the epitaxial layer. The front side is depleted as well and the depletion region extends from the registers toward the $n^{-}n^{+}$ interface having the potential minimum. The following discussion and figures related to references [8,9,10].

Table1-3: Applied voltages on the front-side and back-side of the

Name	Applied upon	Value (volt)
Depletion voltage (V_B)	P^+ rectifying back contact	-230
Register High voltage (ϕ_{high})	P^+ storage registers	-17
Register Low Voltage (ϕ_{low})	P^+ Barrier registers	-21
Anode Voltage(V_{Anode})	n^+ readout anode	0
MOS Voltage	MOS gate	0

C.1 The Reverse Bias PN Junction and the Depletion Voltage

The PN junction is created at the boundary between the N-type and the P-type silicon when they are implanted on each other, Fig. 1-8-(1). In the N-region, the electros are the majority carriers while in the P-region the electrons are the minority carrier.

The free electrons in the N-region move randomly in all directions at room temperature. By forming the PN junction, a momentary diffusion current arises due to the difference in the concentrations of the electrons on both sides of the junction. Therefore, the free electrons near the junction in the N-region begin to diffuse across the junction into the P-region and recombine with the holes there. Holes behave the same and they diffuse to the N-region. Due to the loss of the electrons in the N region, a positive layer is created. Similarly, negative layer is built in the P-side due to the loss of the holes. A built-in potential builds up which acts as a barrier against the electron movements due to the built-in field force. This makes the net current zero and the situation can be considered as the diffusion current is balanced by the drift current which is generated from the potential difference. The space-charge region around the metallurgical junction where the built-in potential exists is called the depletion region, Fig. 1-8(2).

The width of the depletion region when the PN junction is in equilibrium condition can be estimated using the Fermi level diagram Fig 1-8(3). The built-in potential (V_B) can be obtained according to the position of Fermi level. Fermi level must be the same in the PN region such that the probability of finding an electron at energy (E) must be the same throughout otherwise the electrons would flow to those regions of higher probability but of the same energy. According to the Fermi-Dirac distribution function, the probability of 50% is determined by $-E_F$. It is known that E_F is shifted towards the conduction band of energy E_c in the N-type semiconductor, and towards the valance band E_v in the P-type.

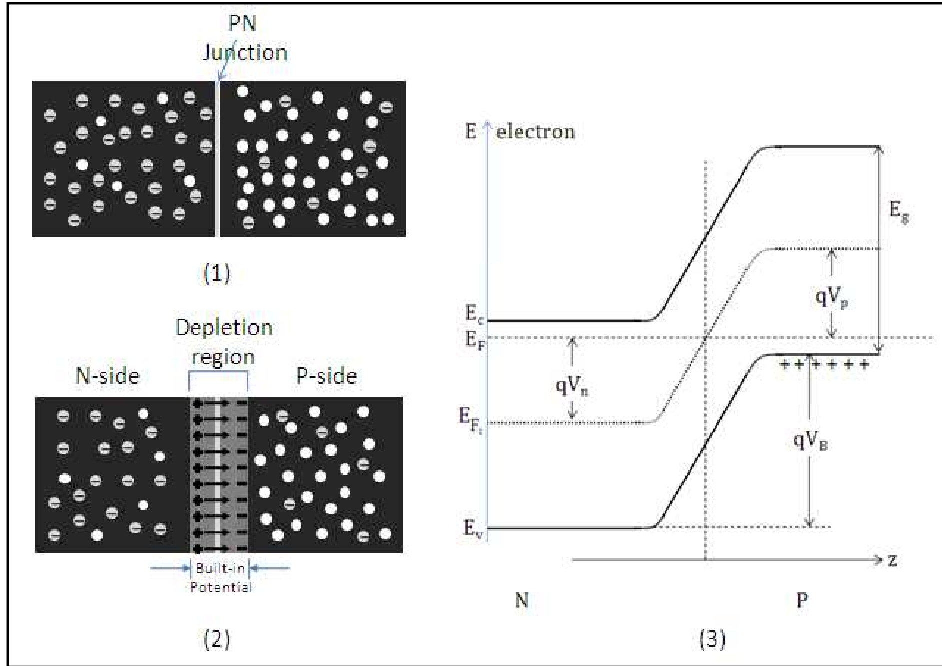

Fig.1-8: Drawing shows the formation of the depletion region once the P-type and N-type semiconductor materials are attached (1 & 2), and (3) is the Fermi level diagram.

Therefore for constant E_F, the conduction and the valance bands have to bend in the vicinity of the junction as shown in the figure 1-8(3). The energy level E_{F_i} is the position of E_F in an intrinsic semiconductor (approximately in the middle of the gap), qV_n and qV_p are the energy shifts of E_F on the two sides of the junction with respect to E_{F_i}.

The built-in potential which is the potential difference formed according to the band bending in equilibrium is given by: $V_B = V_n - V_p$

At a given temperature (T) with the doping concentration N_A in the P-region and N_D in the N-region, the barrier potential can be given by

$$V_B = \frac{KT}{Q_e} \ln \left[\frac{N_A N_D}{n_i^2}\right] \tag{1-1}$$

where K is Boltzmann constant, n_i is the intrinsic carrier density.

The depletion depth in the N-type region (d_n) and in the P-type region (d_p) can be estimated by solving Poisson's equation. The solution as follows:

$$d_n = \sqrt{\frac{2\varepsilon_r \varepsilon_o N_A}{Q_e N_D (N_A + N_D)} V_B} \tag{1-2}$$

$$d_p = \sqrt{\frac{2\varepsilon_r \varepsilon_o N_D}{Q_e N_A (N_A+N_D)} V_B} \quad (1\text{-}3)$$

where ε_r is the relative permittivity for silicon ($\varepsilon_r = 11.68$) and ε_o is the vacuum permittivity ($8.8541 * 10^{-12} F/m$) .The total depletion length is the sum of d_n and d_p.

If an external potential difference V_A is connected such that the positive side is attached to the n-region and the negative side is attached to the p-region, a reverse- biased PN junction is obtained. In this case, the positive side of the voltage source attracts the free electrons, which are the majority carriers in the *n* region, away from the *pn*-junction. As the electrons flow toward the positive side of the voltage source, additional positive ions are created. In the *p*-region, electrons from the negative side of the voltage source enter as valence electrons and move from hole to hole toward the depletion region where they create additional negative ions. This results in a widening of the depletion region and a depletion of majority carriers. Since d_n and d_p are proportional to $\sqrt{V_B}$, the application of reverse bias causes separation of the Fermi levels on the two junction sides to increase the bending of the energy bands, which now appear as shown in Figure 1-9. The width of the depletion region and the maximum field at the junction grow with reverse bias ($\sqrt{V_A + V_B}$). As more of the *n* and *p* regions become depleted of majority carriers, the electric field between the positive and negative ions increases in strength until the potential across the depletion region equals the bias voltage, V_A.

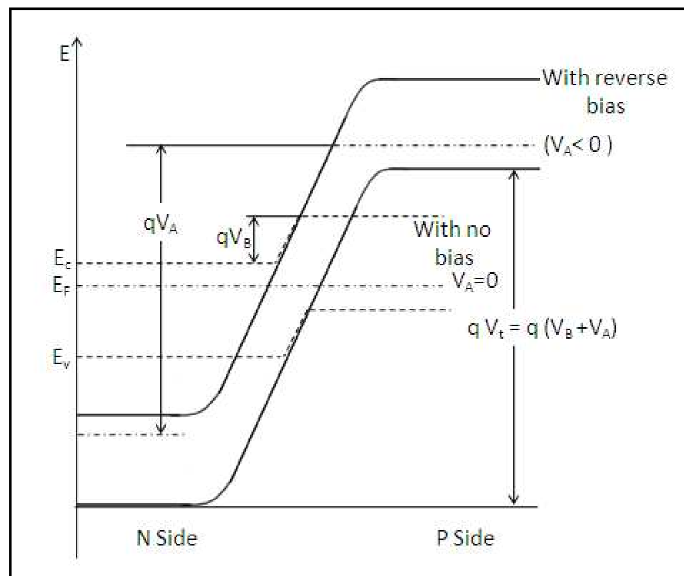

Fig.1-9: The PN junction under the reverse-bias voltage

The depletion voltage which is required to extend the depletion region over the whole weakly doped n^{-}substrate thickness (w_n) for the case of $N_A \gg N_D$ can be then calculated as follows:

$$V_{depletion} = -\frac{Q_e N_D}{2\varepsilon_r \varepsilon_o} w_n^2 \quad (1\text{-}4)$$

The maximum electric field occurs at the junction is given by

$$E_{max}\left[\frac{V}{cm}\right] = \sqrt{\frac{2Q_e}{\varepsilon_r \varepsilon_o}\frac{N_A N_D}{N_A + N_D} V_A} \quad (1\text{-}5)$$

In the pnCCD, the doping concentration values for the backside contact and the substrate contacts are given in table 1-1. If the tabulated values are substituted in formula (1-1) above, the estimation for the built-in voltage and the depletion voltage can be obtained. The built-in potential when no external voltage is applied is:

$$V_B = \frac{1.38*10^{-23}\frac{m^2.kg}{s^2.K} * 300K}{1.6*10^{-19}C} \ln\frac{10^{18}*6*10^{11}}{(1.45*10^{10})^2} = -0.56V$$

The depletion in the P region (d_p) is $2.1 * 10^{-5}\mu m$ and in the n region (d_n) is $35\ \mu m$. The applied potential that is needed to make the full depletion along the weakly doped silicon bulk is (Eq. 1-4):

$$V_{depletion} = \frac{-1.6*10^{-19}C*6*10^{11}cm^{-3}}{2*11.6*8.85*10^{-14}F/cm}(0.045cm)^2 = -95\ V$$

This voltage is supplied to the backside contact since the anode voltage (V_{Anode}) is kept 0 V. Since the silicon bulk is fully depleted by this voltage, further increasing of the applied voltage on the backside ($V_B = -230\ V$) will make the electric field more uniform in the silicon bulk. This voltage will shorten the drift time of the generated electron cloud to reach the potential minimum.

The maximum electric field for the applied backside voltage (V_B) of -230 V is

$$E_{max} = \sqrt{\frac{2 * 1.6 * 10^{-19}C * 6 * 10^{11}cm^{-3}}{11.6 * 8.85 * 10^{-14}F/cm} * 230V} = 6559\ V/cm$$

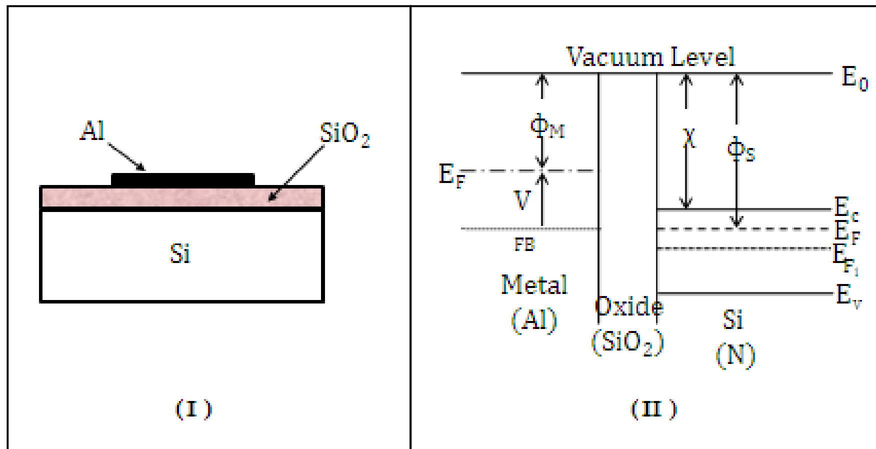

Fig.1-10: MOS capacitor cross section (I) and the corresponding Fermi level diagram (II)

C.2- The Metal-Oxide Semiconductor Capacitor

The metal-oxide semiconductor capacitor (MOS) capacitor involved in the structure of the depleted front side of the detector provides practically the physical separation between the shallow depleted P^{+} registers. The applied voltage on the registers besides the presence of the positive and negative space charges of the silicon implants provides electric potential barriers. The following description shows how the voltage which supplies the MOS capacitor is optimized to enhance the separation and reduces attracting the signal electrons.

The MOS capacitor has Al metal plate on the upper side and the homogenously doped N-type silicon on opposite side with oxide insulator in between (SiO_2), Fig.1-10(I). Energy bands for the elements in the MOS capacitor with respect to the vacuum level are shown in figure 1-10(II) when separated from the capacitor. The vacuum level is the same for the elements in the MOS structure and refers to the work function E_0 which is needed for an electron to leave its surface.

The energy level diagram may be used to describe the situation when the capacitor is built up. Since the oxide insulates the metal from the silicon, the charge carriers will have little chance to cross from the silicon to the metal and thermal equilibrium condition can be applied separately on each element. Under this condition, potential difference will appear because of the difference in work functions between the aluminum and the silicon when the Fermi levels align themselves in the capacitor's elements. The silicon being the higher work function becomes negative with respect to the metal. Part of the potential drop takes place in the oxide by causing the conduction band and valance bands to bend.

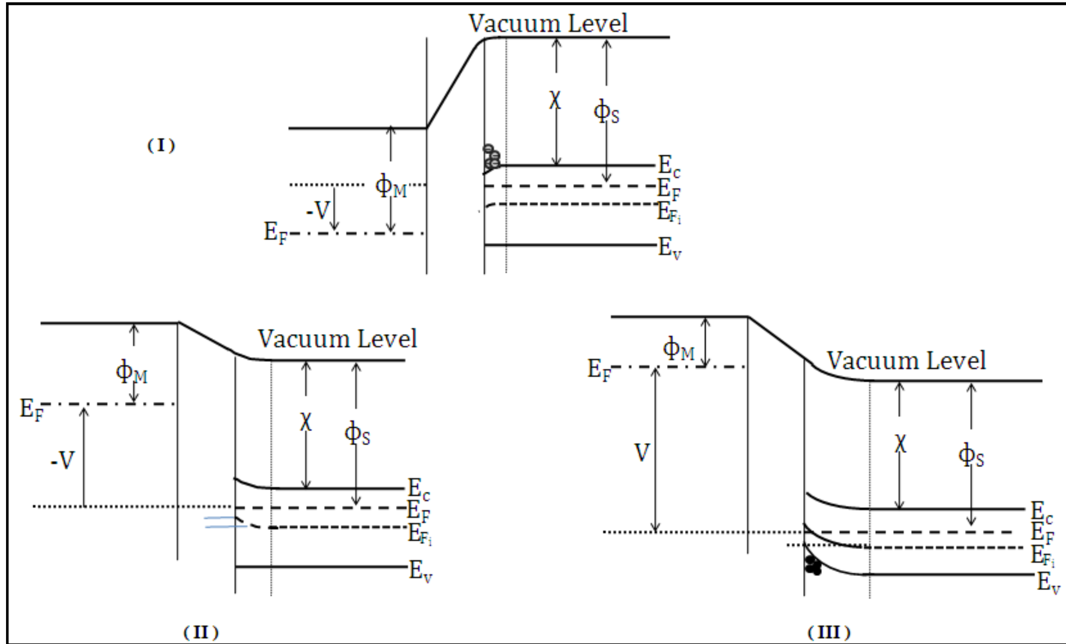

Fig.1-11: Energy diagram in of the N-type MOS capacitor: (I) Accumulation ;(II) surface depletion ; (II) Inversion.)

The other part of the voltage drop causes the bands in silicon to bend such that the Fermi level gets closer to the conduction band, Fig 1-11(I). This leads to an accumulation of the electron charges at the silicon-oxide interface.

To compensate for the voltage drop such that the bands return flat, the so called **flat-band voltage** (V_{FB}) has to be applied across the capacitor

$$V_{FB} = \frac{\phi_M - \phi_S}{Q}$$

where ϕ_M and ϕ_S are the respective metal and Si work functions in eV. The value of V_{FB} for Al-gate on n-doped silicon is - 0.3V and -0.5V for heavily ($10^{15} cm^{-3}$) and weakly ($10^{12} cm^{-3}$) doping density respectively. This voltage will cause the electric field across the oxide to be zero which in turn makes the interfaces free of any residual charge.

At the silicon-oxide surface, **accumulation**, **depletion**, and **inversion** are the forms of charge status at the interface under the application of applied voltage (V_{App}). If the silicon is grounded and the voltage is applied to the Al gate, the **flat-band voltage** and the **threshold voltage** (V_T) can make the distinction for the charge status at the interface. Figure 1-12 shows the details.

Surface accumulation occurs when $\mathbf{V_{App}} > \mathbf{V_{FB}}$ with the result that the applied positive voltage makes the potential at the semiconductor–oxide interface more positive. This will increase the negativity of the silicon due to the induced negative charges in the silicon. As a consequence, the energy bands will bend even more and the Fermi level gets closer to the conduction band edge so the electrons will be shifted to the interface and accumulates in the vicinity Fig. 1-11(I). Due to the exponential dependence of the electron concentration on the potential, the region of increased electron concentration is so thin that can be approximated to be a surface-charge density (Q_{acc}) at the interface as follows:

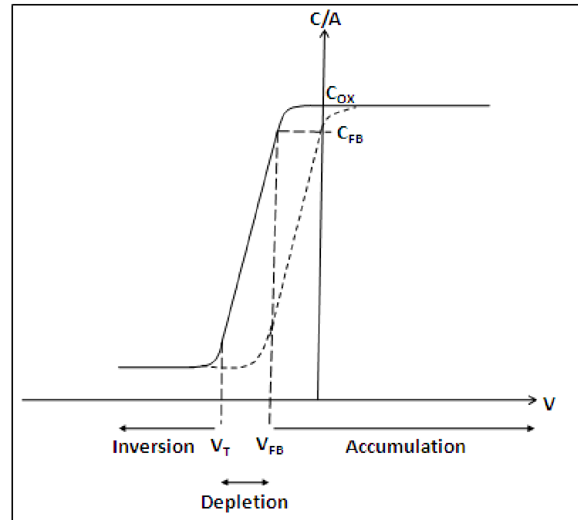

Fig.1-12: The capacitance versus applied voltage for high frequency capacitance. Solid-line is the real capacitor and dashed-line for ideal capacitor.

$$Q_{acc} = -\varepsilon_{ox}\varepsilon_0 \frac{V_{App}-V_{FB}}{d_{ox}} = -C_{ox}(V_{App} - V_{FB})$$

where C_{ox} is the oxide capacitor per unit area and ε_{ox} is the relative permittivity of the oxide and it is 3.9 .

Depletion can be reached via decreasing the applied voltage such that $\mathbf{V_T} < \mathbf{V_{App}} < \mathbf{V_{FB}}$. In this case the bands will bend upwards and the electron concentration at the surface will decrease, Fig. 1-11(II). The electrons being pushed away from the interface leave the surface free of electrons and hence fixed positive donor impurity space charge remains (depletion layer). The space charge in the depletion layer (Z_{dep}) would have a capacitance per area for a given V_{App} as:

$$C_D = \frac{\varepsilon_r \varepsilon_0}{Z_{dep}}$$

where ε_r is the relative permittivity of the silicon (11.68). On the other side, the oxide capacitor is due to the aggregation of the induced negative charges at the Al–oxide interface.

The MOS capacitor (C_{MOS}) is given by the oxide capacitor (C_{ox}) and the depleted silicon capacitor (C_{dep}) as follows:

$$C_{MOS} = \frac{C_{ox} * C_{dep}}{C_{ox} + C_{dep}}$$

An **inversion** of the semiconductor type, Fig. 1-11(III), is reached through decreasing the applied voltage below the threshold voltage ($\mathbf{V_{App}} < \mathbf{V_T}$). The intrinsic level at the interface will reach – and eventually cross – the Fermi level. Then we shall have a majority of holes at the interface.

At the onset of the inversion, the positive semiconductor charge density Q_B is determined by the maximum thickness of the depletion layer d_{dep} when the voltage across it (the band bending) is

$$V_B = \left|\frac{2\phi_F}{q}\right|$$

Where $\phi_F = E_{F_i} - E_F$ is in electron volts. By using the equation (4) , the total charge density is

$$Q_B[C/cm^2] = qN_D d_{dep} = \sqrt{2q\varepsilon_r\varepsilon_0 N_D V_B}$$

The threshold voltage for inversion is the sum of V_{FB}, the voltage drop V_B across the silicon depletion region and the voltage drop across the oxide necessary to support the depletion charge $-Q_B$ ($Q_e \approx 0$ at the threshold):

$$V_T = V_{FB} - \frac{Q_{ox}}{C_{ox}} + \frac{2\phi_F}{q} - \frac{Q_B}{C_{ox}}$$

For example, the MOS capacitor made of <111> N-type semiconductor, doped with $N_D = 10^{12} cm^{-3}$, with Al metal on oxide insulator 0.4 μm thick, will have threshold voltage calculated as follows:

$$C_{ox} = \frac{\varepsilon_{ox}\varepsilon_0}{d_{ox}} = \frac{3.9 * 8.854 * 10^{-14} F/cm}{0.4 * 10^{-4} cm} = 8.63 * 10^{-9} F.cm^{-2}$$

$$V_{FB} = -0.5\ V$$

$$Q_{ox} = +2.0 * 10^{11} q.C.cm^{-2}$$

$$\phi_F = E_{F_i} - E_F = KT \ln\frac{N_D}{n_i} = 1.38 * 10^{-23} * 300 * \ln\frac{10^{12}}{10^{10}} = 0.19\ eV$$

$$\frac{2\phi_F}{q} = -0.24\ V$$

$$Q_B = 2.83 * 10^{-10} C.cm^{-2}$$

$$V_T \approx -0.3 - 3.7 - 0.24 - 0.033 \approx -4.27\ V$$

D. The Potential Profile in the Silicon Substrate

The interface between the epitaxial layer and the bulk of the detector will fix the electron potential minimum within this layer underneath the registers. Electron-hole pairs generated in the depleted bulk experience the electric field that generates a force which pushes the electrons into the potential minimum and the holes to the backside of the detector.

An approximated one-dimensional solution of the potential profile in the silicon bulk as well as in the epitaxial layer can be obtained by solving Poisson's equation by considering the boundary conditions of the device and the fact that the full depletion occurs in the weakly and uniformly doped silicon bulk [ref. 4].The electric potential solution ignores n^+ contacts and the built-in potential as well. Figure 1-12 shows schematic drawing of the N-type silicon: (1) the epitaxial region and (2) the detector bulk. The origin of the z-axis, the depth, is taken at the front side.

Poisson's equation in the regions is:

$$\frac{\partial^2 \varphi_1}{\partial z^2} = -\frac{e.N_{D1}}{\varepsilon_o \varepsilon_r} \quad ; \quad 0 \leq z \leq z_{epi} \qquad (1\text{-}6)$$

$$\frac{\partial^2 \varphi_2}{\partial z^2} = -\frac{e.N_{D2}}{\varepsilon_o \varepsilon_r} \quad ; \quad z_{epi} \leq z \leq z_B \qquad (1\text{-}7)$$

where ($e.N_{D1}$) and ($e.N_{D2}$) is the space charge density in region (1) and (2) respectively.The doping concentrations N_{D1} and N_{D2} have the values as depicted in the figure. ε_o is the permittivity of the vacuum and ε_r is the relative permittivity of the silicon. z_{epi} is the thickness of the epitaxial layer and z_B is the thickness of the device. The solution of the electric potentials φ_1 within the epitaxial region and φ_2 for the rest of the device as a function of z position is given by:

$$\varphi_1(z) = -\frac{e.N_{D1}}{\varepsilon_o \varepsilon_r} * z^2 + \left[\frac{V_B - V_F}{z_B} + \frac{e.N_{D2}}{\varepsilon_o \varepsilon_r}.z_B - \left(\frac{e.N_{D2}}{\varepsilon_o \varepsilon_r} - \frac{e.N_{D1}}{\varepsilon_o \varepsilon_r}\right)\left(z_{epi} - \frac{z_{epi}^2}{2z_B}\right)\right] z + V_F \qquad (1\text{-}8)$$

$$\varphi_2(z) = -\frac{e.N_{D2}}{\varepsilon_o \varepsilon_r} * z^2 + \left[\frac{V_B - V_F}{z_B} + \frac{e.N_{D2}}{\varepsilon_o \varepsilon_r}.z_B - \left(\frac{e.N_{D2}}{\varepsilon_o \varepsilon_r} - \frac{e.N_{D1}}{\varepsilon_o \varepsilon_r}\right)\left(\frac{z_{Epi}^2}{2z_B}\right)\right] z$$

$$-\left(\frac{e.N_{D2}}{2\varepsilon_o \varepsilon_r} - \frac{e.N_{D1}}{2\varepsilon_o \varepsilon_r}\right) * z_{Epi}^2 + V_F \qquad (1\text{-}9)$$

The boundary conditions involved in the solution are:

- The electric field at the interface: $\frac{\partial \varphi_1(z=z_{epi})}{\partial z} = \frac{\partial \varphi_2(z=z_{epi})}{\partial z}$

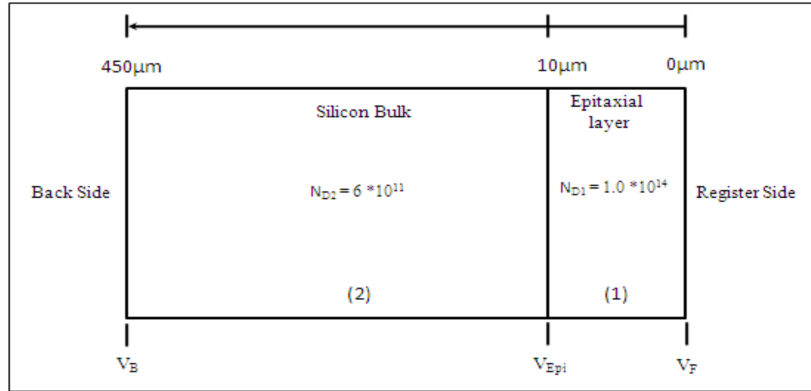

Fig.1-12: *Sketch for the interface between the bulk and the epitaxial layer*

- The applied back voltage (V_B) and the front voltage (V_F): $\varphi_1(z = 0) = V_F$; $\varphi_2(z = z_B) = V_B$
- The position of the electron potential minimum: $\varphi_1(z = z_{epi}) = \varphi_2(z = z_{epi})$

The potential profile has thus a parabolic term superimposed with the linear term. The plot of the potential profile is shown in Fig. 1-13 according to Eq.(8) and Eq.(9). Two profiles are illustrated considering different applied voltages at the back side (-230 V and -130 V) for the same voltage value (-17 V) applied on the storage resister.

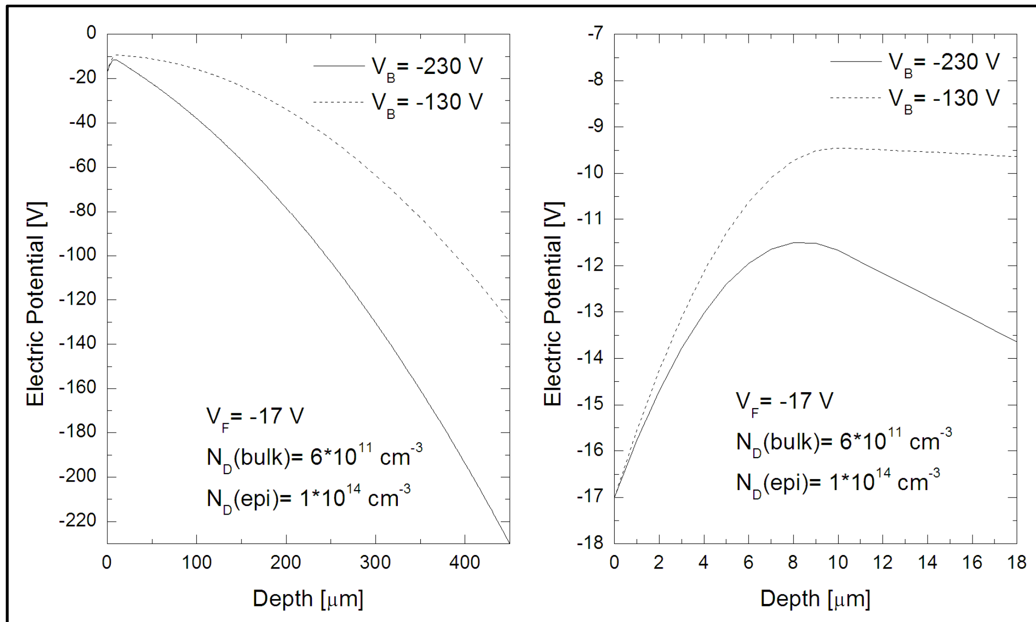

Fig.1-13: Output plots for the potential profiles in the pnCCD using two different back side voltages (V_B) for the same register's voltage (V_F). Left: along the 450 μm device thickness; Right: up to 18 μm. The plot in the right hand side shows that the potential minimum for the applied V_B has depth less than 10 μm which is confined within the size of the epitaxial layer.

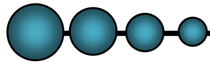

2. Characterization and Operational Parameters of the pnCCD

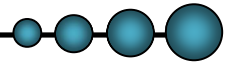

The anticipated performance of the pnCCD detector and its image formation are influenced by many factors. This incorporates the fabrication limitations in the detector and the quality and the quantity of the radiation source exposing the detector. This chapter introduces the parameters that may influence the experimental results in order to be taken into consideration in the preparation of the experiment. It serves as well for guiding in the data evaluation and the final conclusions.

A. Attenuation of Photon Beam in Silicon

The pnCCD is fully depleted silicon detector and has wafer thickness of 450 μm. Beside the type of the detector material and the detector thickness, the probability of the photons to undergo an interaction depends on the X-ray energy.

The interaction of a collimated and monochromatic X-ray beam of intensity (I_0) striking the detector perpendicular to the backside surface follows the exponential behavior of which the incoming intensity will be reduced by a fraction of:

$$P(x) = e^{-\mu(E)\rho Z} \tag{2-1}$$

where $\mu(E)$ is the mass attenuation coefficient of silicon for the incident photon energy E , ρ is the silicon density and Z is the depth in the detector bulk where the photon is converted.

Figure 2-1 is a plot of the mass attenuation coefficient for silicon versus the X-ray photon energy [ref. 11]. The plot shows that:

I. the photoelectric effect is dominating the interaction process in silicon up to 55 keV.
II. the mass attenuation coefficient of the photoelectric absorption is decreasing rapidly with increasing the photon energy. The abrupt increase in the plot of the photoelectric effect is due to the K absorption edge in silicon at 1.84 keV.

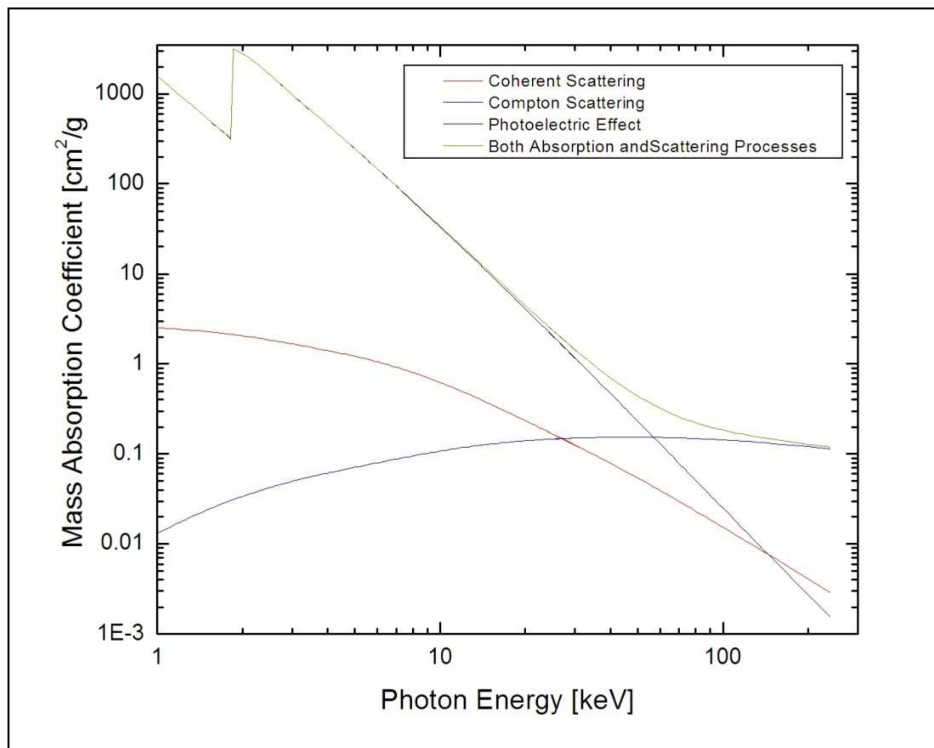

Fig.2-1: Plots of the mass attenuation coefficient in silicon versus the x-ray photon energy for the absorption and scattering processes.

B. The Position Resolution and Charge Sharing

The pnCCD is position sensitive detector since the interaction position of the X-ray photons can be addressed up to a certain resolution. The position resolution of the detector depends primarily on the pixel geometry. Each pixel in the pnCCD is composed of three registers and it has square shape of 75 µm*75 µm. Since the middle register is the storage one and the other two registers are barrier registers, the response function is essentially box-like. Therefore, the position resolution is equal to the register's pitch.

Charge sharing is determined by the amount of charges split between numbers of pixels. Beside the pixel geometry, the charge sharing is influenced by:

a) the size of the charge cloud which depends on the depth in the detector volume where the photon is converted.
b) the position of the charge cloud relative to the pixel boarders.

The primary charge cloud, represented by the number of electrons which are generated from the interaction of photon with the silicon atom, is pushed from the interaction position toward the front side via the driving force of the electric field. During the drift and due to the influence of the diffusion and mutual electrostatic repulsion, the charge cloud expands as the square root of drift time in the diffusion case and cubic root of drift time in the case of repulsion [discussed in chapter 3-D]. Since the two processes are coupled and occur simultaneously, their influences determine the size of the electron cloud at the time it reaches the potential minimum.

The pixel size influences the charge sharing of which the probability of the sharing increases with the smaller pixel size. For single photon detection (moderate photon flux), the charge sharing patterns can be analyzed using a signal threshold. A pattern of single-hit event means that the amount of signal charge collected in one pixel is higher than the signal threshold in its neighboring pixels. A double-hit event is defined if two pixels are sharing the quantity of the charge cloud. Triple-hit and quadruple-hit events are for charge distributed between three and four pixel respectively. Figure 2-2 shows an example of the 'accepted' charge sharing patterns. Here it is assumed that the charge cloud size is relatively smaller than the pixel size.

Nonetheless, the split events have the advantage in the image formation since more spatial details of the object under examine can be obtained.

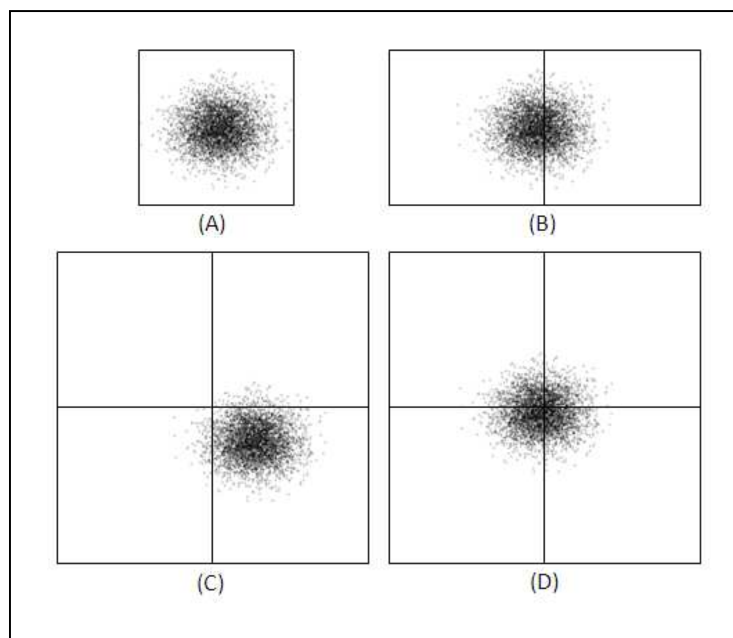

Fig.2-2: Schematic drawing for the main charge sharing patterns in the pixelated detector: (A) Single event,(B) Double-split ,(C) Triple split, (D) Quadruple split event.

The intrinsic resolution of the detector and the pixel size are interrelated factors that govern the spatial resolution of the imaging device. The spatial resolution can be quantified by obtaining the point spread function (PSF) of a point-like object (Fig.2-3, left). To measure the PSF of a monochromatic X-ray, a circular pinhole collimator of a size much smaller than the pixel size can be used. Provided that the pinhole collimator is parallel to the detector surface, the perpendicular X-ray beam leads to accumulate the electrons clouds generated along the track in the pixel array having a round-shape distribution. Figure 2-3-right shows circularly symmetric distribution in a pixel grid and its isotropic surface plot. The maximum intensity in the distribution is in the center and falls exponentially with the distance away from the center.

For a linear and shift invariance system, the spatial distribution of the intensity in the image $g(x_i, y_i)$ is a convolution of the spatial response of the device (PSF) with the spatial distribution of the intensity of the object $f(x_o, y_o)$ in addition to the noise function $\eta(x_i, y_i)$. It is given mathematically as follows:

$$g(x_i, y_i) = \int_{-\infty}^{\infty}\int_{-\infty}^{\infty} PSF(x_i - x_o; y_i - y_o)\ f(x_o, y_o) dx_o dy_o + \eta(x_i, y_i)$$

The spatial resolution can be thus quantified by determining the Full Width at Half Maximum (FWHM) from the bell-like shape of the distribution. The importance of the FWHM value is that the detector is able to distinguish between two closely spaced objects having a distance (R) in the spatial space not less than the FWHM (Fig.2-4).

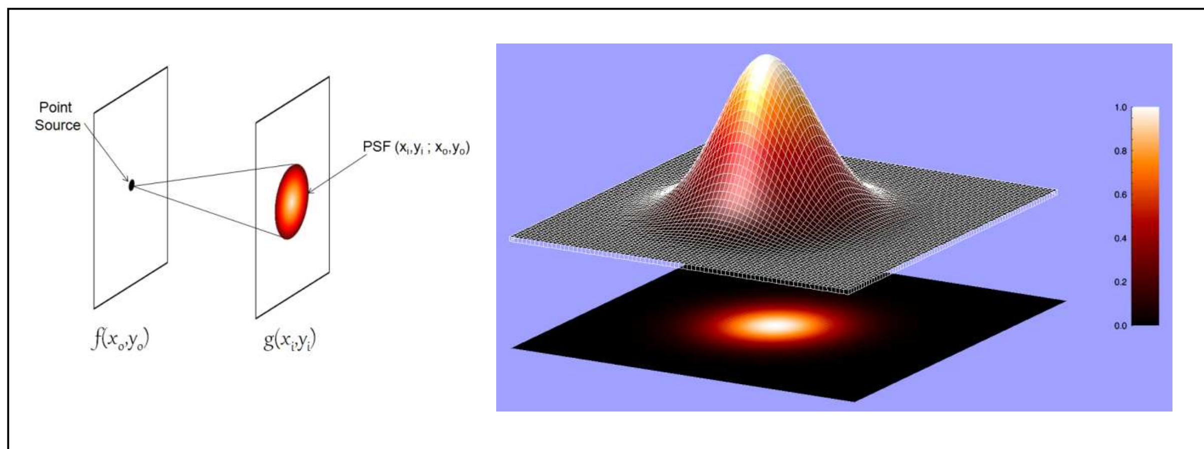

Fig.2-3: Left image shows the PSF which is the projection of the punctual illumination. Right image illustrates the distribution of the PSF in a pixel grid and its corresponding Gaussian distribution shape. The color corresponds to the intensity values.

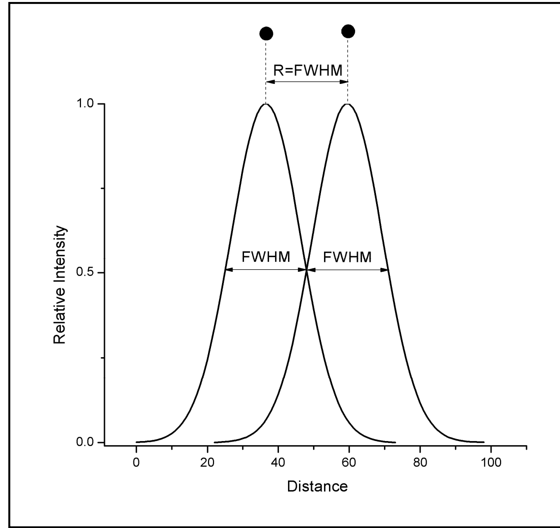

Fig.2-4: Two line profiles from the PSFs of two points having distance R apart. Since the distance is equal to the FWHM, the detector is able resolve them separately.

Practically for relatively big pixel size, the PSF can be possibly achieved if the pinhole collimator is aligned parallel to the center between four pixels and the data is analyzed according to the center of gravity per cloud in the distribution. Elsewhere, it is difficult to directly measure the PSF from the intensity distribution.

The alternative method to the PSF is to use the edge response by having the edge spread function (ESF). The ESF is the efficiency profile obtained in the pixel array as a response to a discrete transition of the pinhole through the edge between two pixels, Fig.2-5. The spatial resolution can be determined from the FWHM of the line spread function (LSF) when taking the derivative of the ESF:

$$ESF(x) = \int_{x}^{\infty} LSF(x^{\prime})dx^{\prime} \tag{2-2}$$

$$LSF\left(x^{\prime}\right) = \frac{d}{dx}\left[ESF(x)\right] \tag{2-3}$$

The main difference between the PSF and the LSF is that the PSF is two-dimensional distribution and the LSF is one-dimensional distribution. The spatial resolution R of a Gaussian distribution PSF and the electrode pitch *p* can be given by:

$$R = 2.356 * \frac{p}{\sqrt{12}} \tag{2-4}$$

where the standard deviation of the distribution is [ref.30]

$$\sigma^2 = \int_{-\frac{p}{2}}^{\frac{p}{2}} \frac{x^2}{p} dx = \frac{p^2}{12} \;\; \rightarrow \;\; \sigma = \frac{p}{\sqrt{12}}$$

For 25 μm electrode pitch in the pnCCD, a spatial resolution of 17 μm can be obtained according to Eq. 2-4. This estimation shows that the spatial resolution can be enhanced beyond the electrode geometry and the actual interaction position in the detector volume has a difference of σ from the measured position.

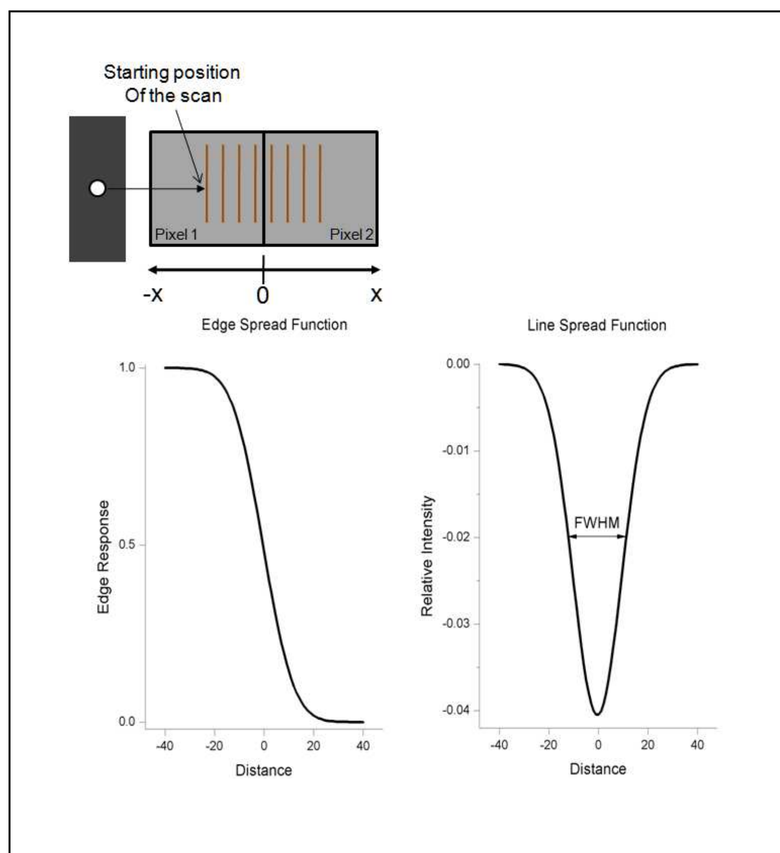

Fig.2-5: The edge response method. The edge spread function is the efficiency profile which results from the scan across the edge between Pixel 1 and Pixel 2. The derivative of the ESF gives the LSF. The spatial resolution of the system is given by the FWHM of the LSF profile.

C. Energy Resolution

The ability of the detector to discriminate two energies close to each other is characterized by the energy resolution of the system and depends essentially on the system noise. Since the signals which are collected by the detector are mainly electrons, the fluctuations in the number of signal electrons are limited by the Fano noise and the readout noise. The measured energy resolution can be characterized by the full width at half maximum of the energy peak. In the spectral analysis, the accepted split events (Fig.2-2) can be summed up to obtain the X-ray spectrum.

D. The Quantum Efficiency

The quantum efficiency (QE) is the fraction of the number of photons hitting the detector and producing useful signals. The efficiency depends on the mass attenuation coefficient, the thickness of the detector, the detector materials and the detector design. The graph of the measured QE values against the phonon energy is plotted in Fig.2.6 for the pnCCD detector [ref.12]. The QE values are measured in the energy range between 0.1 keV and 30.9 keV. The plot shows the materials incorporated in the detector design characterized by the absorption edges in the graph.

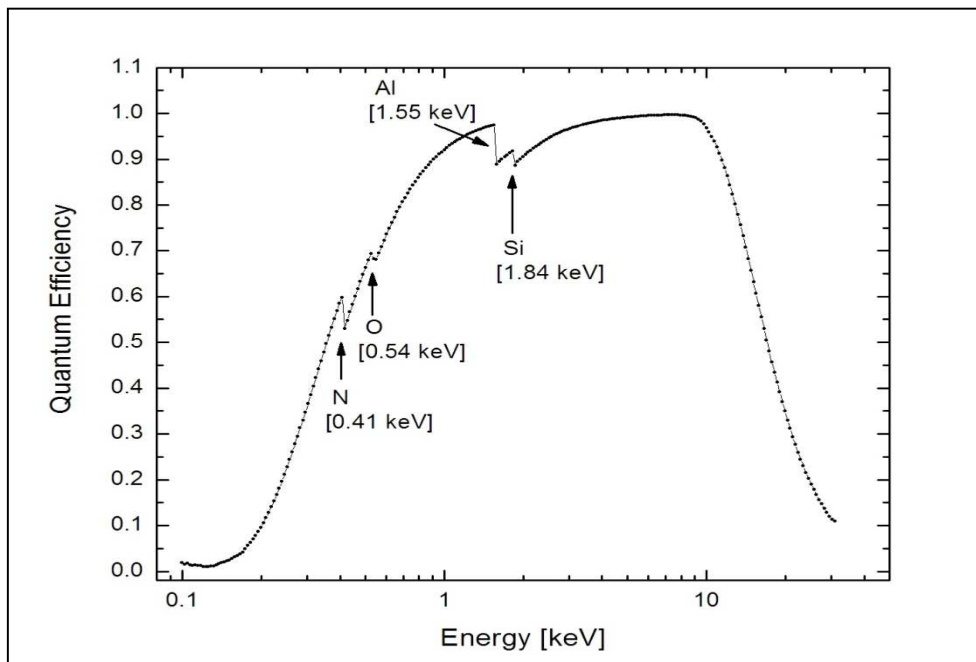

Fig.2-6: Measured quantum efficiency for the pnCCD detector for X-ray between 0.1 and 30.9 keV.

E. Leakage Current and Readout Noise

The pnCCD shows a finite conductivity when there is no radiation exposing it. This results mainly from the thermally generated electrons and holes in the depletion region. This current is called the leakage current and it can be reduced by cooling the silicon chip typically below $-80\ °C$.

When the thermally emitted electrons gain enough energy to move from the valance band into the conduction band, they will drift toward the potential minimum and generate signals in the pixels. The holes on the other side will drift to the backside of the detector. The measured value of the leakage current for fully depleted pnCCD of $450\mu m$ thickness is $1 * 10^{-9}\ A/cm^2$ at a temperature of 300K which is equivalent to $6.24 * 10^9\ electrons/s.cm^2$ [ref.4].

The measurement of the readout noise is described in reference [5]. The high contribution of this noise is originated essentially from the front-end electronics and lower contribution from the CAMEX chip. The total readout noise is often expressed in terms of equivalent noise charge (ENC). For cooled pnCCD, the ENC per pixel (ENC_P) is 2 electrons. For shared events, the overall noise (ENC_{tot}) contribution depends on the number of pixels (N_{pix}) and can be given by [ref.13]:

$$ENC_{tot} = ENC_p * \sqrt{N_{pix}} \tag{2-3}$$

By recording a number of “dark frames”, the offset value per pixel accumulated from the leakage current and the electronic noise can be determined via an *analysis-software package* which includes algorithms to perform mathematical operation on the recorded data. By this means, the offset is subtracted from the measured signals in each frame [Chapter4-D].

F. Common Mode Noise

The pnCCD is read out in columns of which each row is shifted towards the readout nodes and processed (amplified/ filtered) simultaneously. Tiny variation in the voltage supplying the readout electronics might induce noise which will affect row of pixels with the same value. This common deviation is determined by finding the median value per line after subtracting the offset. The common mode correction is running and subtracted in every signal frame data.

G. Charge Transfer Noise

The signal charge is moved from pixel to pixel when transferred to the readout anode. The charge transfer noise arises from the number of electrons that are lost from the charge packet during the transfer mechanism. This means that the signal charge is reduced and the number of electrons lost remains in the pixels' trail. If N_{shift} transfers occur, then the RMS is calculating the fluctuation in the successive signal charge due to the charge loss as follows:

$$RMS_{transfer} = \sqrt{CTI * N_{ele} * N_{shift}} \quad (2\text{-}4)$$

where CTI is the charge transfer inefficiency ($CTI = 1 - CTE$) and N_{ele} is the number of electrons in the charge packet. The typical value of the charge transfer efficiency (CTE) for the pnCCD is close to one with CTI in the order of 10^{-5} [ref. 13].

H. Pile-up Events

The pnCCD is less damage to the intense synchrotron beam due to its front-side design. However, high photon flux requires relatively fast readout electronics. The frame rate of the detector is 133Hz which is quite slow for dynamics measurements. The main limitation arises with the amount of the pile-up events and consequently the number of rejected events.

Pile-up events occur when more than one photon per pixel per frame is detected at once. Therefore, the generated electrons will combine and their measured energy is summed up.

The high flux delivers higher photon rate (Φ) in the detector. The accumulated rate per pixel (N_p) in a given integration time (Δt) is given by $N_p = \Phi * \Delta t$ with the relative precision due to the inherent photon statistics:

$$\frac{\Delta N_p}{N_p} = \frac{1}{\sqrt{N_p}} = \frac{1}{\sqrt{\Phi * \Delta t}} \quad (2\text{-}5)$$

For time-resolved measurements, the high photon rate can be used for improved precision or shorten the integration time at the same precision.

The probability of the pile-up events for a given photon rate can be estimated from the Poisson distribution as follows:

$$P(k) = e^{-\Phi} * \frac{\Phi^k}{k!} \qquad ; \ k = 0,1,2, \ldots. \tag{2-6}$$

For example, if a monochromatic X-ray beam is collimated such that a photo rate of 0.2 γ/s reached the detector, then the probability to detect: no events ($k = 0$) is 0.8187, single events ($k = 1$) is 0.1637, pile-up of two photons is 0.01637, and pile-up three photons is 0.00109 . If the incoming rate is 2.0 γ/s , then the probability to detect pile-up events is 0.2707 and 0.1804 for two and three events respectively. Therefore, the probability of the pile-up events increases with the increasing the photon rate and with the long integration time.

At high photon flux, the energy spectrum of a monochromatic X-ray beam includes the first harmonic peak which corresponds to those 'isolated' photons and the pile-up peaks at energy positions equal their pile-up multiplicity.

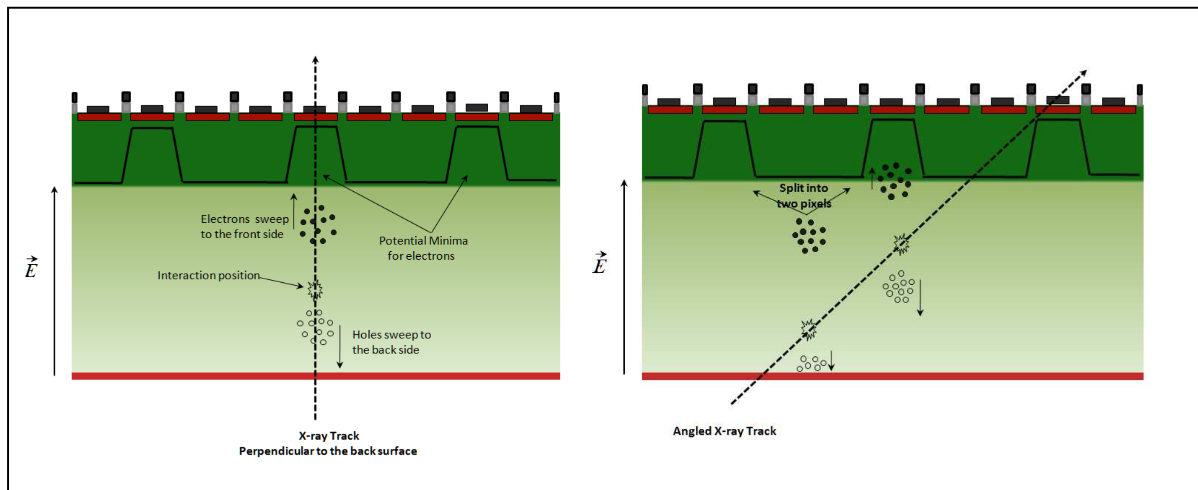

Fig.2-7: Perpendicular versus inclined x-ray track. The distribution of the charges in the pixel array depends on the incident angle.

I. Parallax Effect

Commonly a substantial semiconductor thickness is required to achieve high quantum efficiency. The thickness of the detector may lead to geometrical effects that degrade the spatial resolution of the object to be imaged when the X-ray beam penetrates the detector with an oblique angle with respect to the direction perpendicular to the detector entrance surface, as shown in figure (2-7). This effect is called parallax effect and it results from the attenuation of the incoming photons along the oblique track in thick

detector. This leads to a spread of the charge clouds into a number of pixels corresponding to the beam penetration angle as a function of the interaction depth. Due to this effect, the images in the detector will exhibit degradation in the spatial details such as blur and edge artifacts.

For diffraction experiments, synchrotron radiation offers high intense and parallel monochromatic source of X-ray on a small crystal. This is important for extracting the diffraction information from a given sample crystal. On the other hand, parallax-free image and high spatial resolution detector allow resolving Laue spots which are spatially very close because the size of the spots formed in the pixel array is the projection of the cross section of the crystal convoluted with the PSF of the detector.

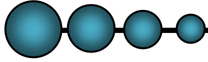

3. Theoretical Computation and Expectations

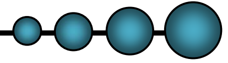

This chapter implies literature-based formulas describing the process from the moment the electron clouds are created in the silicon bulk till they reach the potential minima. The dynamic expansion of the electron cloud during the collection time is consequently formulated to establish a numerical model which gives an expectation for the size of the charge cloud at the end of the collection time. The model is a stepwise evaluation of the dynamic expansion visualized as if the detector bulk is partitioned into subparts and the incident photons are attenuated exponentially throughout.

A. The Detection of the X-rays

The pnCCD detector is utilized to detect X-ray photons in the energy range of 100eV up to effectively 30 keV as depicted in figure2-6. The dominant interaction mechanism in this energy range is the photoelectric effect, Fig 2-1.The incident X-ray photon therefore transfers all its energy to an electron in the inner shells of the silicon atom. Thereby the photoelectron is ejected with a kinetic energy E_{ele} given by the following equation:

$$E_{ele} = E_{\gamma} - E_{B} \tag{3-1}$$

where E_{γ} is the energy of the monochromatic photon and E_{B} is the binding energy of the photoelectron ejected from the K-shell, and it equals 1.84 keV for the silicon atom. The direction of the ejected photoelectron is mainly parallel to the electric field component of the incoming X-ray [15]. The photoelectron loses its energy by inelastic collision with orbital electrons of which a number of e-h pairs are consequently created. The process will continue until the photoelectron and all the electrons come to rest. The initial atom being in the excited state is relaxed by the transition of an electron from the upper shells. Consequently, the difference in energy between the two shells is emitted as a characteristic X-ray or Auger electron and may create more e-h pairs if absorbed nearby.

If the average energy (w) is the minimum energy required to generate an electron-hole pair, then the total number of electrons N_{ele} produced from the interaction of a photon of energy (E_γ) is

$$N_{ele} = \frac{E_\gamma}{w} \tag{3-2}$$

The statistical fluctuation in the generated number of electrons follows Poisson distribution with standard deviation of

$$\sigma_{N_{ele}} = \sqrt{F * N_{ele}} \tag{3-3}$$

where F is the Fano factor and it is an empirical attempt to adjust the observed variance to the Poisson variance. At room temperature, the Monte Carlo data for the pair creation energy (w) is 3.64 eV and Fano factor (F) is 0.115 [ref.16].

Two measurements were done to determine the mean creation energy and the Fano factor. The first measurement was performed for soft x-rays using a silicon $n^+n^-p^+$ diode with integrated readout electronics and the synchrotron radiation utility [17]. It shows that the pair creation energy rises from 3.64 eV at 1400 eV to 3.74 eV at 350 eV for room temperature, and at 140 K it rises from 3.72 eV at 1400 eV to 3.93 eV at 300 eV. Besides, the results show that the Fano factor has distinct energy dependence and at small X-ray energy they also show temperature dependence.

Another measurement was carried out using silicon p-i-n diode in temperature range 80-270 K and the X-ray energy 5.9keV [ref. 18]. A pair creation value of $3.73 \pm 0.09\ eV$ with a gradient of $-0.0131 \pm 0.0004\%\ K^{-1}$ was found and a Fano factor of 0.118 ± 0.004 is also reported.

If a large number of events are accumulated in the detector provided that σ_C defining the charge loss during the shifting process and σ_A defining the electronic readout noise, then the energy response function will be a Gaussian shaped peak with an energy resolution R (FWHM)given by :

$$R(eV) = 2.35 * w * \sqrt{\sigma_{N_{ele}}^2 + \sigma_C^2 + \sigma_A^2} \quad . \tag{3-4}$$

Considering the pnCCD detector is cooled enough such that the leakage current is negligible, the ENC is 2 e^- and the CTE ≈ 1, the FWHM of 5.0 keV energy peak will not be better than 111 eV for single hit events when assuming a values of 3.70 eV and 0.118 for the pair creation energy and Fano factor respectively.

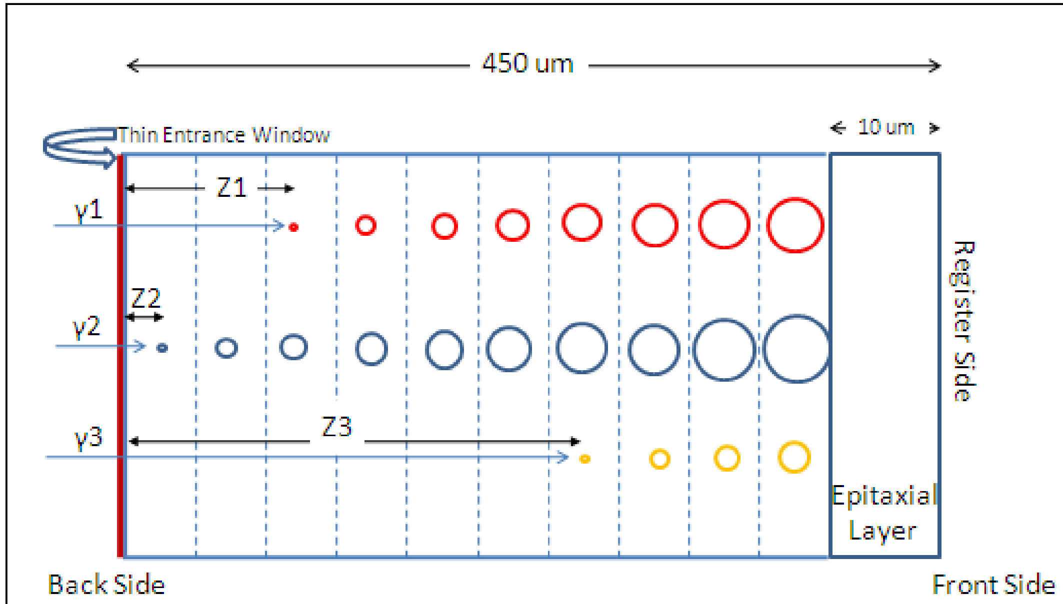

Fig.3-1: Sketch showing three photons of the same energy interact at different depths (Z1,Z2,Z3) and creating electron clouds (first circles) in the silicon bulk and the following circles from any interacting position compromise the process of expansion during the drift to the epitaxial layer.

B. The Computation Process

The goal is to calculate the size of the electron cloud generated from the interaction of a monoenergetic X-ray photon (E) when reaching the potential minimum in the fully depleted pnCCD detector provided that the photon beam strikes the backside of the detector.

To follow the process, the silicon bulk will be partitioned into **N** transverse bins of equal size (S_N) and the monoenergetic beam has initial intensity $\boldsymbol{I_\circ}$ attenuated exponentially in the bulk thickness (w_d). The probability that the incoming photon interacts at given depth (z) is given by eq. 2-1. The distance from the interaction location to the epitaxial layer defines the electron's drift distance (DD_e) which is ($w_d - z$) and the distance to the backside is the hole's drift distance ($DD_h = z$). Figure 3-1 illustrates an example of three X-ray photons ($\gamma_1, \gamma_2, \gamma_3$) of the same energy having different interaction position (z_1, z_2, z_3).

The total number of absorbed photons $\boldsymbol{I_A}$ at depth (z) is given by:

$$I_A(z) = I_\circ(1 - EXP\ (- \mu_l(E) * \ z) \qquad (3\text{-}5)$$

Where μ_l is the linear attenuation coefficient for silicon at a specific photon energy and it has the unit of μm^{-1} if the interaction depth (z) in μm.

C. Charge Collection Time

When the absorbed photon imparts all its energy in the silicon atom, a number of electrons will be ejected into the conduction band and consequently an equal numbers of holes are left behind in the atomic shells. The transportation of the electrons is carried out through the drift and diffusion processes.

The presence of high electric field in the pnCCD detector will primarily be able to separate the electrons and holes before they recombine. The electrons will be then subjected to the electric field force to traverse the bulk toward the registers side in a direction parallel to the electric field lines. On the other hand, the holes will drift to the opposite side until they reach the negatively biased backside and get absorbed.

The diffusion takes place in a non-vanishing concentration gradient. The electrons in this case tend to spread out randomly in an attempt to decrease their concentration from the region of higher concentration into the lower one. The dynamic of this process is due to the thermal energy of the electrons.

The movements of the charge carriers inside the semiconductors are perturbed by different scattering mechanism, mainly the lattice scattering and impurity scattering. The lattice scattering is caused by the collision of the charge carriers with the thermal induced vibrational motion of the crystal. The crystals periodically oscillate with amplitude much smaller than the lattice spacing, quantized by the so called phonons. The total energy and the momentum in this collision are conserved and the phonons change the magnitude and direction of the electrons. The kinetic energy gained by the electrons from the acceleration in the electric field is lost by the scattering event. The electrons are further accelerated in the direction of the electric field and scatter again. Since the impact time in this collision is much smaller than the transport time, the transported electrons are always in equilibrium with the lattice structure and their velocity is only a function of relatively “low” electric field. The lattice scattering is temperature dependent; therefore increasing the crystal temperature causes the transported electrons to face more scattering. Impurity scattering is caused by the presence of ionized impurity atoms in various positions in the crystal lattice. The net charge of the ionized impurity atoms either repeals or attracts the transported electrons passing nearby which consequently changes the direction of the electrons. The faster the electrons transportation, the less time the electron spends in the vicinity of the ionized impurities [9].

The mobility of the electron (μ_e) in the semiconductor is a measure of how easily electrons are moving in a semiconductor material under the influence of the applied electric field, the applied temperature, and the doping concentration. Different measurements and simulations concerning the mentioned factors affecting the carrier mobility are thoroughly discussed in reference [ref. 19].

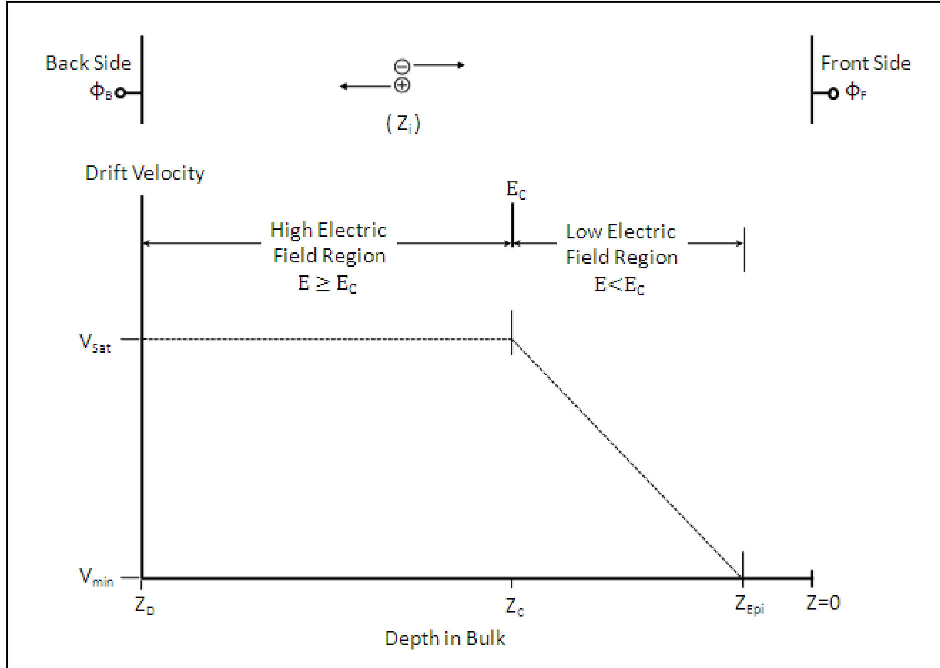

Fig. 3-2: Drawing shows the dependency of the electron drift velocity on the applied electric field in the detector bulk.

The critical electric field value E_C for the electrons in silicon can be defined as a function of temperature (T), [ref.: 20 & 21] and can be used to make the distinction in the magnitude of the electron mobility as shown in Fig. 3-2.

$$E_C = 6.98 * 10^3 \frac{V}{cm} * \left[\frac{T}{300\ K}\right]^{1.55} \tag{3-6}$$

For the pnCCD applied temperature of 193 K, the critical electric field value is 3528.8 V/cm. Therefore for constant mobility (μ_n), the velocity (v) of an electron at position z with respect to z_C in low electric field region is given by

$$v(z) = v_{sat} - \mu_n * E(z) = v_{sat} - \mu_n \frac{e\, N_D(z)}{\varepsilon}(z - z_C) \equiv v_{sat} - (z - z_c)/\tau_n \tag{3-7}$$

where τ_n is defined as a characteristic collection time,[$\tau_n \equiv \varepsilon / e * N_D * \mu_e$] and v_{sat} is the saturated drift velocity. The collection time (t) required by the electron cloud to drift from the position of its generation (z_i) to the epi-layer depth (z_{epi}) by the influence of uniform and low electric field ($E < E_c$) is:

$$t(z) = \int_{Z_i}^{Z_{Epi}} \frac{1}{v(Z)} dz = \int_{Z_i}^{Z_{Epi}} \frac{1}{v_{sat} - \tau_n(z - z_C)} dz = -\frac{1}{\tau_n}\left[\ln v_{sat} - \tau_n(z - z_C)\right]_{Z_i}^{Z_{Epi}}$$

$$t(z) = -\frac{\varepsilon}{\mu_n\, e\, N_D(z)} \ln\left[\frac{v_{sat} - \tau_n(z_{epi} - z_c)}{v_{sat} - \tau_n(z_i - z_c)}\right] \tag{3-8}$$

Meanwhile the electron cloud generated in the high electric field region ($E \geq E_c$) has the following collection time (t_{tot}):

$$t_{tot} = \frac{z_i - z_c}{v_{sat}} + \frac{-1}{\tau_n} \ln\left[\frac{v_{sat} - \tau_n(z_{epi} - z_c)}{v_{sat}}\right] \qquad (3\text{-}9)$$

The empirical formula which relates the dependency of the electron mobility at low electric field on the applied temperature and the doping concentration has been derived based on the experimental data and modified Brooks-Herring theory of mobility [ref.22]:

$$\mu_e\left[\frac{cm^2}{V.s}\right] = 88\left[\frac{T}{300K}\right]^{-0.57} + \frac{7.4*10^8*T^{-2.33}}{1+\left[\frac{N_D}{1.26*10^{17}*\left[\frac{T}{300K}\right]^{2.4}}\right]*0.88*\left[\frac{T}{300K}\right]^{-0.146}} \qquad (3\text{-}10)$$

where T is the temperature in Kelvins. For lightly- doped donor concentration (N_D) in the pnCCD silicon bulk and temperature of 193 K, the denominator in the second term of Eq. 3-10 is roughly one. Therefore, the influence of the doping concentration on the electron mobility is negligible and the electron mobility functions as the temperature. Equation 3-10 can be reduced to:

$$\mu_e\left[\frac{cm^2}{V.s}\right] = 88\left[\frac{T}{300K}\right]^{-0.57} + 7.4 * 10^8 * T^{-2.33} \qquad (3\text{-}11)$$

The mobility of the electrons according to Eq. 3-12 at 193 K temperature is 3612 $cm^2/V.s$. If the room temperature (300K) is substituted in the equation, then the electron mobility is 1340 $cm^2/V.s$. The published values of the electron mobility at room temperature show some differences such as a value of 1438 $cm^2/V.s$ was in [ref. 20] and 1350 $cm^2/V.s$ shown in [ref.23].

At higher electric field, exceeding the critical electric field value, the proportionality between the drift velocity and the electric field is no longer retained since the accumulated kinetic energy of the electron is gradually lost by additional scattering which in turn decreases the electron mobility. Consequently the drift velocity will saturate to a value equal the average thermal velocity. The expression widely used to model the mobility–electric field dependency for electrons [ref.19] is:

$$\mu_e(E) = \frac{\mu_n^o}{(1+[\frac{E_n * \mu_n^o}{v_n^{sat}}]^\beta)^{1/\beta}} \qquad (3\text{-}12)$$

where β is defined from the fitting experimental data[ref.20]:

$$\beta = 1.11 * \left[\frac{T}{300\,K}\right]^{0.66}$$

The variation of the saturated drift velocity over the lattice mobility is temperature dependent which can be fitted to [ref. 20]:

$$v_e^{sat} = 1.0 * 10^7 \ \frac{cm}{s} * \ [\frac{T}{300\ K}]^{-0.87} \qquad (3\text{-}13)$$

D. Charge Cloud Expansion

This section discusses the formulas which are used to estimate the spatial size of the electron cloud generated from the interaction of the X-ray beam once reaching the epitaxial layer. The initial cloud size propagates in size during the migration toward the potential minimum due to the diffusion process and the mutual electrostatic repulsion between the electrons constituting the cloud.

D.1-Primary Charge Cloud Size

The range R_{ele} of the primary electron ejected with kinetic energy (E_{ele}) is estimated for silicon using the range-energy relation [ref. 24] :

$$R_{ele}(\mu m) = 0.0171\ E_{ele}^{1.75} \qquad (3\text{-}14)$$

where the E_{ele} in keV. The generated initial electron cloud has a spherical shape with a Gaussian profile of initial 1σ radius given by the following equation [ref. 25]:

$$\sigma_{init} = 0.257\ R_{ele} \qquad (3\text{-}15)$$

Substituting Eq. 3-14 in Eq. 3-15 gives the primary charge cloud radius:

$$\sigma_{init}(\mu m) = 0.0044 * \ (E_\gamma - E_B)^{1.75}. \qquad (3\text{-}16)$$

The primary electron cloud is very small for all energies resolved by the pnCCD detector and consequently can be considered as a point-like for further discussion.

D.2- The Diffusion Process as a Random Walk

The movement of the electron cloud inside the crystal structure is disturbed by the scattering process and therefore the migration is randomly occurred. The treatment of charge expansion due to the drift-diffusion behavior is assuming a series of random walk steps for the electrons based on the derivation described in

reference [26]. The solution depicts 1D spreading that can be extended afterward to the 2D case. Considering the direction of the electron cloud propagation is in the z-axis which is the direction of the electric field in the detector, the lateral expansion will then be assumed in the other axes.

A simple model allows the estimate of the diffusion is to consider the steps of the electron's propagation are independent either to the left or to the right along the x-axis. If we take into account the mean free path of the electron (λ), then the step length (s) between two successive scattering will vary randomly with probability of $e^{-e/\lambda}$. However the derivation is relatively simplified by assuming a constant step length which is equal to the mean free path. If the total number of steps taken by the electron during the collection time is N of which $N = n_R + n_L$ where n_R are steps to the right ($+x$) and n_L are steps to the left ($-x$), then their difference will be: $m = n_R - n_L$.

The electron's net displacement in the $+x$ direction is then

$$n_R\lambda - n_L\lambda = m\lambda .$$

Since the steps are independent and the probability to step left or right is equal (p = 1/2), the probability of having a displacement $m\lambda$ is given by a binomial distributed $P(n_R; N)$:

$$P(n_R; N) = \frac{N!}{(n_R!)(N-n_R)!} * \left[\frac{1}{2}\right]^{n_R} * \left[\frac{1}{2}\right]^{n_L}$$

If this distribution is centered at $m = 0$, then the variance in m is $(\overline{m^2} - \overline{m}^2)$. The variance of the distribution of displacement x is equal to the step length λ times the variance in the number of steps:

$$\sigma^2 = \overline{x^2} = \lambda^2 N$$

The number of steps is the collection time (t) divided by the collision time (t_c): $N = \frac{t}{t_c}$. Therefore,

$$\sigma^2 = \frac{\lambda^2 * t}{t_c}.$$

If the material-dependent diffusion constant (D) is defined to be $\frac{\lambda^2}{2t_c}$, then the radius of the electron cloud at the end of the collection time is:

$$\sigma = \sqrt{2Dt} \tag{3-17}$$

This formula is called Einstein relation. The diffusion constant in the formula is $D = \frac{KT}{Q_e}\mu_e$, where k is Boltzmann constant, T is the temperature, Q_e is the charge of the electron and μ_e is the electron's

mobility. The electron therefore spreads out with a variance proportional to the collection time and the electron cloud following this model will have a distribution of fixed mean. For large number of N steps from all the electrons in the charge cloud, the Gaussian distribution will be an approximation to the binomial distribution:

$$P(x,t) = \frac{1}{\sigma(t) * \sqrt{2\pi}} EXP(- \frac{x^2}{2\,\sigma(t)^2}) \tag{3-18}$$

In two dimensions, the expansion is then given by

$$\sigma_r^2 = \sigma_x^2 + \sigma_y^2 = 4Dt$$

The symmetric 2-D Gaussian distribution reads:

$$P(r,t) = \frac{1}{2\pi\,\sigma(t)^2} EXP(- \frac{(x^2 + y^2)}{2\,\sigma(t)^2}) \tag{3-19}$$

D.3- Mutual Electrostatic Repulsion

The drift-diffusion process occurs regardless the number of electrons generated from the incident photons and it is totally material dependent. The numbers of the electrons play a role in the mutual electrostatic repulsion of which the more electrons include in the cloud the bigger the Coulomb force generated. The effect of the mutual electrostatic repulsion within the electron cloud has been investigated experimentally and theoretically and it shows a significant contribution in broadening the charge cloud in the silicon drift detector [ref.27]. In the theoretical analysis the assumption of a spherical symmetry of the charge cloud is considered. If $n(r)$ is the volume charge density of N_{ele} electrons, then the total charge $Q(r)$ contained in a sphere of radius R at time t is

$$Q(r,t) = \int_0^R q * n(r) * 4\pi r^2 dr$$

The electric field of a given stationary charge distribution (external field is zero) is

$$E(r,t) = \frac{Q(r,t)}{4\pi\varepsilon r^2}$$

Substituting $Q(r,t)$ and $E(r,t)$ in the repulsion term of the continuity equation one gets:

$$\frac{\partial Q(r,t)}{\partial t} = -\frac{\mu_n}{4\pi\varepsilon} * Q(r,t)\frac{\partial Q(r,t)}{\partial r} * \frac{1}{r^2}$$

The following solution is obtained:

$$Q(r,t) = \frac{R^3}{\frac{3 * \mu_n}{4\pi\varepsilon} * t}$$

This solution still needs to include the amount of charge ($q * N_{ele}$) composing the charge cloud and to let the charge distribution not to extend to infinity for any finite time. The physical solution can then be found by containing the total charge in the formula and limiting the region reached by the electrons at time (t) with a sphere of radius R_o, by introducing a step function to the formula above. Therefore, the maximum radius of the charge cloud results from the electrostatic repulsion is:

$$R_o(t) = \sqrt[3]{\frac{3\mu_e q}{4\pi\varepsilon} * N_{ele} * t} \tag{3-20}$$

where μ_e is the mobility of the electron, q is the electron charge, and ε is the multiplication of the relative permittivity in silicon and the permittivity in vacuum.

E. Numerical Model of the Charge Spread

This section aims to model the charge cloud expansion from the formulas 3-16, 3-17 and 3-20 as a convolution process carried out in a picoseconds time steps during a given collection time based on the fact that the diffusion process and the electrostatic repulsion are dependent process and coupled during the drift. The picoseconds time steps is an attempt to simulate the coupling resulting from the expansion of the initial cloud size as a square root of time in the diffusion process and in the case of the electrostatic repulsion as a cubic root of time. The computation proceeds in the following sequence:

Part One: Preparation

Stage1:

■ The detector bulk is visualized as if it is divided into an integer number of slabs.

■ Initialize the number of photons to be involved in the computation.

■ Calculate the number of absorbed photon in each slab according to Eq. 3-5.

Stage2: Execute for each photon

■ From the center of each slab to the epitaxial layer, calculate the collection time using Eq. 3-8 or 3-9 according to the conversion position of the photon.

■ Calculate the initial cloud (σ_{init}) size for the given photon energy,Eq. 3-16.

■ Calculate the corresponding time (T_{init}) of σ_{init} from Eq. 3-20.

■ Provide the picoseconds step time (Δt)

■ Calculate the radius of the charge cloud due to the diffusion process (σ_D) corresponding to the step time ($\Delta t = 10^{-12} sec$) provided the constant mobility value and temperature of 193 K.

$$\sigma_D = \sqrt{2\frac{KT}{Q_e}\mu_e * \Delta t}$$

■ The input time (T_{in}) in the convolution process is

$$T_{in} = T_{init} + \Delta t$$

■ Provide the number of iterations ($steps$) for the convolution process:

$$steps = \frac{Collection\ Time}{\Delta t}$$

Part Two: Convolution per charge cloud

Repeat the sequence till the number of $steps$ is reached

P**1-** Calculate the charge cloud radius (R_{var}) via Eq. 3-20 corresponding to the input time (T_{in}).

P**2-** Calculate the RMS value: $RMS = \sqrt{R_{var} + \sigma_D}$

P**3-** Calculate the time corresponding to the RMS value (T_{RMS}) from Eq. 3-20.

P**4-** Update the input time (T_{in}) such that : $T_{in} = T_{RMS} + \Delta t$ and return to point P**1**

This part will terminate with σ_{CC} corresponding to radius of the charge cloud at the end of the collection time.

Part Three: The Gaussian Distribution

▲ Make a regular grid of specific dimensions, e.g. 375x375, such that the cell size is $1\mu m$ and the central pixel of the grid is P_c.

▲ Distribute the charge cloud of radius σ_{CC} in the grid at $P_c \equiv [x_o, y_o]$ with the Gaussian distribution

$$G(x,y) = \frac{1}{2\pi\sigma_{CC}^2}\, e^{-\left[\frac{(x-x_0)+(y-y_0)}{2\sigma_{CC}^2}\right]}$$

▲ By adding up the charge clouds coming from all slabs, a symmetric 2D PSF weighted over the number of clouds per slab (PSF) is generated.

$$PSF = \int N_{ele} * Q_e * G(x,y)$$

▲One dimensional scan profile can be created by integrating over the PSF provided the minimum and the maximum limits over a range of scan steps $[x_i = 0,1,2, \ldots ,150]$ when starting from the pixel $P_c - 75$.

$$Amplitude\ per\ step|_{P_c} = \int_{x_i}^{x_i+75} PSF\, dx \qquad (3\text{-}21)$$

The charge cloud size for a given photon energy will be then the FWHM of the differentiated peak from scan profile (Eq-2-3).

F. Expectations from the Numerical Model

The input parameters used in the computation are the operation temperature 193 K of the detector , the depletion voltage of -230V and the registers voltage of -17V. The input number of photons to be processed is 10^3. The coordinate is established such that the z-axis has the origin 0 at the front side and go through $450\mu m$ till the back side.

Different monochromatic energies are introduced. As illustrated in the plots in figure 3-3, the log-scale of the y-axis refers to the total number absorbed photons in a given slab versus the attenuation length. The attenuation length is the distance from the backside to the position where the photon is converted and assumed to be presented at the center of the slab. If 10^3 incoming photons of $5keV$ are hitting the detector from the backside, then the total number of photons that are attenuated in the first $30\mu m$ is 819. Proceeding with number of photon left (181 photons), the next slab will take up 148 out of them.

Comparing the incoming X-ray energy with the attenuation length, the photons of $5keV$ will be completely attenuated within the first 135 μm measured from the backside. Meanwhile, higher energetic photons will have the chance to penetrate further and to be attenuated along the whole detector thickness or they may leave the detector without interaction.

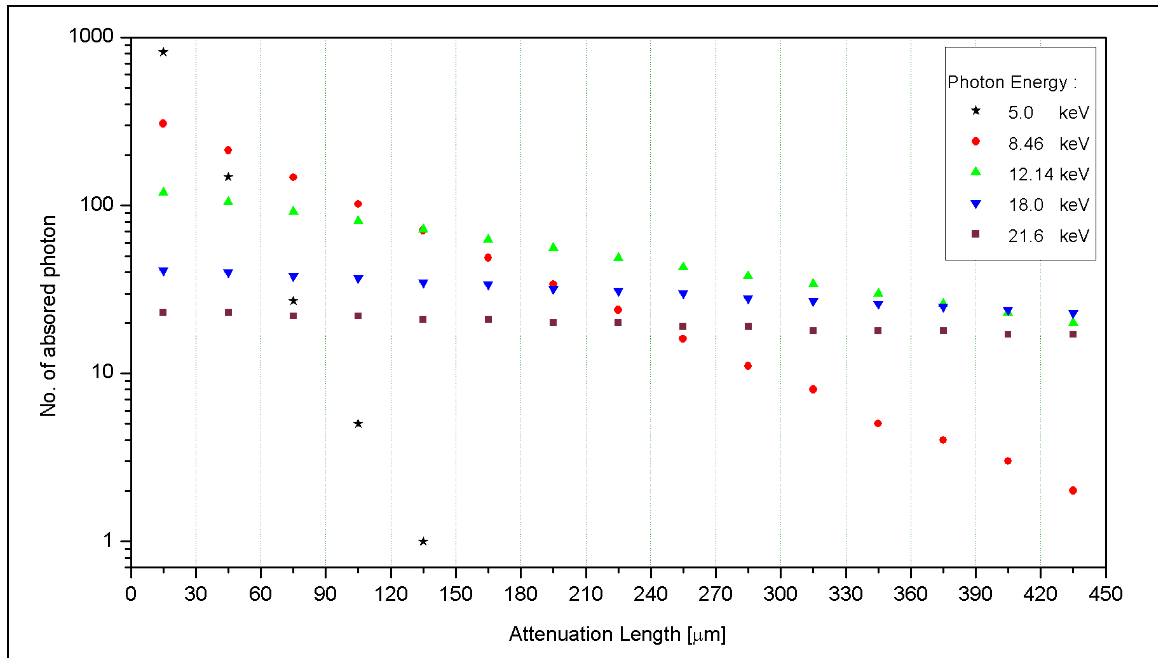

Fig.3-3: The probability of photon absorption along the detector bulk as if the bulk is divided into 30 μm slabs. The total number of the incoming photons is 1000.

Now if the photon will be converted in the first $30\mu m$, for example, a charge cloud will be generated. The electric field force will drive the cloud toward the epitaxial layer. The distance from the center of the slab to the bulk-epitaxial interface represents the drift length. The plot of the drift length against the collection time is depicted in Fig 3-4 for the given slabs. This figure shows that the maximum drift time for the charge cloud is around $3ns$ if it will cross the $440\mu m$ bulk thickness. The drift time decreases as the interaction position gets closer to the epitaxial layer. It shows also a linear drop up to the $120\mu m$ from the epitaxial layer because of the saturated velocity of the electrons. The generated charge clouds will drift to the epitaxial layer and they will grow in size as shown in section F on this chapter. The RMS values of the cloud are plotted against the drift length as depicted in Fig. 3-5 for different photon energy. For example, the photon of 5keV having drift length of $440\mu m$ will reach the epitaxial layer with a radius of $10.37\mu m$.

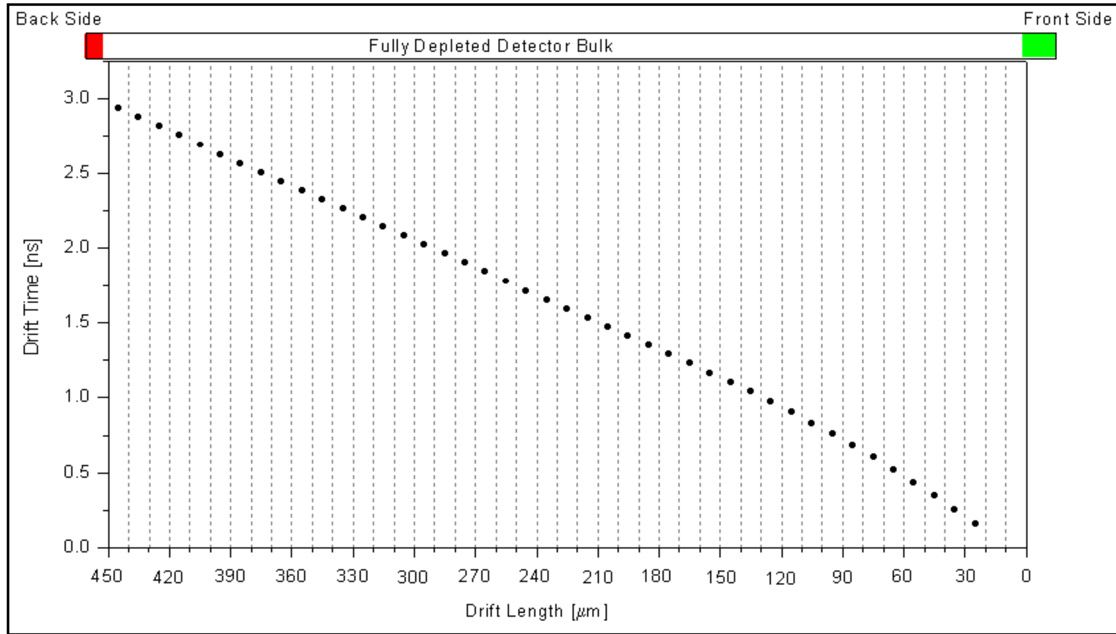

Fig.3-4: The calculated charge collection time versus the drift length.

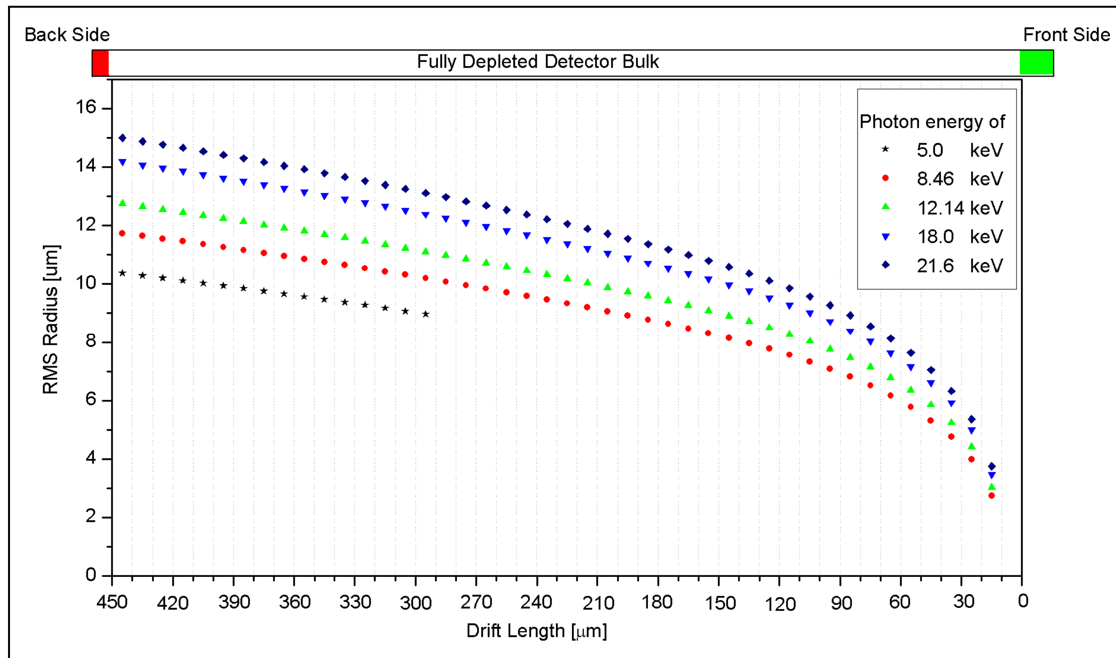

Fig.3-5: The calculated RMS values of the charge cloud as a function of the drift length.

F.1- The Scan Profile for Perpendicular Incoming Beam

Since the radius of the charge clouds thus estimated, the case study when the incoming beam hits the detector perpendicular to the back surface, Fig 2-7(left), leads to project the charge clouds into one position in the pixel array. When the scan is carried out as described in Eq.3-21 on the PSF which is accumulated from all the Gaussian distributed charge clouds, a scan profile contains the scan position versus the normalized charge amplitude can be plotted as illustrated in Fig. 3-6 (top). In this figure different photon energies are simulated separately.

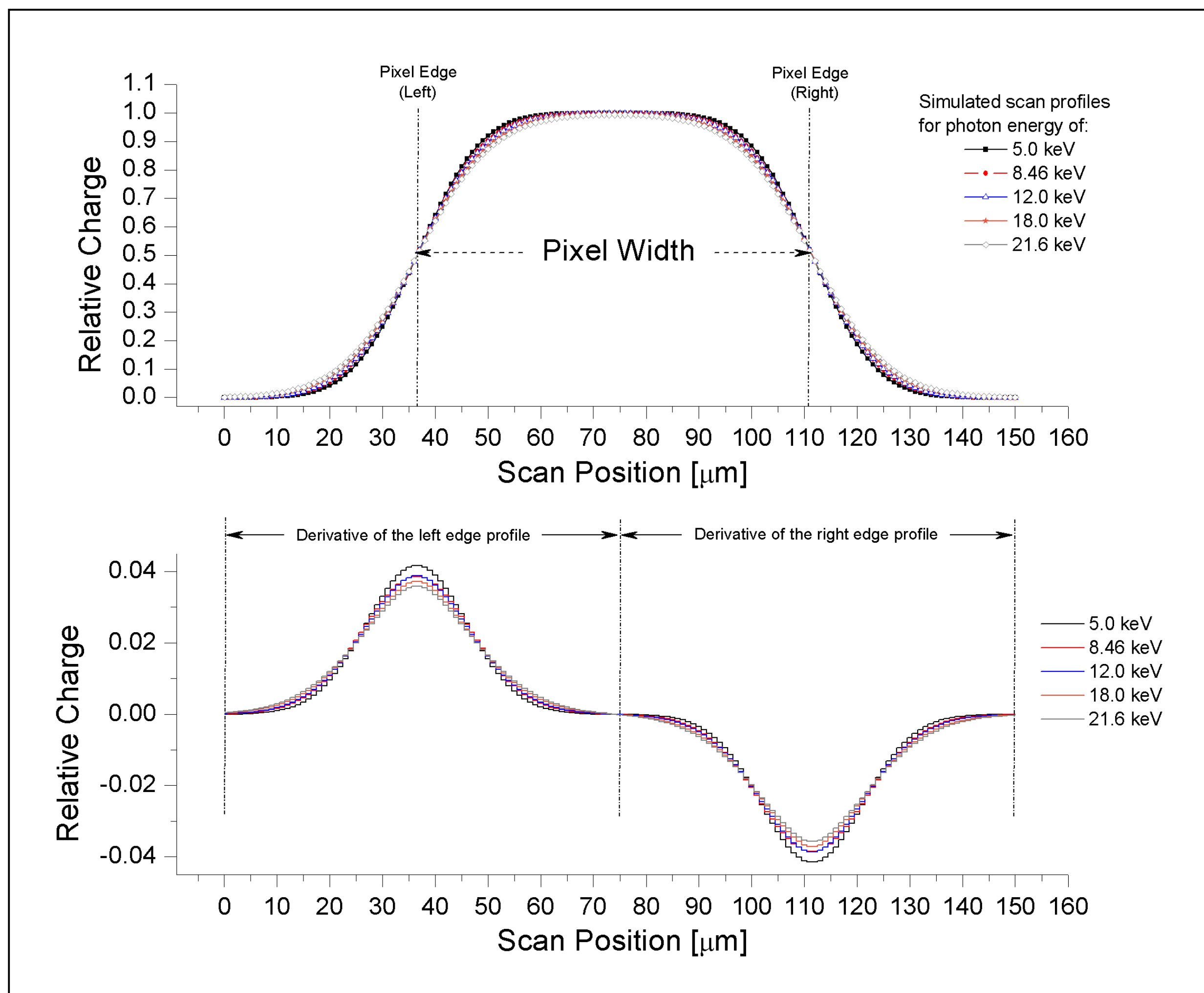

Fig.3-6: Top, the simulated scan profiles for different photon energies. Bottom, the LSF of the left and the right edges obtained from the derivative of the edge profiles.

Differentiating the sigmoid (Edge spread function) in right side of the scan profile or on the left side will give the LSF, Fig. 3-6 (bottom). The corresponding RMS radius (σ) of the charge cloud as a function of the given photon energy is:

photon energy (keV)	RMS of electron Cloud σ_{Tot} (μm)
5.0	9.601
8.46	10.334
12.0	10.779
18.0	11.435
21.6	11.953

F.1- Statistical Fluctuations in the Calculated RMS Resolution

In reality, even for the same photon energy, statistical variations in the number of generated electrons in the detector result in relatively different electron clouds. Since the collection time depends on the distance of the interaction position from the epitaxial layer, the fluctuations in the collection time for a given number of electron clouds result in a PSF that is quite wide or narrow. For any reasons of statistical variation, a weighting value (ψ) can be introduced in the simulation model as an attempt to define the confident level of the measured RMS resolution. Therefore, Eq. 3-20 can be written as follows:

$$\sigma_R = \psi * \sqrt[3]{\frac{3\mu_e Q}{4\pi\varepsilon} * N_e * t}$$

The values of ψ that are introduced in the simulation are :

$\psi = 0.8 ; 0.9 ; 1.0 ; 1.1 ; 1.2$

The numerical simulation is carried out again as described in section E of this chapter. The resulting edge profile is differentiated and a proper fit is then applied on the LSF. The output values are shown in Table 3-1 and the plotted as depicted Fig. 3-7.

Finally for a maximum collection time of 3.0 ns , the calculated RMS values at $\psi = 1.0$ with its standard deviation error are plotted as shown in Fig. 3-8.

Table3-1: Calculated RMS of the electron cloud as a function of the photon energy for different fluctuation-related weighting values, ψ. The maximum collection time is 3 ns.

ψ	RMS (μm) 5.0 keV	RMS (μm) 8.46 keV	RMS (μm) 12.0 keV	RMS (μm) 18.0 keV	RMS (μm) 21.6 keV
0.8	7.687	8.284	8.581	9.238	9.509
0.9	8.644	9.311	9.674	10.443	10.716
1.0	9.601	10.334	10.779	11.435	11.953
1.1	10.562	11.363	11.983	12.830	13.234
1.2	11.534	12.404	13.100	13.815	14.469
--------------------------------- Statistical Output ---------------------------------					
Mean	9.605	10.339	10.823	11.598	11.976
SD	1.519	1.627	1.794	1.826	1.967
Error SD $= SD/\sqrt{5}$	0.680	0.728	0.802	0.817	0.880

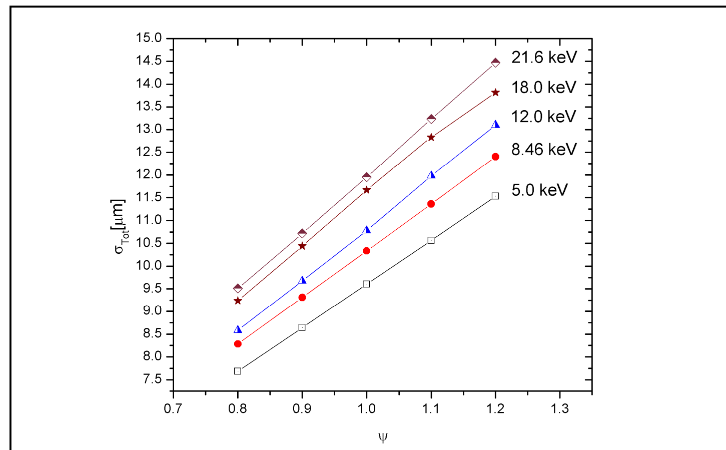

Fig.3-7: Plot of the RMS radius of the electron cloud as a function of the photon energy for different fluctuation-related weighting value ψ. The maximum collection time in the calculation is 3ns.

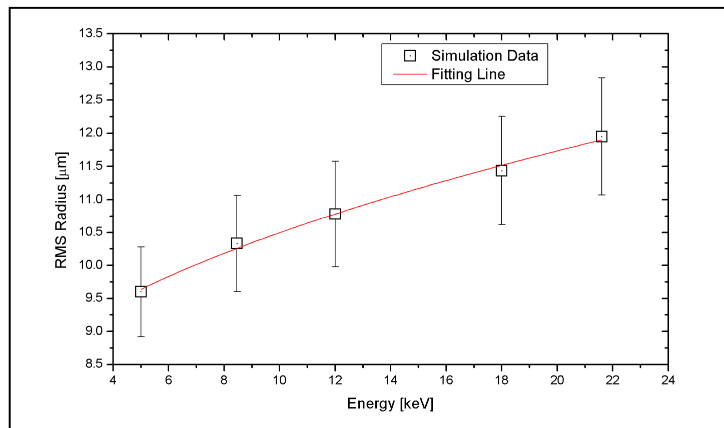

Fig.3-8: The RMS radius of the electron cloud (at ψ =1) with the corresponding photon energy and the statistical fluctuation.

F.2- Inclined Track of the Incoming X-ray Beam

The entrance of the X-ray beam with an inclined angle (θ) with respect to the line normal to the back surface will be discussed. Figure 3-9 illustrates an example of X-ray beam of 12.14 keV photon energy hitting the back surface with angle of 40° . The photons will be attenuated and absorbed along the pathway continuously. The number of absorbed photons in each slab will drop exponentially with the penetration depth for the given linear attenuation coefficient for the silicon at this energy. The number of absorbed photons as a function of the penetration depth is plotted as it is illustrated in Fig.3-3. Therefore, the number of irradiated pixels depends on the incident angle and the pixel intensity is proportional to the number of collected electrons.

The charge clouds generated at any depth will then drift parallel to the electric field lines. The pixel response and hence the total accumulated charge will manifest approximately the depth where the photons are converted. Since the pixel size is known and the detector thickness is known as well, one expects to see the charges distributed over six pixels for this inclined beam. As shown in Fig. 3-9, the pixel of the highest intensity is marked by (4) and the pixel of the lowest intensity is marked by (8).

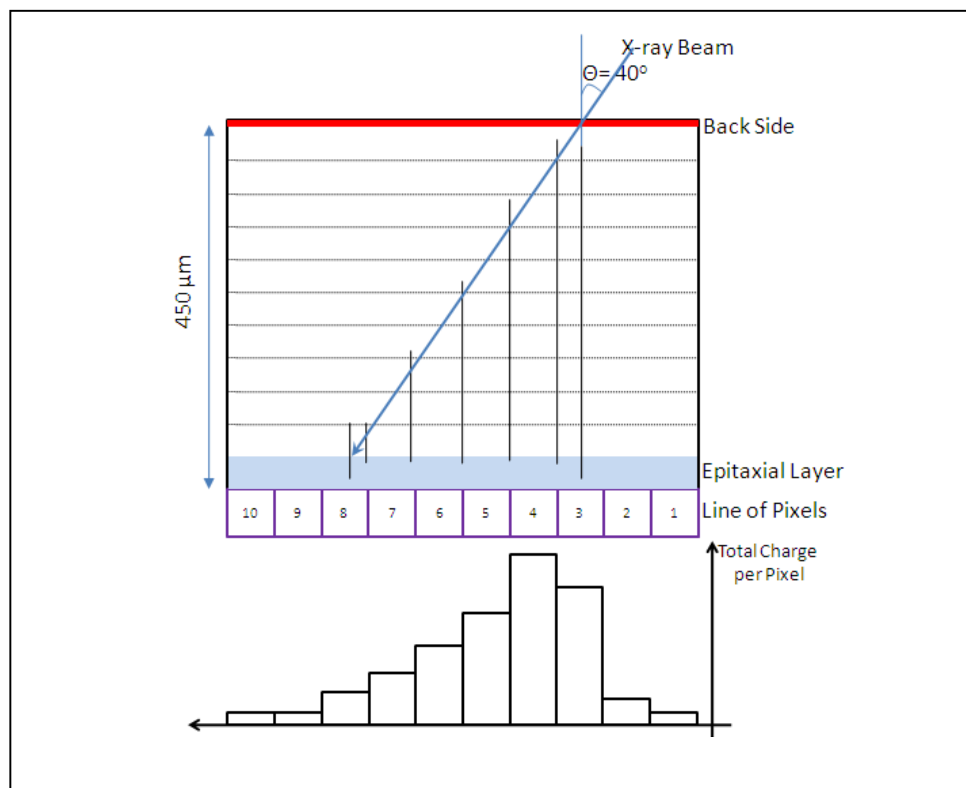

Fig.3-9: Drawing shows a 40^{0} inclined X-ray beam of 12 keV striking the back surface. The lower histogram represents the charge intensity per pixel.

The fraction of the photons attenuated between the depth Z_1 and Z_2 (with respect to the epitaxial layer) for the detector of bulk size (Z_B) is given by:

$$f(Z_2 \leq Z \leq Z_1) = e^{-\mu(Z_B-Z_1)} - e^{-\mu(Z_B-Z_2)} \quad (3\text{-}22)$$

The radial distance (w) corresponds to the difference between Z_1 and Z_2 can be calculated using the incident angle (θ)

$$w = (\tan\theta) \cdot (Z_1 - Z_2) \quad (3\text{-}23)$$

If w equals the pixel width, then the fraction of the charges collected within a given pixel $\sum_{pixel} Q$ from the total charges collected $\sum_{array} Q$ is given by:

$$\sum_{pixel} Q = \left[\sum_{array} Q\right] * \left[e^{-(\mu(E)).(Z_B-Z_1)} - e^{-(\mu(E)).(Z_B-Z_2)}\right] \quad (3\text{-}24)$$

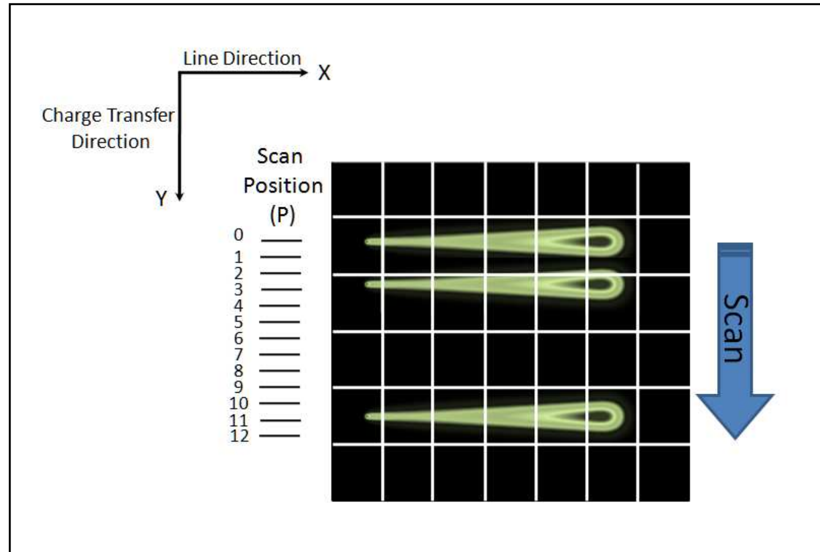

Fig.3-10: Comet-like distribution which results from the simulation of the 40^0 inclined beam of 12.14 keV photons. The RMS of the electron cloud per pixel is determined from the edge profile when the scan is carried out in the Y- axis.

In order to determine the RMS of the electron clouds as a function of the depth, a scan has to be carried out in the opposite direction of the beam projection. The scan is valid only for one dimensional projection. The result of the scan gives the edge profile per pixel and thus the RMS can be determined from the LSF.

As illustrated in Fig. 3-10, the output of the simulation model shows that the charge distribution in a fine gird is comet-like. Since the beam is projected along the x- axis, the scan has to be carried out in y-axis.

In reality, the comet-like distribution will not be seen in the detector since the pixel size is 75 times bigger than the grid cell shown in the simulation. Figure 3-11 compares the intensity images resulting from the simulation when the grid cell is 1µm and the expected image in the detector when the grid cell is 75µm.

The scan profiles in each pixel (the pixel number is related to Fig.3-9) are depicted in Fig.3-12. The following points can be concluded:

I. The relative intensity per pixel is decreasing as moving from pixel '4' to pixel '8'. Pixel '3' has less intensity than pixel '4' due to the incident angle of the beam.
II. The plateau in the scan profiles indicate that the size of charge clouds decreases as the interaction position gets closer to the epitaxial layer.
III. Since the number of the generated electrons is produced from the same photon energy and the collection time is constant at a given depth, the impact of the mutual electrostatic repulsion over the diffusion can be signified as the collection time decreases. Table 3-2 presents the RMS cloud values when the electrostatic repulsion and the diffusion are decoupled and when they are convoluted. The values in Table 3-2 are plotted in Fig.3-13 and it shows that the electrostatic repulsion is the dominant processing in the cloud expansion.
IV. Since the conversion position cannot be specified directly from the experiment, the mean collection time is calculated from the simulation model described in this section.

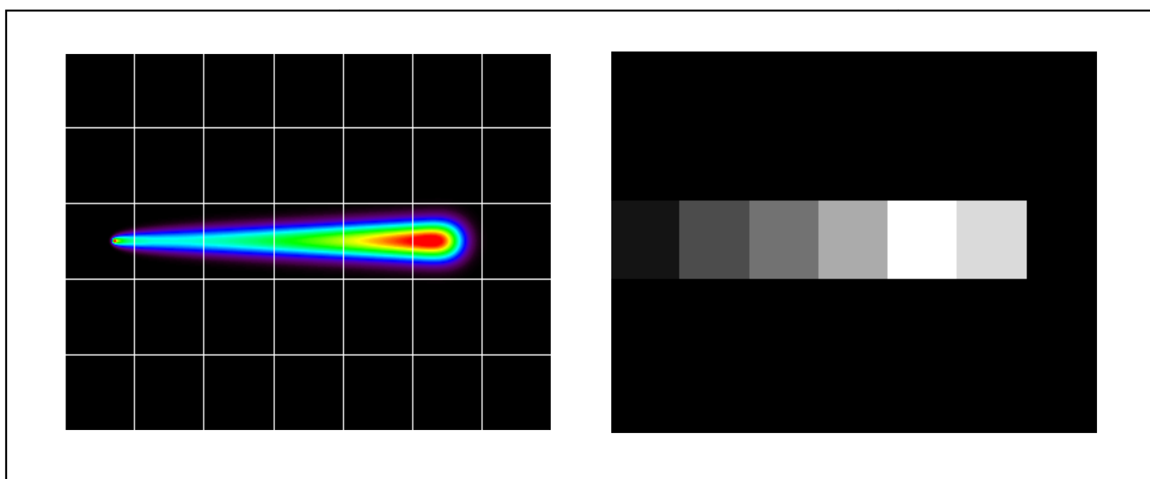

Fig.3-11: The charge distribution due to the 40° inclined X-ray track of 12.14 keV photon. The image in the left side is taken with 1µm grid cell and the image in right is the one matching the pixel size in the pnCCD detector, 75µm.

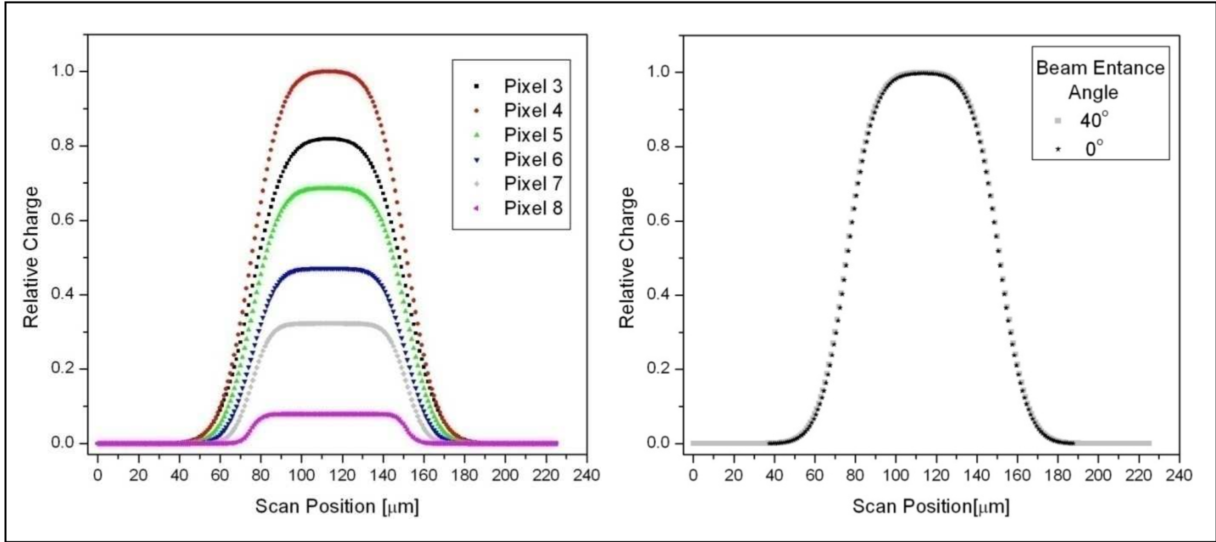

Fig.3-12: Left, simulated scan profiles per pixel result from a scan performed in a y-axis as shown in Fig.3-10. The pixel numbers is referred to Fig.3-9. Right, the scan profile when the X-ray beam is perpendicular to the surface (θ = 0) and the other scan profile is obtained from the sum of the pixel values in the x- axis (Fig.3-10) for the 40° inclined X-ray track. The x-ray energy used in the simulation is 12.14 keV.

The sum of the pixel values in the x-axis (Fig.3-10) with respect to the scan position when the X-ray track is inclined by 40° should produce the same scan profile when the scan is carried out along the y-axis with the beam hitting the detector perpendicular to its surface, as shown in Fig. 3-12 right. This implies that the PSF which results from the beam perpendicular to the surface is the convolution of the PSFs which are distributed over the pixel due to the inclined X-ray track.

Table 3-2: The RMS of the electron cloud due to the diffusion process only, mutual repulsion only, and the convolution of both of them. The photon energy is 12.14 keV.

Pixel Index	Collection Time [ns]	RMS [µm] Diffusion	RMS [µm] Repulsion	RMS[µm] Diffusion ⊗ Repulsion
8	0.292	1.876	5.057	5.316
7	0.916	3.317	7.394	7.944
6	1.372	4.060	8.460	9.177
5	1.839	4.700	9.328	10.197
4	2.303	5.260	10.055	11.063
3	2.769	5.766	10.69	11.827

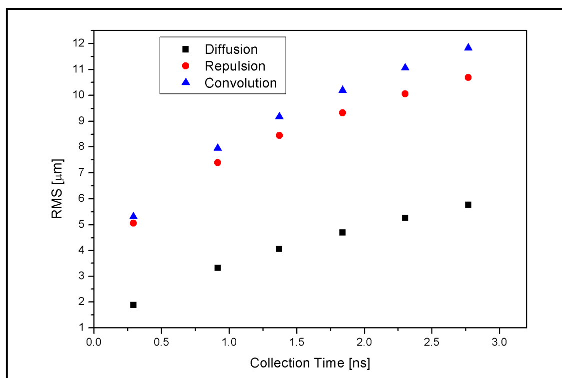

Fig.3-13: Plot for the RMS values presented in Table 3-2 against the collection time.

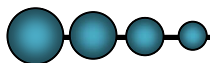

4. Experimental Set-up and Data Handling

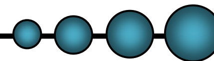

This chapter describes the experimental setup and the alignment which was made to perform the experiments. The procedure to correct the measured data is explained as well.

A. The Objective of the Experiment

The image formed by the pnCCD detector is a consequence of the detection of the electron clouds generated from the interaction of the X-ray photons. Being a 2D array detector, the pattern formation depends essentially on the size of the charge cloud, landing position. The size of the charge cloud can be determined by making a scan through the pixel edges to obtain the edge profile. The landing position is directly related to the conversion position of the photon. The purpose of the experiment is to measure the electron cloud size as a function of phonon energy using a monochromatic X-ray beam.

B. The Experimental Technique

The experimental setup includes a circular pinhole collimator, monochromator, stepping motors, flying tube and software interface.

The measurements were performed using the synchrotron radiation at the EDR beamline in BESSY II. The energy range of the white beam is $5\,keV\ < E\ < 30\,keV$ having a maximum photon flux ($2.9 * 10^5 photons/s/mA$) at 7.7 keV as depicted in Fig. 4-1. The white spectrum shows a critical energy at approximately 1 keV and strong air absorption for the low X-ray energies up to roughly 5 keV. An exponential decay in the intensity appears for the energies higher than the 7.7 keV [ref. 28,29].

A beam of a monoenergetic X-ray is obtained by using a monochromator made of silicon [111]. The monochromator interrupts the direction of the synchrotron beam and according to the glancing angle (θ) between the direction on the beam and the monochromator, the reflected beam will have definite energy (E_{refl}) and direction.

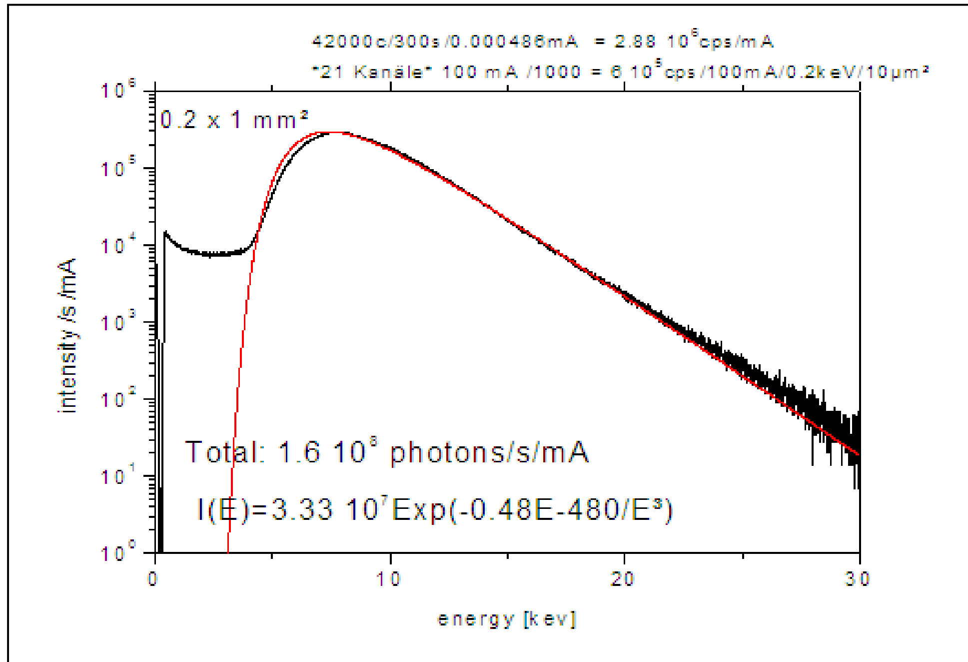

Fig.4-1: The x-ray spectrum of the white synchrotron radiation of beam size of 0.2 x 1mm measured through an air pass of about 1m [ref. 29].

The relation between the glancing angle θ and the reflected wavelength λ is give by the Bragg's law:

$$n \cdot \lambda = 2d sin\theta \qquad n = 1,2,3, \ldots \tag{4-1}$$

where n the harmonic order. The crystal lattice spacing (a) of the monochromator is $a = 5.43$Å.

For example, the first order reflection (n=1) of 5 keV can be obtained if the monochromator is tilted with angle of 46.4º with respect to the direction parallel to the beam:

$$E_{refl} = \frac{12.4\ keV.\text{Å}}{\sin{(23.3)}} * \frac{\sqrt{3}}{2 * 5.43\ \text{Å}} = 5\ keV$$

Due to the crystal symmetry the second order reflection (n=2) is a "forbidden" reflection. The first harmonic X-ray reflection is considered in the data analysis. The energies used are 5, 8.46, 12.14,18 and 21.6 keV. Evacuated flying tube was used for the 5keV energy in order to reduce the air scattering. At a distance of 70cm to 100 cm from the monochromator, a circular pinhole collimator is aligned parallel to the detector surface. Figure 4-2 illustrates the experimental setup.

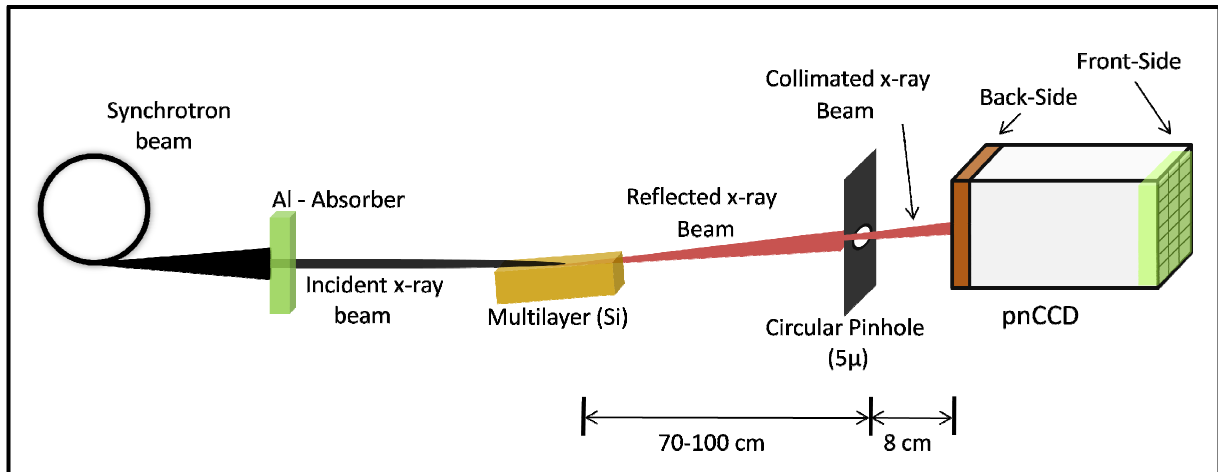

Fig.4-2: Drawing illustrates the experimental setup.

The pinhole collimator used in the experiment is $5\mu m$ in diameter drilled in a lead sheet of 1.8 mm thickness and covered on front and back sides with 5.2 mm Aluminum.

The collimator transmits the reflected X-ray through the aperture and attenuates their passage elsewhere. The pinhole is located at a distance of $10\ cm$ from the detector surface. Therefore, the illuminated area in the detector is thus magnified with a diameter (D) of:

$$D = \frac{m+l}{m} * 2d \tag{4-2}$$

Where m is the source-pinhole distance, l is the pinhole-detector distance and d is the radius of the pinhole.

The detector can be moved in two dimensions, via vertical and horizontal scanning motors. Other stepping motors are used to align the pinhole collimator, Fig.4-3(left).

The scan has been performed by moving the detector either vertically or horizontally while the pinhole position was fixed. The vertical direction is the charge transfer direction in the detector (Y-axis), and the scan in the horizontal direction is for the line direction (X-axis). The sequence of the scan and the alignment is controlled externally. The scan was carried out in 5 µm steps running over a number of pixels.

The starting point of the scan is the center of the pixel. It is experimentally found by the maximum possible accumulated intensity in this pixel compared with the neighboring pixels. The “online” software is a tool offering an interactive visualization of the intensity image as well as spectral display for the detected energies.

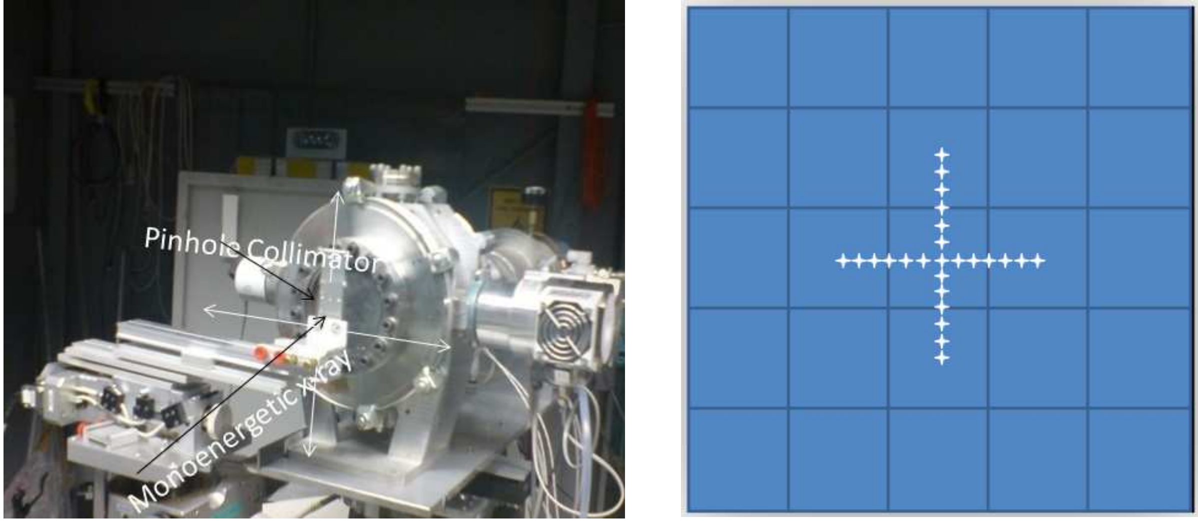

Fig.4-3: The Pinhole collimator aligned in front of the detector (left), imaginary steps of the scan in x-axis and y-axis(right)

C. The Edge Profiles

The defined pixel's sizes will be the "micrometer scale" used to study the position resolution and to quantify the size of the charge cloud when the scan crosses the pixel's boarders. The physical structure and size of the pixel will be manifested in the measurement outputs.

At each scan position, a sufficient number of photons was accumulated to deduce the position resolution at the location. Consequently, the statistical fluctuations can be spatially minimized and the position resolution can be improved. Assuming that the pixel P_i is the targeted pixel of the scan , then the pinhole has to be centered in and perpendicularly aligned to the center of the pixel (P_{i-1}) and the scan stepped in a definite width (Δx) , until the center of pixel (P_i) is reached. The y- direction is constant since the scan is carried in one direction, the x-direction.

$$Scan\ steps(x_n): x_{init}, x_{init} + \Delta x, \dots \dots, x_{edge}, \dots \dots\ x_{final}$$

The charge accumulated in pixel P_i with respect to the scan position, $C_{total}^{P_i}(x_n, y)$, will increase monotonically as the scan progresses toward the edge of pixel P_i and reach the maximum possible when the total charge cloud is collected in the center of the pixel P_i. At the end of the scan, a one-dimensional edge profile is obtained which compromises the relative charges accumulated per scan position in the pixel P_i versus the scan position. The relative charge in the pixel P_i varies as follows:

$C_{total}(P_i(x_n, y))$	≈ 0	No Charges is accumulated in pixel (P_i)
$C_{total}(P_i(x_n, y))$	≈ 1	Maximum Charge is accumulated in pixel (P_i)
$1 < C_{total}(P_i(x_n, y)) < 0$		Partial charges accumulation in pixel (P_i)

D. Data Handling and Correction Procedure

Two software packages are available in order to handle the data and perform all required correction, evaluation and display for the raw data. Figure 4-4 shows block diagram of the correction procedure executed by the software. The "On-line" software is a "Graphic User Interface" tool which facilitates an interactive communication with the detector during the X-ray detection. In this software the image is displayed in a matrix of 256x256 pixels, having the intensity or energy information per pixel. Moreover the energy spectrum of the detected photons can be also displayed. The correction routines are accessible and can be applied directly on the displayed image and on the energy spectrum. Any geometrical setup for the experiments can be built up and aligned in consistent with the online display. The raw data are written in a binary frame format file for later use. The written frames data (the header plus the pixel info) is read and corrected using the so-called "Offline software" written in IDL language. The main correction routines included in the software packages are the offset, noise, common mode, gain and CTE,[ref. 14].

D-1 Offset and Noise Maps

Dark frames are acquired when the detector is under operation and is not exposed to any X-ray beam. The algorithm can be explained in the following steps to generate the offset map:
For each pixel in the given frame:

1. Add the values over the whole dark frame (S_{total})
2. Sort the data from the minimum to the maximum value.
3. Subtract the two lowest (S_{min}) and two largest (S_{max}) values from the summed value.
4. Find the mean value $\bar{S} = \frac{S_{total} - S_{min} - S_{max}}{N_{frames} - 4}$

The process will then end with a new matrix called the offset map as shown in figure (4-5). It contains the calculated offset values. Step 3 is needed because the detector is sensitive to the cosmic rays or any radiations scattered to the detector during writing the dark frames.

For more detailed offset map, a fine structured matrix, called *residual offset map*, can be obtained by calculating the median value per column and simultaneously the median value for each raw. The residual offset map is generated by subtracting the pixel values in the offset map from the median values. Any recognized white pixel can indicate that the leakage current is high in this pixel.

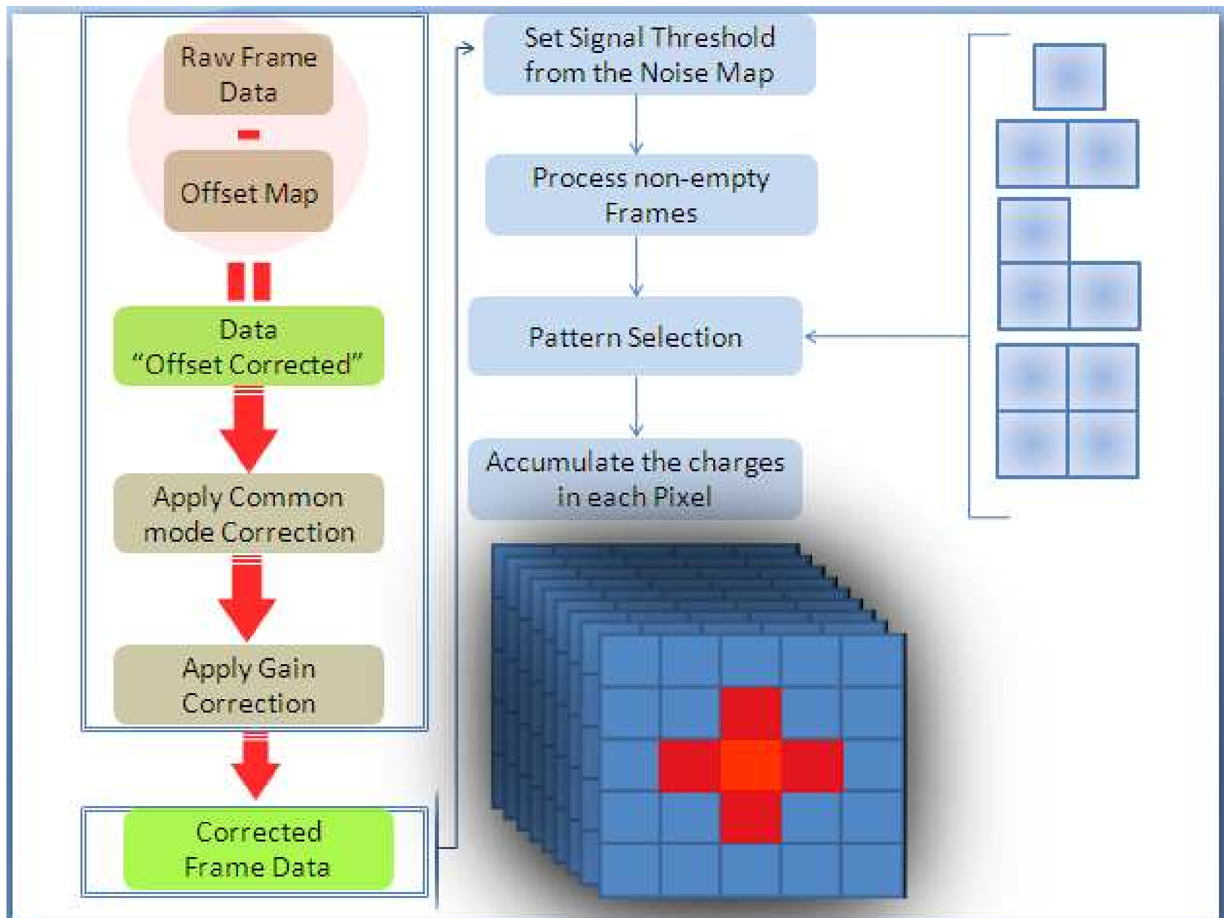

Fig.4-4: Block diagram for the Data correction procedure for each frame data in both online and offline software.

D-2 Noise Map

The Noise map Fig. (4-5) is created by calculating the standard deviation in each pixel as shown in the following steps:

In each dark frame:

1. Calculate the median value per raw
2. Subtract the median from each pixel in the raw

3. Generate the offset map
4. Subtract twice the pixel offset.

For each pixel in the dark frames:

5. Sum up the value in the pixel in all dark frames, find out the mean value ($\bar{V}$).
6. Subtract the pixel value (V_{pixel}) from the mean and square the result.
7. Find the variance by dividing step 5 by the number of dark frames ($N_{dframes}$).
8. The noise is therefore the standard deviation calculated by the square root of step 6.

$$\sigma_{noise} = \sqrt{\frac{1}{N_{dframes}} * \sum_{1}^{N_{dframes}} (V_{pixel} - \bar{V})^2} \quad (4\text{-}4)$$

Step 1 is needed for the common mode noise correction in step 2.

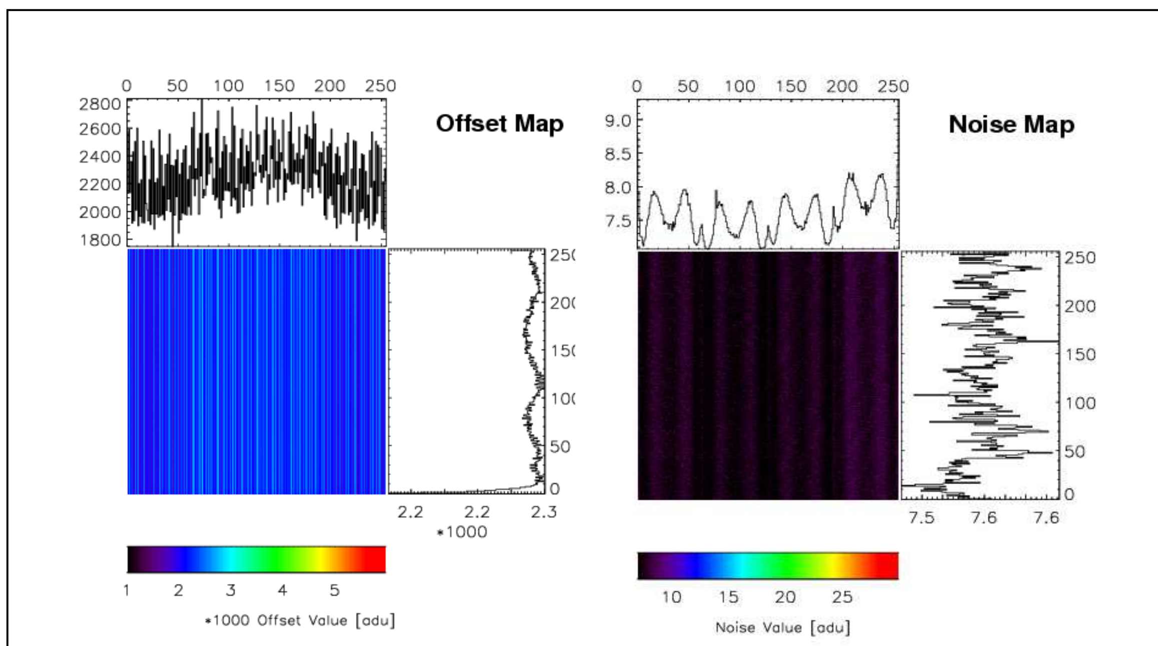

Fig.4-5: The offset map and the noise map resulting from the dark frames. The temperature of the detector is constant and is eaual to -80.

D-3 Common Mode Noise

The standard approach to correct for the common mode noise, either for the dark frames or signal frames, is to take the median value for each raw and to correct for it.

In each Frame:

1. Subtract the offset value in each pixel (V_{offset})
2. Calculate the median value in each raw (V_{median})
3. Subtract the median value from the pixel value.

$$V_{pixel}^{corr} = V_{pixel} - V_{offset} - V_{median} \tag{4-5}$$

D-4 Gain and Charge Transfer Inefficiency (CTI)

For the charges being read out from different channels, amplified and then converted via the ADC, the output values are slightly different and need to be corrected. The output values are read in the analog to digital unit (ADU). The pre-requirement to perform this correction is to record a mono-energetic X-ray peak in a way that enough counts are detected in each pixel and uniformly distributed over the whole image area or over the region of interest (ROI). If the data in the matrix is correct by the offset and the common mode, the signal threshold ($4\sigma_{noise}$) can be applied hereafter and the split pattern can be selected. The patterns of interest here are single events and only column-wise split events. If the mean value of those events in each channel ($E_{channel}$) is calculated (usually from the Gaussian fit), the overall mean energy ($\bar{E}$) for all channels (N_c) can be determined such that:

$$\bar{E}\ (ADU) = \frac{1}{N_c} * \sum_{1}^{N_c} E_{channel} \tag{4-6}$$

The ratio of $\bar{E}/E_{channel}$ can be used as a correction factor for each given channel in a way that all channels will have the same peak centroid in the energy spectrum. The conversion factor ($cfactor$) from ADU to eV can be then known if the mono-energetic X-ray peak centroid ($\bar{E}(eV)$) is known

$$cfactor = \frac{\bar{E}(eV)}{\bar{E}(ADU)} \tag{4-7}$$

For evaluating the CTE, the single events and the joined column-wise split events are used. The line of least-squares can be fitted to the data and the peak position (P) shifts along the rows (r) according to:

$$P(r) = P_o.CTE^r \tag{4-8}$$

The CTE in the *pn*CCD detector is 0.999985 and the CTI is 0.000015.

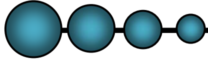

5. Measurements and Results

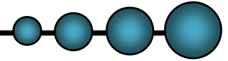

The analysis of the measured data is presented in this chapter. The correction method described in the previous chapter is used to correct the row data.

A region of interest (ROI) of 3x3 pixels is considered in the analysis to determine the photon energy which has to be included in the data analysis. If the sum of the pixel charges in the ROI falls within the upper and lower energy limits of the photopeak, then the charges are added up in their pixels over all the measured frames.

The relative charge in the target pixel is obtained from the ratio of the accumulated charges in this pixel relative to the total charges in the ROI for each scan position. The target pixel is known since the detector was moved in specific steps from a known initial position.

The scan profile is the two edge profiles which result from crossing the transition scan the pixel edges in one direction. The differentiation of the edge profile provides the line spread function. The RMS radius of the charge cloud (σ) is the standard deviation of the LSF which is determined by applying Gaussian fit or a proper fit to the LSF.

Two measurements were performed using selected photon energies from the synchrotron radiation. The measurements depend on the angle of incidence of the collimated X-ray beam relative to the detector surface.

The angle-based measurement investigates the charge cloud size as a function of depth. The measurement is achieved by tilting the detector horizontally (line direction in the detector) with a specific angle with respect to the incoming X-ray beam. X-ray track of 30° and 40° respectively were obtained.

The inclined track causes the generated electron clouds to spread over a number of pixels. By performing the scan in the charge transfer direction, the RMS radius of the charge cloud per pixel can be obtained. The mean collection time which corresponds to the RMS value can be calculated from the simulation model (section F2 of chapter 3) since the conversion position of the photon cannot be specified experimentally.

By applying a proper fit to the measured RMS values, the contribution of the diffusion and the electrostatic repulsion in the cloud expansion can be determined.

The energy-based measurements aim to find the RMS of the electron cloud as a function of the X-ray energy. The experiments were performed with a collimated X-ray falling normal to the detector surface. Therefore, the point spread function is the weighted sum of all charge clouds generated along the 'normal' X-ray track in the detector volume. Horizontal and vertical scans were performed separately to obtain the edge profile along the line direction and the charge transfer direction respectively.

A. X-ray Spectra and Energy Resolution

The pnCCD can be used to detect the X-ray spectrum of the incoming photons. The monochromatic X-rays are obtained in the measurements from the silicon monochromator placed in the X-ray pathway as shown in Fig 4-2.

In the pixel array, the electron cloud of the impinging photon is registered in one pixel or a number of neighboring pixels. The corrected signal frame is primarily compared with a signal threshold. The signal threshold is four times the noise map. A moving mask of 4x4 pixels is thereafter applied on the corrected frames in order to determine the accepted/rejected patterns of the charge spread. The sum of the pixels in the accepted patterns are joined and added to the energy spectrum. The accepted pattern is shown in Fig.2-2.

Figure 5-1 shows the measured energy spectra. The energy peaks which are involved in the analysis of the following sections are 5.0, 8.46, 12.14, 18.0 and 21.6 keV. They are the first harmonic peaks resulting from a 111 reflection from the monochromator. The other peaks result from either a higher harmonic peaks mixed with a pile up events or only pile up peaks due to a forbidden reflections from the monochromator.

The experiment for measuring the 5 keV photons (spectrum A) includes using an evacuated flying tube between the monochromator and the pinhole since the air scattering attenuates the 5 keV photons reaching the detector. The first peak in this spectrum is the first harmonic reflection and the other peaks are either 'isolated' energies or mixed with the pile-up events.

The photopeak at 15 keV is strong reflection since the detector was close to the monochromator (~70 cm) and the photons experience less scattering in the air at this energy. The energy peak at 20 keV is the fourth-order reflection and may also include some pile-up events. The quantum efficiency for the detector at 30 keV is roughly 0.11, therefore this peak is the photons of the sixth harmonic with probably greater contribution of the pile up photons coming from the strong reflection at 15 keV.

The energy resolution of the detector depends mainly on the number of generated electrons and the electronic noise. The measured energy resolution for the photopeaks of the first harmonic is the FWHM resulting from the Gaussian fit applied on the peak. Table 5-1 shows the measured and the calculated values. The theoretical values are calculated using eq. 3-4 by assuming 3.7 eV for the pair ionization energy, $2e^-$ for the ENC and 0.118 for the Fano factor. The deviation between the measured values and the calculated one is due to the fact the electron cloud is shared between a numbers of neighboring pixels and the noise per cluster increases with square root of the number of pixels involved (Eq. 2-3).

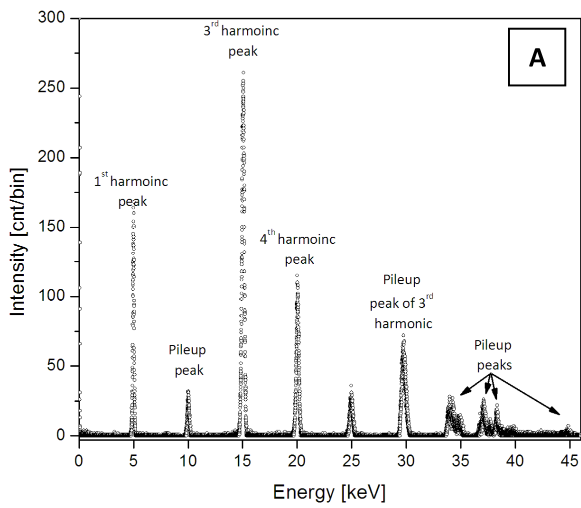

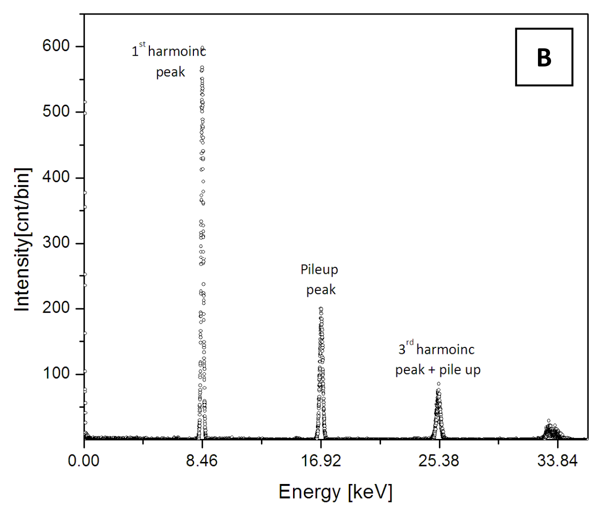

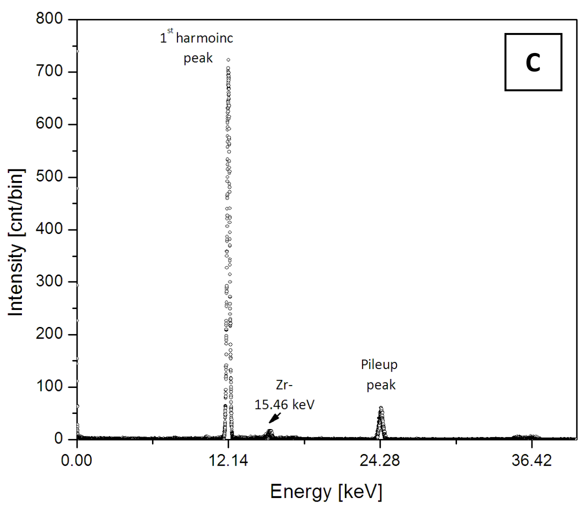

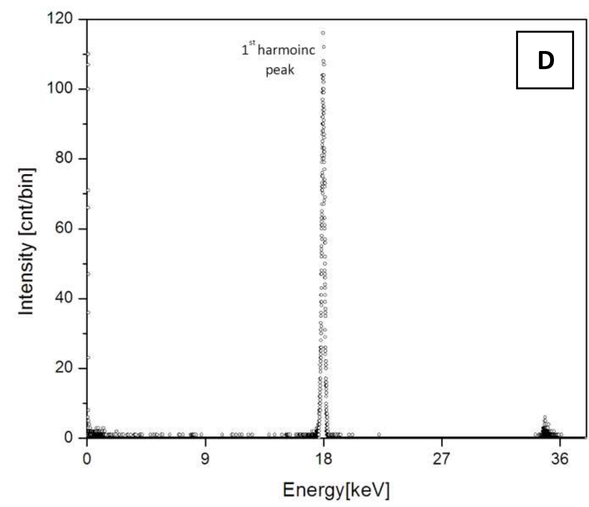

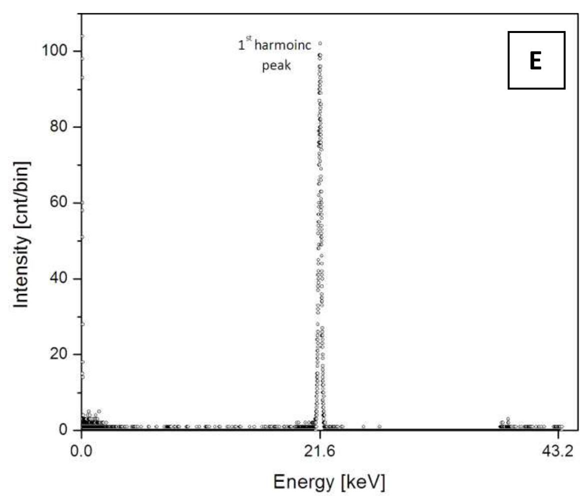

Fig.5-1: The measured X-ray Spectra reflected from the silicon monochromator. The spectra are from a pixel matrix of 5 x 5 around the target pixel. The first harmonic peak in each spectrum is considered in the analysis due to the fact that they do not include pile up photons. The zirconium energy is due to the filter introduced between the X-ray source and the monochromator

Table.5-1: The measured energy resolution versus the theoretical value

Peak Position (keV)	Measured Energy Resolution FWHM (eV)	Calculated Energy Resolution FWHM (eV)
5.00	147	113
8.46	180	146
12.14	244	173
18.00	267	210
21.60	284	232

Figure 5-2 shows a plot of the RMS energy resolution (FWHM/2.35) versus the photon energy. The best fit to the data is derived from equation 3-4 as follows:

$$\frac{FWHM}{2.356} = \sqrt{F * w * E + [w * ENC]^2}$$

Taking $\alpha_1 = F * w$ and $\alpha_2 = [w * ENC]^2$, the equation above becomes:

$$\sigma_E = \sqrt{\alpha_1 E + \alpha_2}$$

The fitting curve gives: $\bar{\alpha}_1 = 0.6856\ eV$ and $\bar{\alpha}_2 = 617.77\ eV^2$

For example, the energy resolution of the detector for impinging photons of 15 keV is

$$\sigma_E = \sqrt{0.6856\ eV * 15000\ eV + 617.77\ eV^2} = 104.41\ eV$$

$$FWHM = 2.356 * \sigma_E = 2.356 * 104.14\ eV = 245.35\ eV$$

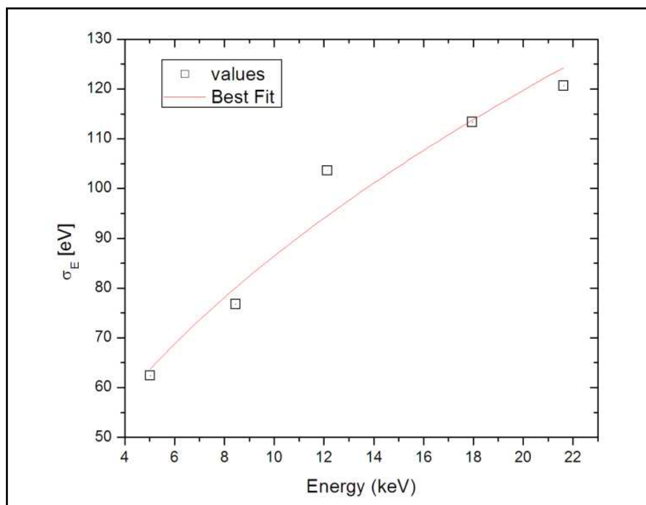

Fig.5-2: The RMS energy resolution versus the photon energy and the best fitting line.

The energy resolution for the detector at 12.14 keV shows a deviation from the measured values. The pressure inside the evacuated chamber of the detector was dropped to a value of $4.3 * 10^{-3} mbar$ in this measurements compared to $3.9 * 10^{-7} mbar$ in the other measurements. The drop in the pressure along with the constant cooling supply of $-80\ °C$ for the detector makes an ice layer to build up on the detector surfaces. This consequently causes paralyzation to the voltage supply circuit in the back surface resulting in drop of the depletion voltage from -230 V to roughly -130 V [ref. 12].

Nevertheless, the detector is still fully depleted and sensitive to the X-ray since -90 V is the minimum depletion voltage required in this detector. The drop in the depletion voltage will consequently reduces the electric field force and therefore the electron clouds require more time to reach the potential minima.

B. Inclined X-ray Beam Track

This measurement was performed using X-ray energy of 12.14 keV, Fig. 5-1 (C). The detector is placed on a table such that the detector can be manually rotated in the XZ plane. The X-axis refers to the "line direction" of the detector array and Z-axis is the direction going through the detector volume and normal to the detector surface. Therefore the following points shall be considered whenever mentioned in this section:

[1] the inclined angle (θ) of the X-ray track is measured reference to the Z-axis. This was achieved by aligning primarily the pinhole collimator and the detector parallel to each other and then by rotating the detector by a specific angle. Due to the geometrical limitations in the experimental setup, a maximum angle of 40° was reached. The limitations include the size of the entrance window of the detector chamber, the distance between the window and the detector chip, the distance between pinhole collimator and the window and the presence of the copper plate which shields the frame store area.

[2] the charge clouds are projected into the "line direction" in the pixel array. The numbers of the projected pixels therefore differ according to the angle.

[3] the scan was performed in the "charge transfer direction" which is the direction parallel to Y-axis of the pixel array.

Three measurements were performed for the same photon energy by changing the incident angle. The angles are 0°, 30° and 40°. The measurement at angle 0° defines the *reference pixel* of the charge distribution for the other angles, since the "center-of-mass" for the all charge clouds will be in this pixel.

Regardless which track the X-ray has; the electron clouds will drift parallel to the direction of the electric field lines. For a given linear attenuation coefficient in silicon at 12.14 keV, the total number of absorbed photons will exponentially decrease as seen in figure 3-3. This attenuation will occur along the whole detector volume from the back side to the epitaxial layer (Fig.3-3).

The involuntary drop in the depletion voltage in this measurement increases the collection time to ~5.8 ns compared to ~3.0 ns when the electron cloud drift the whole detector thickness. Consequently, the electron clouds will experience more expansion during this collection time.

B-1 Measurement with 40° Inclined X-ray Beam

The intensity images shown in figure 5-3 illustrate the charge distribution of the projected 40° X-ray beam. Image (A) is the simulation output taking with image array of $1\mu m$ cell size with the color scale presents the charge accumulation level in each cell, red color maximum value. Image (B) is the measurement output as seen in the pnCCD array of $75\mu m$ pixel size and image (C) is the surface plot of image (B). As depicted, the charges are shared mainly between six pixels starting from right to left. The first bright pixel (Pixel 1) in right hand side is the *reference pixel*. The successive pixels will be numerated from 2 to 6 with respect to "Pixel 1".

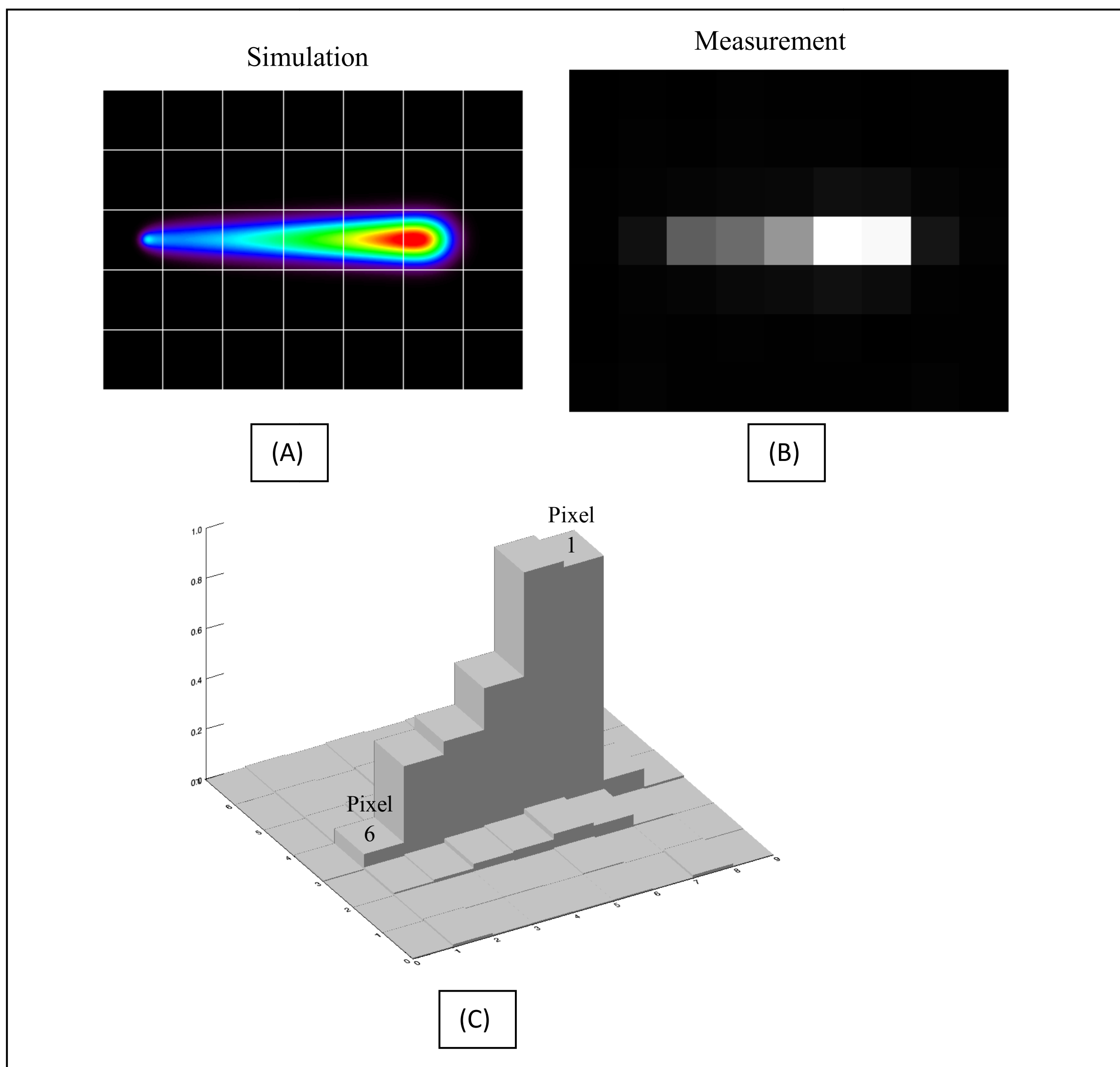

Fig.5-3: Images of the 40°inclined x-ray beam. (A) Simulation output seen by 1μm cell size. (B) The charge distribution measured with the pnCCD. (C) The normalized surface plot of image (B)

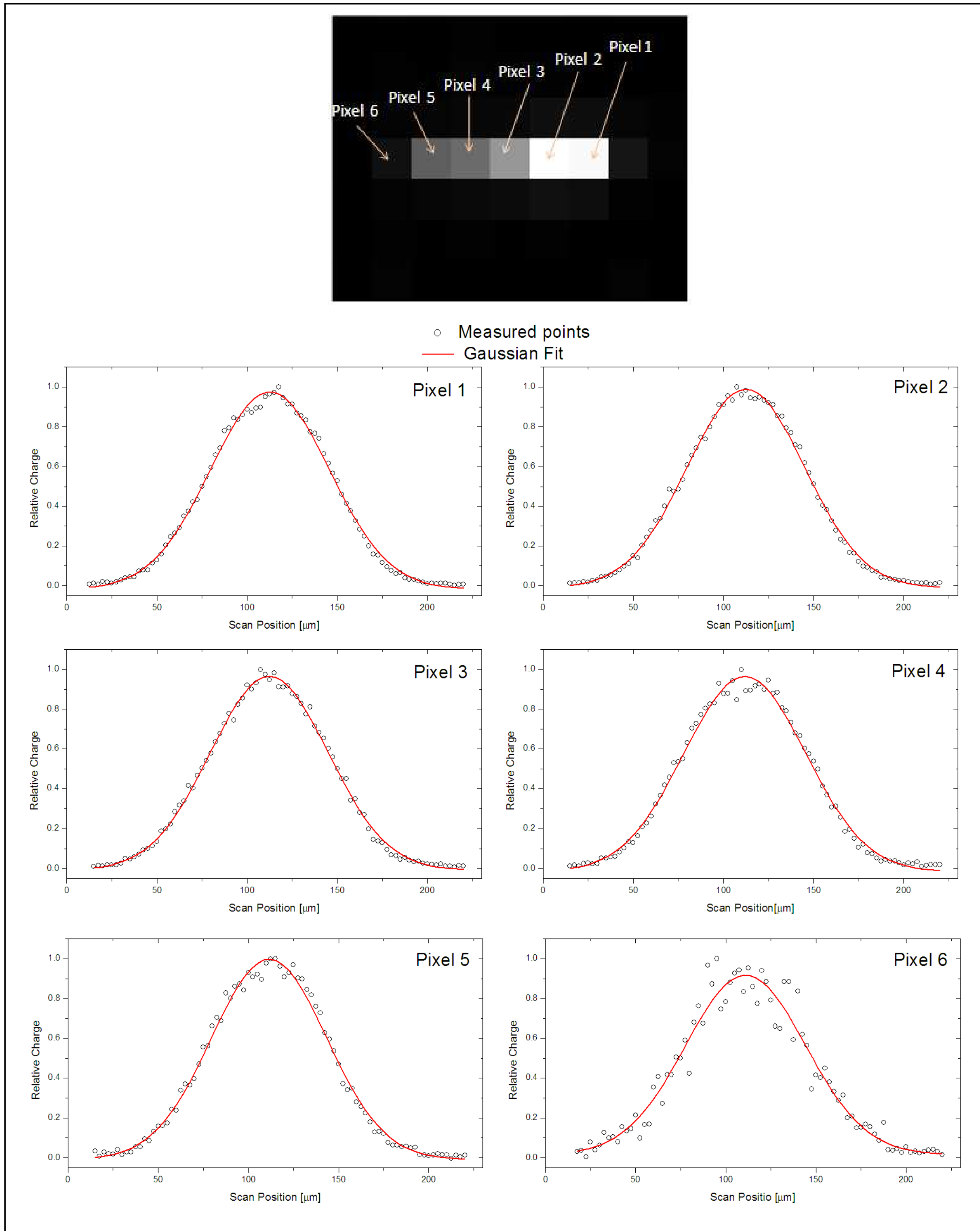

Fig.5-4: Measured scan profiles for the projected pixels from 40° X-ray track. Each profile is normalized to its maximum value and Gaussian fit is applied on it. The applied back voltage of the pnCCD is roughly -125V.

The scan was performed with 2.5 μm per step in this measurement. The normalized scan profile for each pixel is depicted in Fig. 5-4. The measured scan profiles can be fitted with Gaussian function as shown. The statistical fluctuation in the measured value per scan position equals the square root of the number of electrons detected per pixel position. It is dependent, on the other hand, on the landing position and thus the ratio of charge sharing between the pixels in the ROI. Therefore, the sensitivity (the number of electrons per unit time per pixel) is dependent on the angle of incidence. Comparing *Pixel 1* with *Pixel 6* shows that the fluctuations in the measured values in *Pixel 6* are higher than *Pixel 1*which means that the number of electrons detected in *Pixel 6* is less than the number of electrons detected in *Pixel 1*.

In order to determine the radius of the charge cloud corresponding to the scan profiles in theses pixels, a sigmoidal fit is applied on the edge profile and then differentiated. The RMS radius is the standard deviation of the Gaussian fit applied on the differentiated sigmoid. The method which is used to determine the radius of the charge cloud is illustrated in Fig.5-5.

Table 5-2 shows the radii of the charge clouds in each pixel resulting from the differentiated edge profiles.

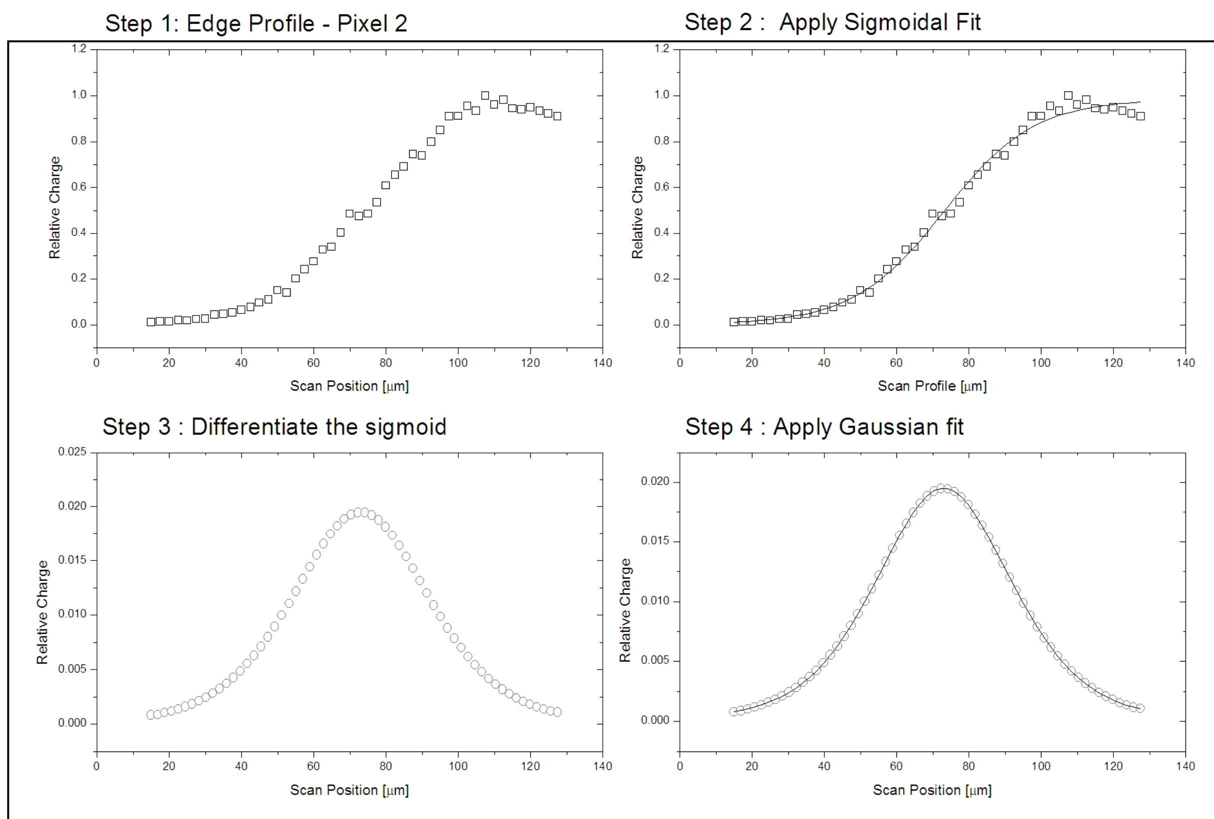

Fig.5-5: The procedure which is used to determine the RMS radius of the charge cloud in each pixel.

Table 5-2: The measured and the calculated RMS radius in each pixel from the 40° X-ray track projection.

Pixel No.	Measurement		Calculation	
	RMS Radius $[\mu m]$	Error $[\mu m]$	Collection Time [ns]	RMS Radius $[\mu m]$
1	18.589	0.183	9.371	17.597
2	18.118	0.187	8.842	17.259
3	17.815	0.187	8.425	17.073
4	17.099	0.224	7.511	16.903
5	16.501	0.205	6.893	16.180
6	16.045	0.211	6.361	14.092

The error in sigma results from the error of the standard deviation of the Gaussian fit. The corresponding time in Table 5-2 is calculated from the numerical model in section F.2 of chapter 3. The plot of the theoretical values of sigma versus the collection time is depicted in Fig. 5-6 A.

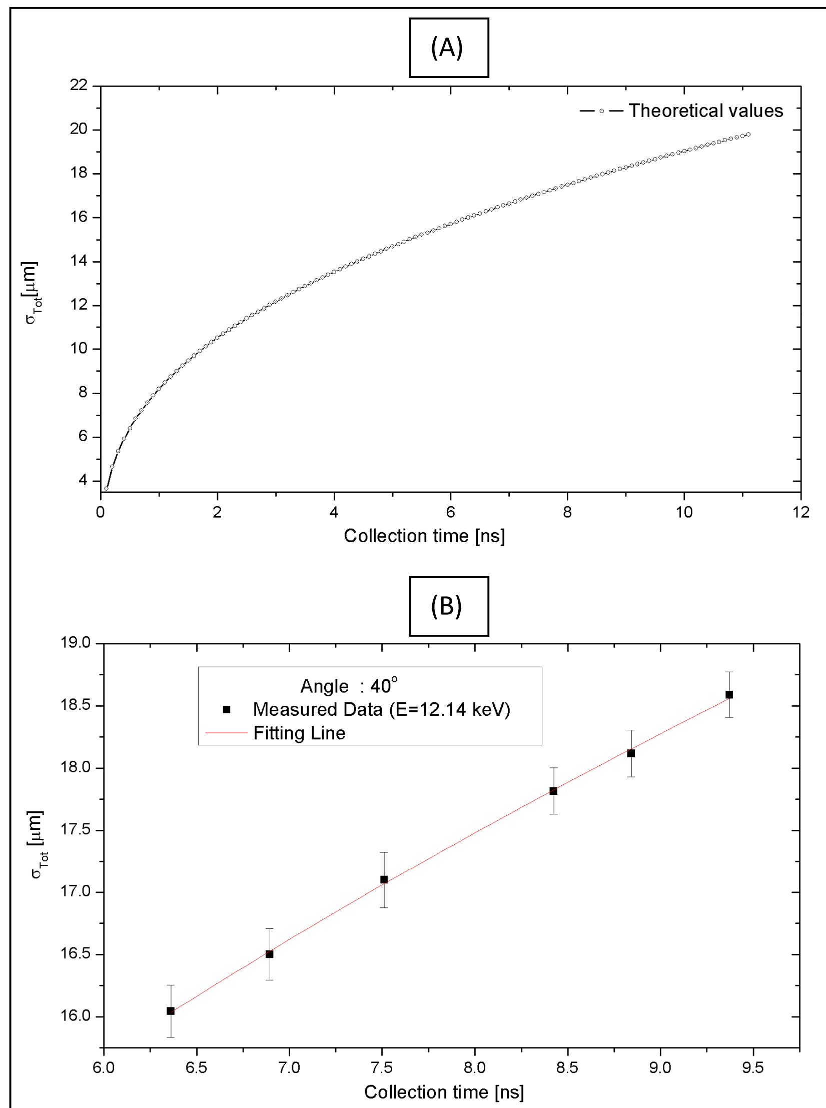

Fig.5-6: Graph (A) presents the theoretical curve which is used to calculate the corresponding time for the measured sigma. Graph (B) is the measured radius of the charge cloud per pixel versus the calculated collection time.

The measured RMS radius in each pixel with the corresponding calculated collection time is plotted in Fig. 5-6 (B). The best fitting line is shown as well in the same figure. As shown in chapter 3, at good approximation, the quadratic sum for the values of the contributions can be used. This allows the separation of the effects. The fitting line thus relates the final cloud size (σ_{Tot}) with the collection time (t) by taking the RMS of the contributions, the diffusion (σ_D) and the mutual repulsion (σ_R), as follows:

$$\sigma_{Tot}(t) = \sqrt{\sigma_D^2(t) + \sigma_R^2(t)} \tag{5-1}$$

Substituting Eq. 3-17 and Eq. 3.20 in Eq. 5-1 gives

$$\sigma_{Tot}(t) = \sqrt{\left(2\frac{kT}{Q} * \mu_e * t\right) + \left(\frac{3\mu_e Q}{4\pi\varepsilon} * N_e * t\right)^{2/3}} \tag{5-2}$$

Introducing fitting parameters P_1 and P_2 in the previous equation gives the fitting equation:

$$\sigma_{Tot}(t) = \sqrt{(P_1 * t) + (P_2 * t^{2/3})} \tag{5-3}$$

where $P_1 = a * 2\frac{kT}{Q} * \mu_e$ and $P_2 = \left(b * \frac{3\mu_e Q}{4\pi\varepsilon} * N_e\right)^{2/3}$. ‘a’ and ‘b’ are introduced as a proportionality factors.

The collection time in Eq. 5-3 is always greater than zero since the expansion of the charge cloud is started from an initial point-like size.

The fitting parameters P_1 and P_2 for the fitting line in 5-6(B) are:

$$\overline{P_1} = 10.196 \left[\frac{\mu m^2}{ns}\right] \quad and \quad \overline{P_2} = 55.995 \left[\frac{\mu m^2}{ns^{2/3}}\right]$$

The error in $\overline{P_1}$ is 1.257 $\mu m^2/ns$ and in $\overline{P_2}$ is 2.513$\mu m^2/ns^{2/3}$.

The best fitting line is then given by:

$$\boxed{\sigma_{Tot}(t) = \sqrt{10.196 \left[\frac{\mu m^2}{ns}\right] * t + 55.995 \left[\frac{\mu m^2}{ns^{2/3}}\right] * t^{2/3}}} \tag{5-4}$$

For example, the radius of the charge cloud for 8.0 ns collection time is:

$$\sigma_{Tot}(t = 8.0\ ns) = \sqrt{\left(10.196\frac{\mu m^2}{ns} * 8.0\ ns\right) + \left(55.995\frac{\mu m^2}{ns^{\frac{2}{3}}} * [8.0\ ns]^{\frac{2}{3}}\right)}$$

$$\sigma_{Tot} = \sqrt{81.568\ \mu m^2 + 223.8\ \mu m^2} = 17.475\ \mu m$$

Table 5-3: The decoupled values of the diffusion and mutual repulsion contributed in the radius of the charge cloud calculated from the first and second terms in equation 5-4 for the photon energy of 12.14keV.

Calculated Collection Time [ns]	Measurement			Calculation
	σ_D [µm]	σ_R [µm]	$\sigma_{R/}\ \sigma_D$	$\sigma_{R/}\ \sigma_D$
9.371	9.775	15.776	1.614	1.513
8.842	9.495	15.474	1.630	1.528
8.425	9.268	15.226	1.643	1.539
7.511	8.751	14.655	1.675	1.570
6.893	8.383	14.241	1.699	1.593
6.361	8.053	13.865	1.722	1.614

The fitting formula (5-4) is valid to calculate the radius of the charge cloud at a given collection time whenever the mutual repulsion is the dominant process over the diffusion ($P_2 > P_1$). The contribution of the mutual repulsion and the diffusion in the measured radius of the charge cloud can be extracted from Eq. 5-4 as shown in Table 5-3. The ratio between the two terms ($\sigma_{R/}\ \sigma_D$) is ploted in Fig. 5-7 as a function of time. As seen, the effect of the mutual repulsion over the diffusion increases slightly as the collection time decreases. At relatively short collection time, the mutual repulsion makes an instantaneous effect on the generated electron cloud by spreading the electrons away from each others. The effect of the repulsion decreases with long drift times since the electrons are relatively apart from each other.The diffuion on the contrary keeps expanding the cloud steadily since it is independent on the amount of electrons in the cloud. The charge expansion is however limited in the crystal structure due to the scattering mechansims.

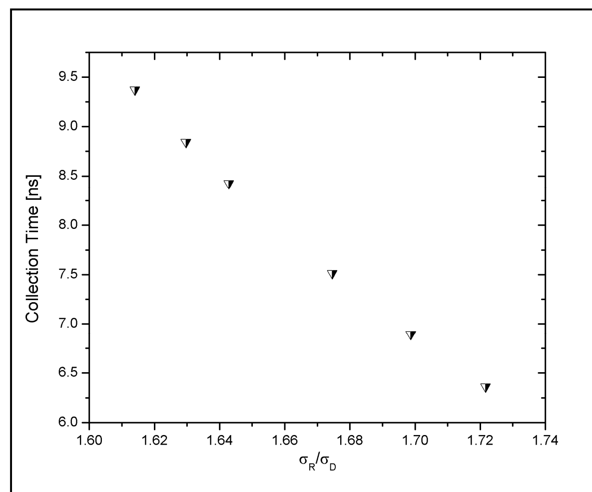

Fig.5-7: The ratio of the mutual repulsion to the diffusion in the charge cloud.

The measurement and the analysis above were for the impinging photon energy of 12.14 keV. Following the analysis in chapter 3, the fitting curve can be generalized for any deposited photon above the k-edge of silicon and for the photoelectric energy range of the detector as follows:

$$\sigma_{Tot}(t) = \sqrt{\left(10.196\left[\frac{\mu m^2}{ns}\right] * t\right) + \left(0.253\left[\frac{\mu m^2}{ns^{2/3}}\right] * \left[\frac{E * t}{w}\right]^{2/3}\right)} \qquad (5\text{-}5)$$

where E is the photon energy in eV and w is the ion pair ionization energy in unit of eV. This allows a prediction of the intrinsic resolution of Si detectors in general.

For example, the electron cloud generated from a 2000 eV photon will have within 3ns collection time a radius of:

$$\sigma_{Tot}(t = 8.0\ ns) = \sqrt{\left(10.196\frac{\mu m^2}{ns} * 3.0\ ns\right) + \left(0.253\frac{\mu m^2}{ns^{\frac{2}{3}}} * \left[\frac{2000\ eV}{3.7\ eV}3.0\ ns\right]^{\frac{2}{3}}\right)}$$

$$\sigma_{Tot} = \sqrt{30.588\ \mu m^2 + 34.921\ \mu m^2} = 8.094\ \mu m$$

The influence of the electrostatic repulsion on the radius of the electron cloud within this collection time is $\sigma_R = 5.91\ \mu m$ and the one from the diffusion is $\sigma_D = 5.53\ \mu m$.

Figure 5-8 employs Eq. 5-5 for different photon energies by using 3.7 eV for the ion pair ionization energy.

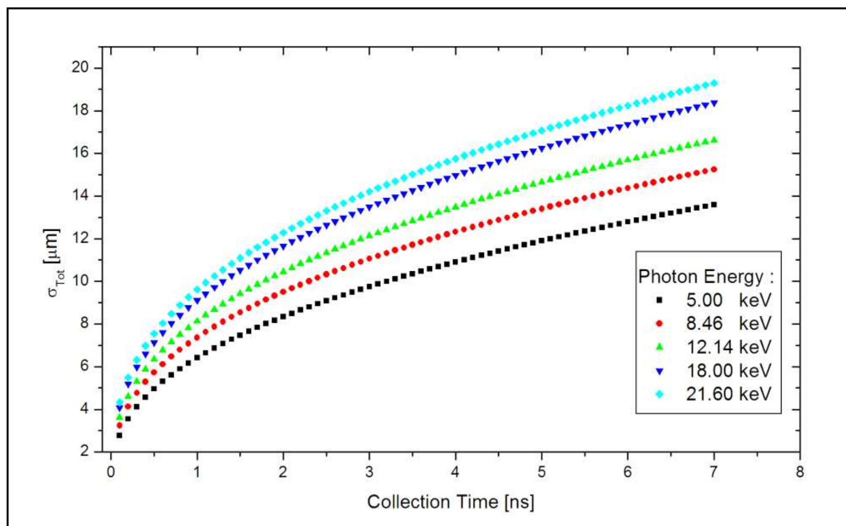

Fig.5-8: Prediction of the total radius of the charge cloud as a function of the collection time reference to Eq. 5-5 by using different photon energies.

B-2 Measurement with 30° Inclined X-ray Beam

The angle of the inclined X-ray track was set to 30° in this measurement. The projected pixels of the detector array are consequently reduced compared with the previous measurement in section B-1. The generated electron clouds are collected mainly in four pixels as depicted in Fig. 5-9. The intensity image (B) is the measurement output. The simulation model in (A) illustrates the distribution of the charges in a grid of $1\mu m$ cell size. Therefore the majority of the charges are accumulated in Pixel 1 and drops linearly as seen in the surface plot (C). The measurement was performed with an integration time of 2 minutes and $5\mu m$ step per position. The photon energy is kept the same, 12.14 keV. The normalized scan profiles in the projected pixels are shown in Fig.5-10.

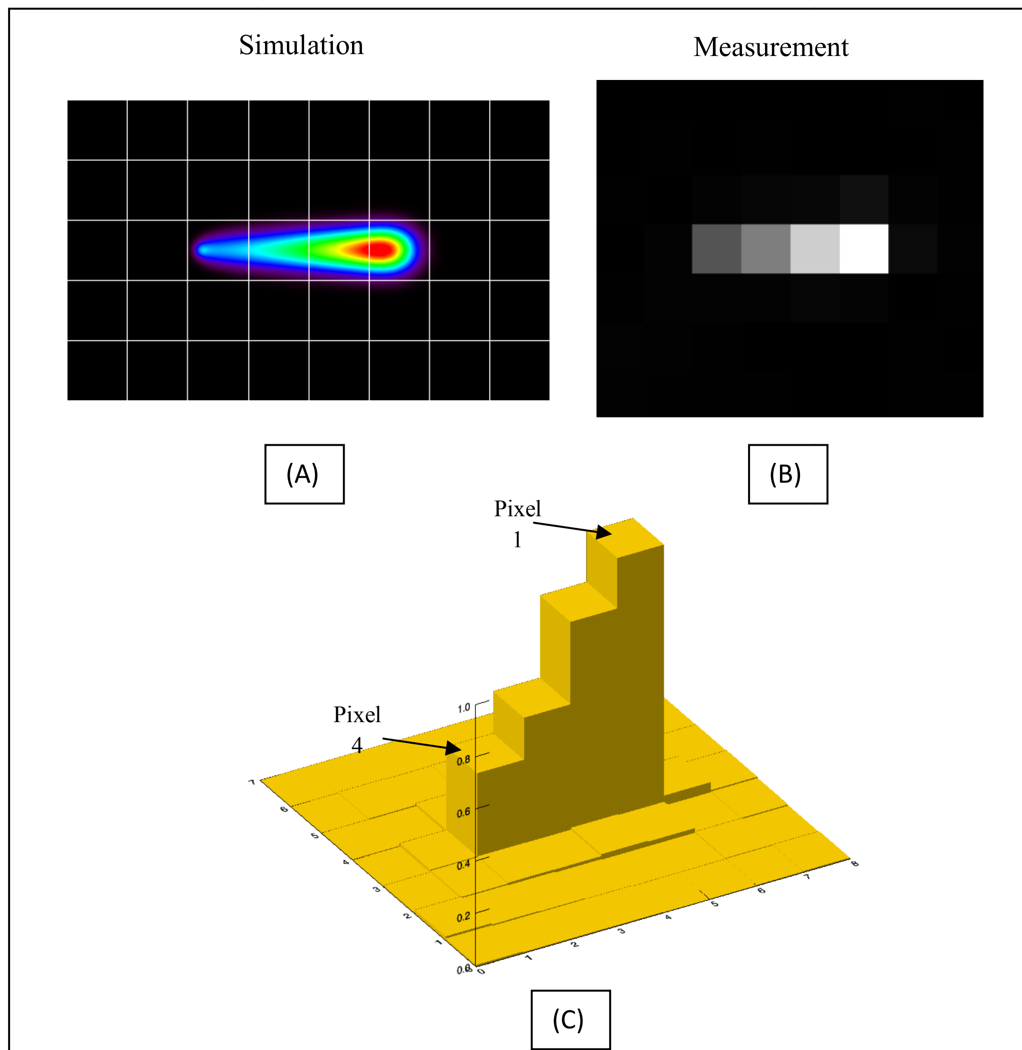

Fig.5-9: Images resulting from the simulated data (A) and measured data (B) for the inclined beam track of 30°.The white grid in image (A) has pixel size of 75 µm laid over a matrix of 1 µm cell size.

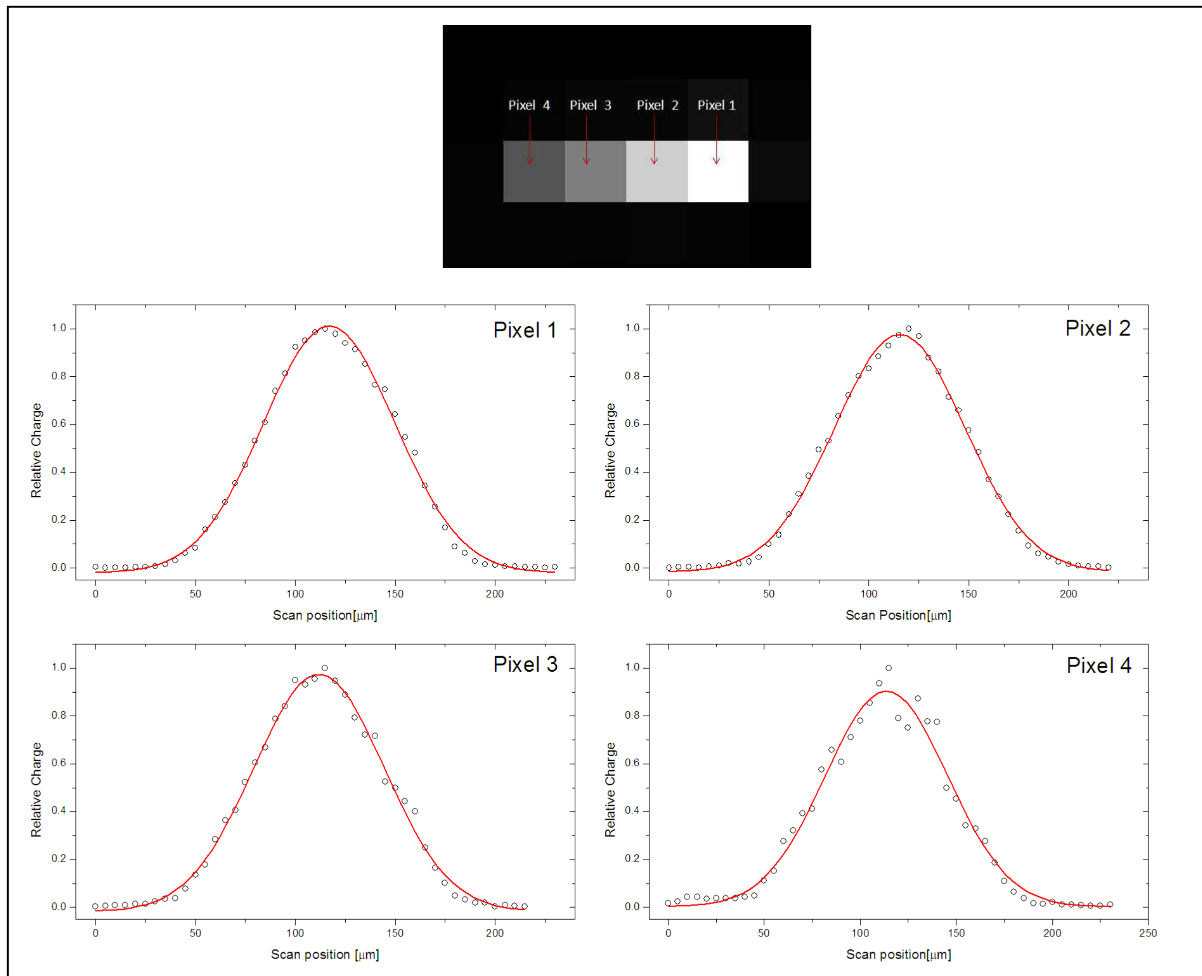

Fig.5-10: The scan profiles which result from the 30° inclined X-ray beam.

The radius of the charge cloud in each pixel is determined from the scan profile as described in Fig5-5. The resulting RMS values are shown in table 5-4 with the error resulting from the applied Gaussian fit on the differentiated profile. The corresponding time for each radius is calculated as shown in Fig.5-6 (A).

Table 5-4: The resulting RMS radii of the electron clouds for the 30° X-ray track

Pixel No.	Sigma [μm]	Error[μm]	Calculated Collection Time [ns]
1	18.644	0.22	9.424
2	18.521	0.16	9.286
3	18.253	0.17	8.941
4	17.086	0.18	7.465

The RMS values are plotted against the calculated collection time as shown in Fig.5-11 and the fitting line is applied on the data as described in Eq.5-3. The resulting fitting equation is:

$$\sigma_{Tot}(t) = \sqrt{8.769 \left[\frac{\mu m^2}{ns}\right] * t + 59.257 \left[\frac{\mu m^2}{ns^{2/3}}\right] * t^{2/3}} \quad (5\text{-}6)$$

The error in $\overline{P_1}$ is 1.071 $\mu m^2/ns$ and in $\overline{P_2}$ is 2.213$\mu m^2/ns^{2/3}$.

For example, if the radius of the charge cloud for 8.0 ns collection time is recalculated:

$$\sigma_{Tot}(t = 8.0\, ns) = \sqrt{\left(8.769 \frac{\mu m^2}{ns} * 8.0\, ns\right) + \left(59.257 \frac{\mu m^2}{ns^{\frac{2}{3}}} * [8.0\, ns]^{\frac{2}{3}}\right)}$$

$$\sigma_{Tot} = \sqrt{70.15\, \mu m^2 + 237.03\, \mu m^2} = 17.53\, \mu m$$

Therefore, the final results of σ_{Tot} is roughly the same as the calculation shown in the previous section.

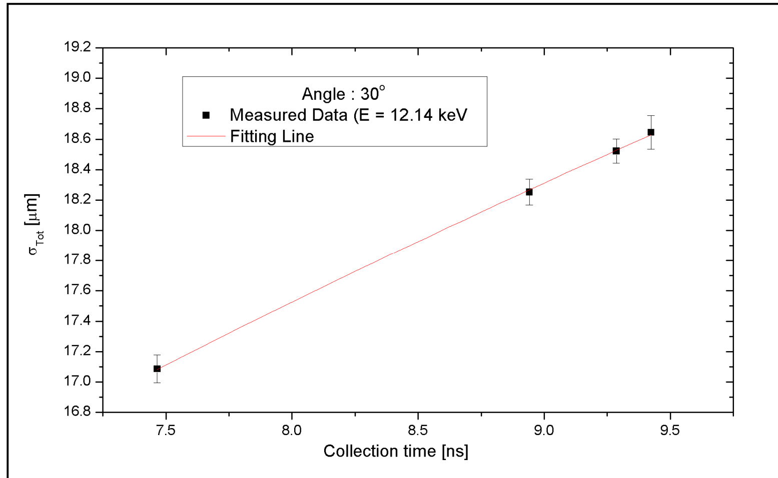

Fig.5-11: The RMS values resulting from the X-ray track of 30° and the best fitting line.

The RMS values resulting from the measurement with 30° and 40° X-ray tracks are plotted as shown in Fig. 5-12. The best fit for the data fulfills the following equation:

$$\sigma_{Tot}(t) = \sqrt{10.617 \left[\frac{\mu m^2}{ns}\right] * t + 55.274 \left[\frac{\mu m^2}{ns^{2/3}}\right] * t^{2/3}} \quad (5\text{-}6)$$

The error in $\overline{P_1}$ is 1.001 $\mu m^2/ns$ and in $\overline{P_2}$ is 2.028$\mu m^2/ns^{2/3}$. This shows that the expected behaviour of the contributions is independent of the incident angle.

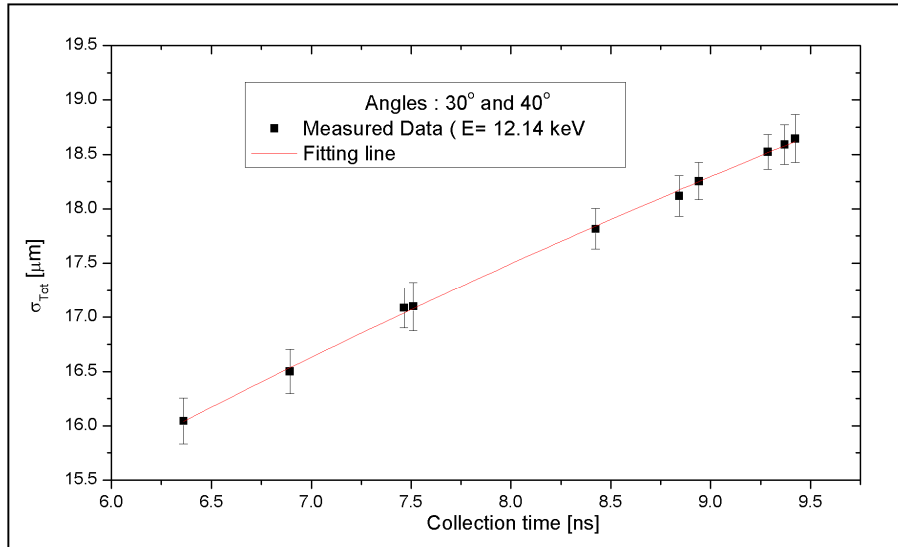

Fig.5-12: The measured RMS values of the electron clouds resulting from the measurement of both 30^0 and 40° X-ray tracks.

The last measurement performed with the X-ray track of 0° which is the direction parallel to line normal to the detector surface. The scan was performed with a $5\mu m$ step per scan position and 2 minutes integration time. The scan profile is illustrated in Fig. 5-13 (A) and its derivative in (B). The RMS radius of the charge cloud (σ_0) is 18.581 μm.

The values of the projected pixels in the measurement of 30° X-ray track are summed up in the direction parallel to the projection (line direction in the detector array) and plotted against the scan position as shown in Fig 5-13(C).The derivative of the scan profile in (C) is depicted in (D). The RMS radius of the charge cloud ($\sigma_{||}$) is 19.163 μm.The difference between σ_0 and $\sigma_{||}$ is 0.582 μm.

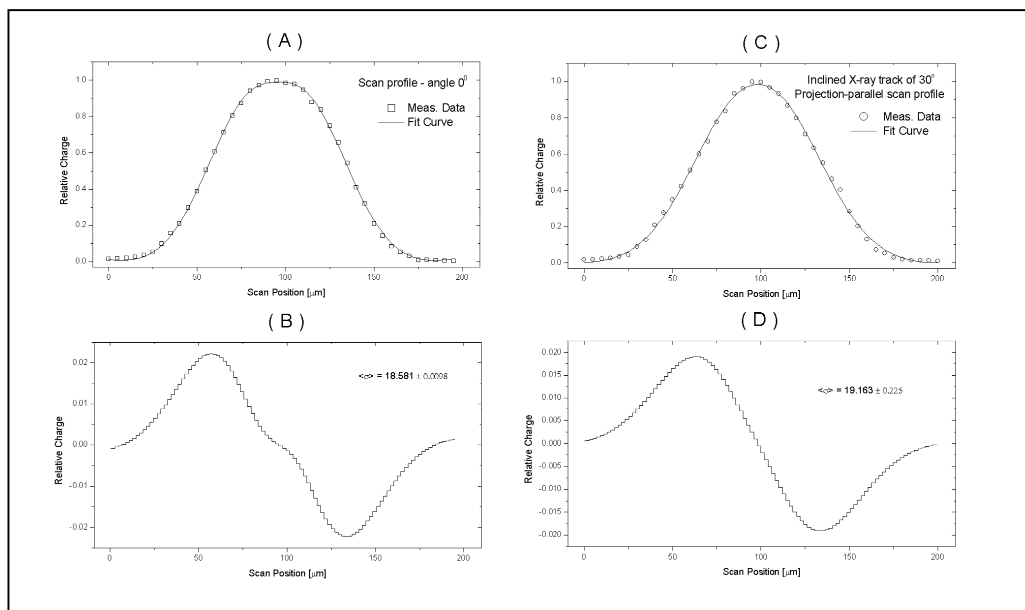

Fig.5-13: A compression of the scan profiles for the X-ray tracks of 0° (A) and 30° (C). The derivative of the scan profile in (A) is depicted in (B) and the one for (C) is plotted in (D).

C. Perpendicular Beam Incidence: Charge Cloud Size as a Function of Photon Energy

It was shown in the previous sections that for the inclined X-ray beam of 12.14 keV photons, the influence of the mutual electrostatic repulsion prevails the diffusion effect on the measured electron clouds at any depth within a definite collection time period. However, the influence of the electrostatic repulsion is dependent on the number of generated electrons. In this section, a selected photon energies between 5.0 keV and 21.6 keV (Fig.5-1: A, B, D, and E) were used to study the relation between the size of the electron clouds and the photon energy. These measurements have been performed for perpendicular beam incidence ($\theta = 0^o$).

The first harmonic energy peak is considered in the data analysis for each measurement. The detector and the experimental parameters which were used in the measurements are shown in table5-5.

In the measurements, the detector back side was exposed to a collimated X-ray beam falling perpendicular on its surface. Therefore, the electron clouds which are generated along the X-ray track from the different depths are collected and distributed over the pixel array of which the center of the distribution is the same for all clouds and it is corresponding to the position of the incoming beam.

A successive scan was performed for a number of pixels as depicted in Fig 5-14. Two independent scans were performed. One scan was carried along the line direction of the detector array and another one in the charge transfer direction. The resulting scan profile includes two edge profiles since the scan crosses the pixel boarders two times.

The scan profiles in Fig.5-14 are analyzed by applying energy threshold on a region of 3x3 around the central pixel in the corrected signal frames. The thresholds have minimum and maximum values which are corresponding to the upper and lower limits of the first harmonic peak. Since the electrons spread between a number of pixels, the sum of the pixel values in the ROI is compared with the energy limits.

Table 5-5: The detector and the experimental parameters for the measurements of the electron clouds in energy range 5-21.6 keV.

Parameter	Value
Back voltage	-230 V
Registers voltage	-17 V
Operating temperature	-80 ^{o}C
Operating pressure	$3.9*10^{-7}$ mbar
Integration time	2-4 minutes
Maximum collection time	~ 3 ns
Scan step	5 µm

Figures 5-15 (A-E) shows the resulting scan profiles and their derivatives for the photon energies used. Since the response of the pixels is symmetric, the scan profiles are obtained by overlapping the scan profiles of all pixels involved in the scan.

Qualitatively, the scan profiles show that the width of the profile's plateau decrease relatively with increasing the photon energy. Therefore, the electron clouds are more shared with the neighboring pixels as the photon energy increases. The distance between the centers of the rising and the falling edges equals the pixel size in all profiles.

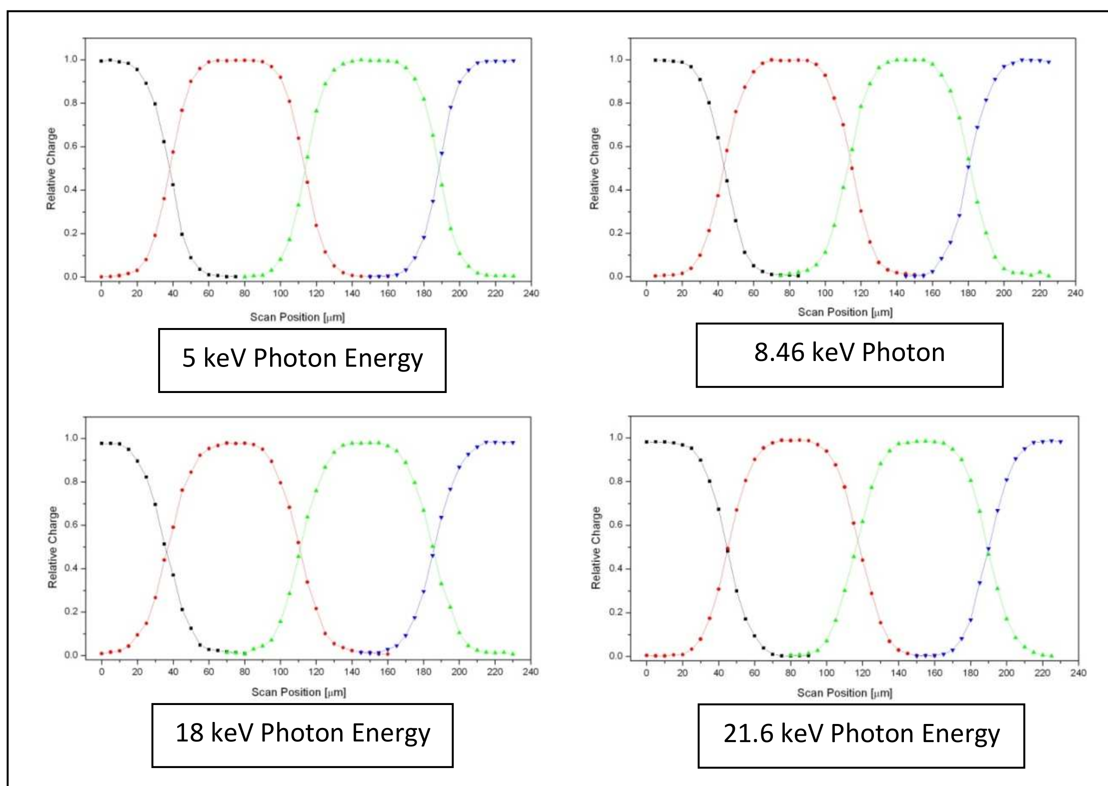

Fig.5-14: Scan carried out on three pixels for different incident photon energy. The drawn lines are only guiding lines.

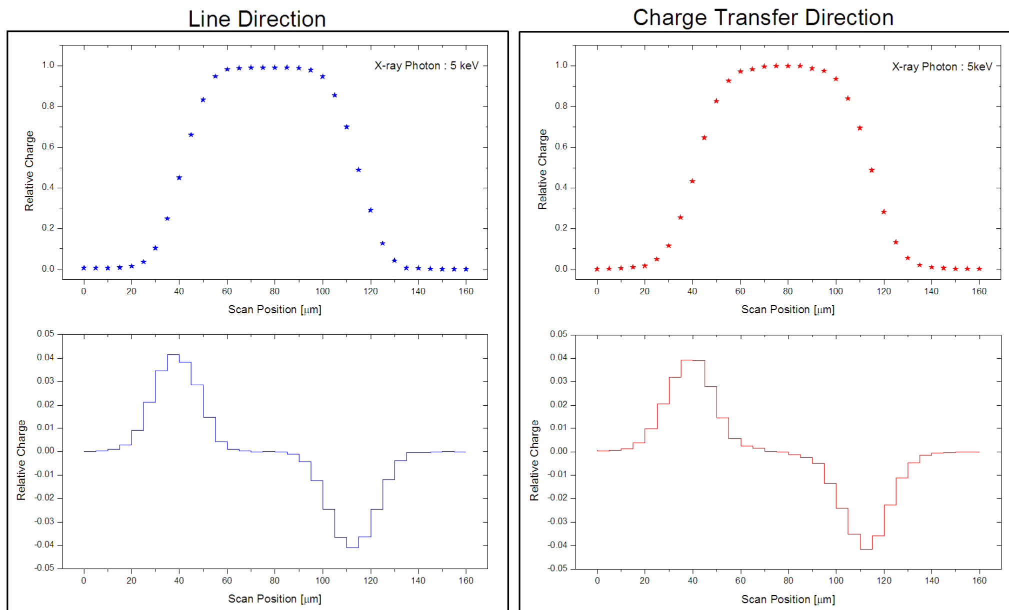

Figure 5-15(A): X-ray photon for 5 keV. Upper plots are the measured scan profiles and the lower graphs are the differentiation of the scan profiles.

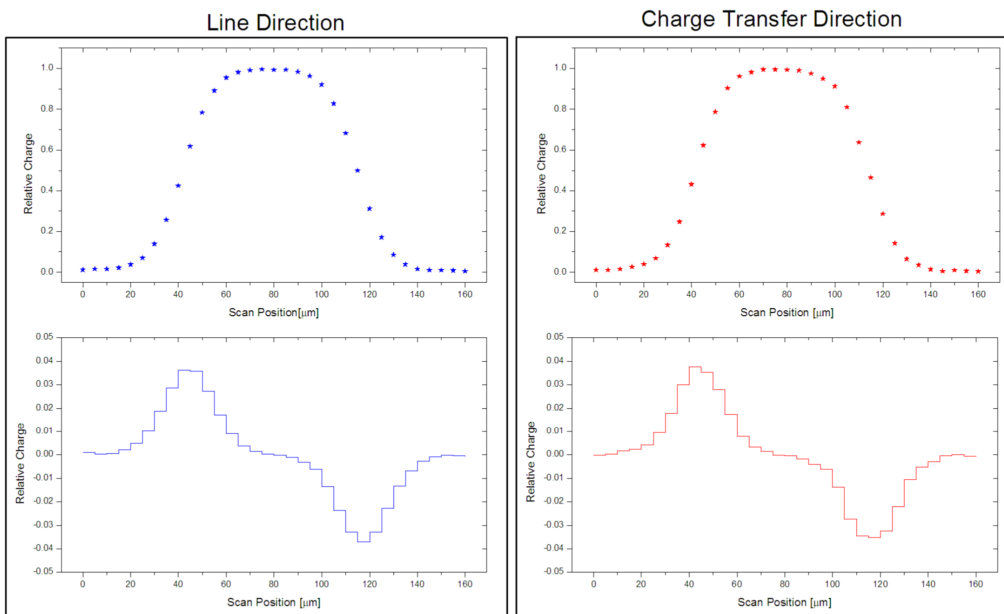

Figure 5-15(B): X-ray photon for 8.46 keV. Upper plots are the measured scan profiles and the lower graphs are the differentiation of the scan profiles.

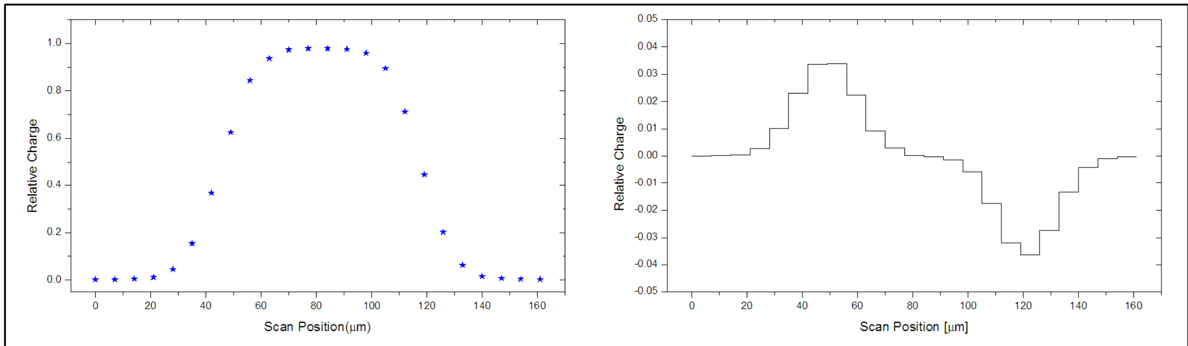

Figure 5-15(C): X-ray photon for 12 keV. Left graph is the measured scan profiles with 7 μm scan step and right is the differentiation of the scan profiles.

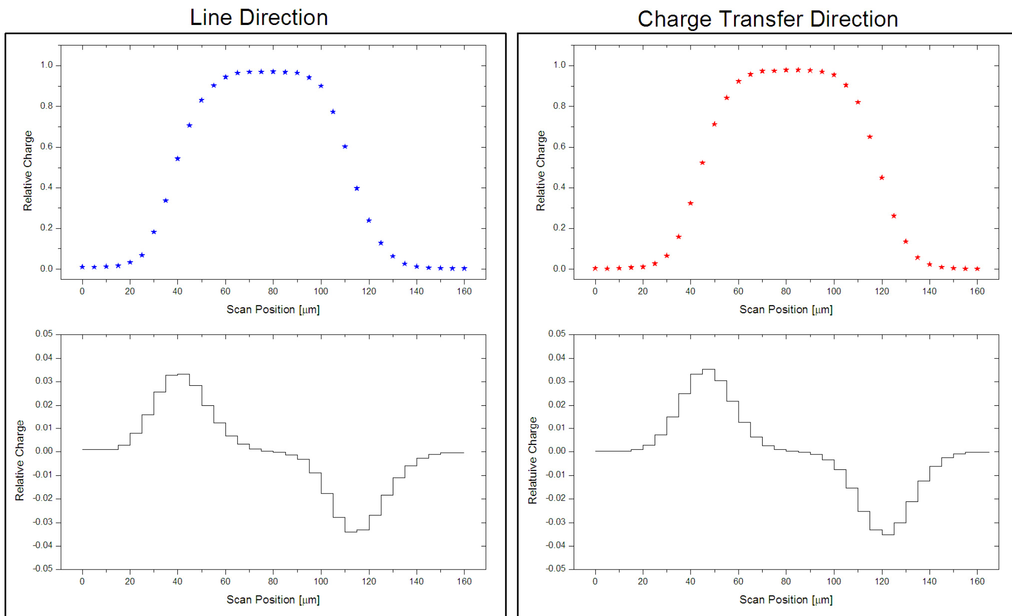

Figure 5-15(D): X-ray photon for 18 keV. Upper plots are the measured scan profiles and the lower graphs are the differentiation of the scan profiles.

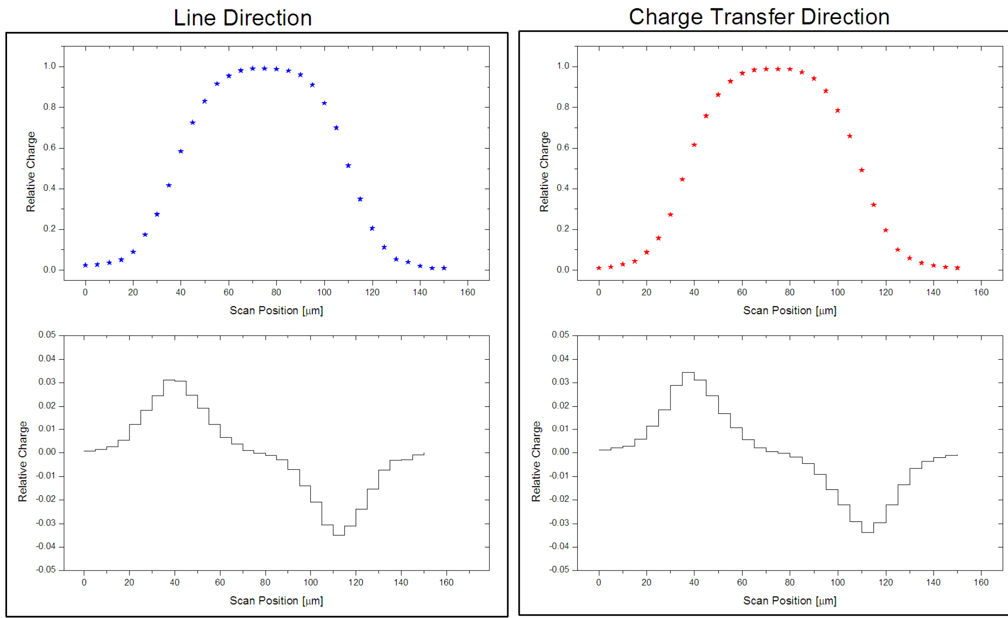

Figure 5-15(E): X-ray photon for 21.6 keV. Upper plots are the measured scan profiles and the lower graphs are the differentiation of the scan profiles.

Table 5-6 shows the RMS radii of the measured clouds for the scans in the line direction and the charge transfer direction. The average values for both scans are given in Table 5-6 and plotted against the photon energies as depicted in Fig. 5-16 (A) and compared with the simulated values in (B) of the same figure. It is noticed that the total width $\bar{\sigma}$ increases only slightly from E = 5keV to 21.6keV although the total charge changes by a factor of 4. Following Eq. 5-5, this increase in charge should increase the variance of the contribution of the repulsion term by $[4]^{2/3} = 2.5$. In comparison, the increase is found to be only 55%. The explanation is found by a more detailed analysis. The attenuation length of the 5 keV photons is maximum 120 μm in comparison with the whole bulk length for the 21.6 keV, Fig.3-3.

Table 5-6: The RMS values for the charge clouds and the corresponding photon energies.

X-ray Energy (keV)	$\bar{\sigma}_X$ Line Direction (μm)	$\bar{\sigma}_Y$ Charge Transfer Direction (μm)	$\bar{\sigma}$ (μm)	Error (μm)
5.0	9.54	9.53	9.535	0.28
8.46	10.49	10.24	10.365	0.32
12.0	10.76	-	10.760	0.27
18.0	11.19	10.98	11.085	0.31
21.6	11.88	11.41	11.645	0.39

Therefore, the PSF of the 5 keV electron clouds are weighted over almost the same cloud size within the 3ns collection time. On the other hand, the PSF of the 21.6 keV are weighted over the electron clouds coming from different conversion positions along the detector length

The experimental values now represent a weighted quadratic sum of the deposited energy in depth and are fitted with a simplified function representing both major contributions, the diffusion and the repulsion, (Fig.5-16 [A]). The measured data is compared with the simulated data as depicted in Fig.5-16 [B].

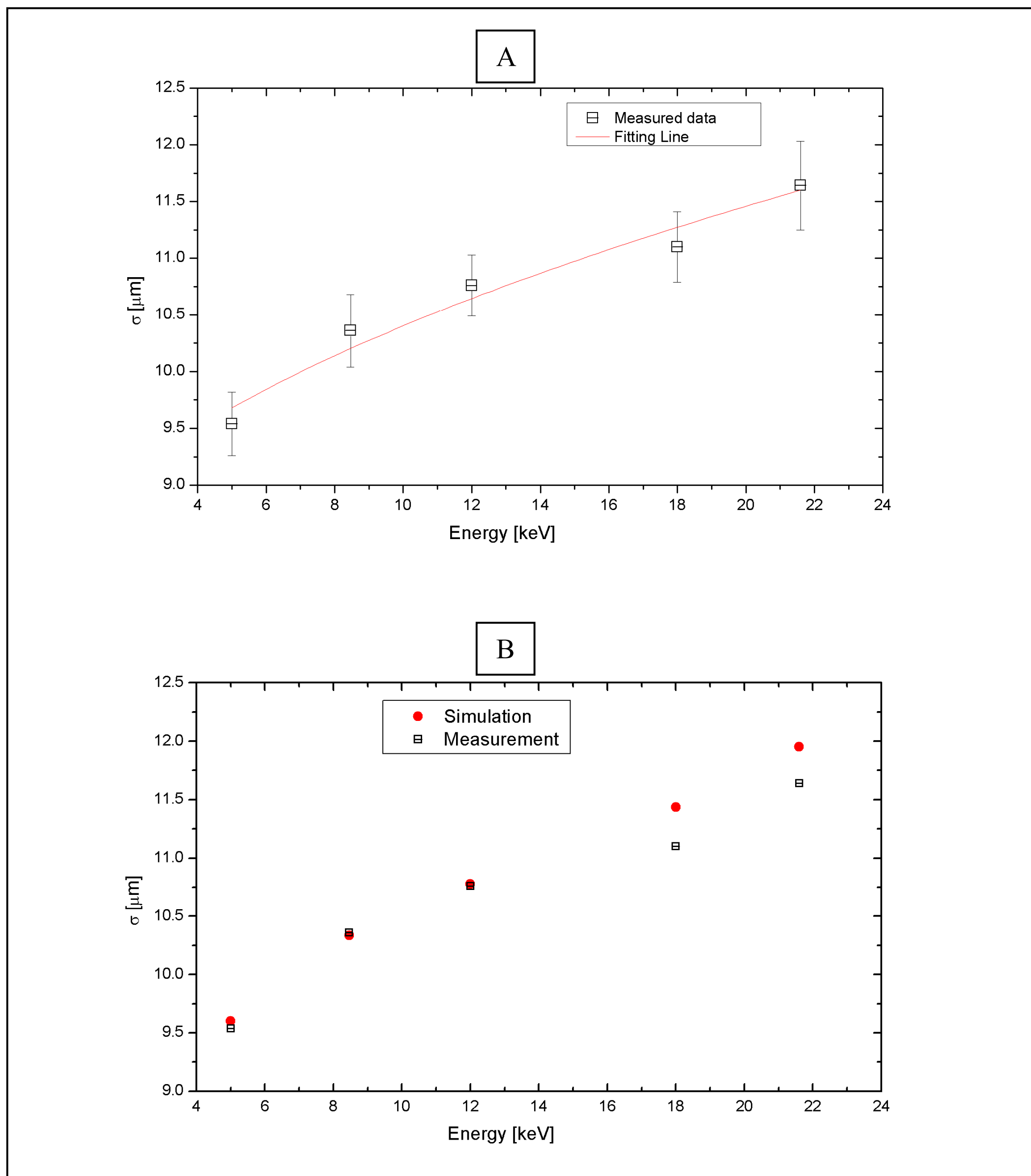

Fig.5-16: (A) The measured RMS radii of the charge clouds versus the corresponding photon energy.(B) The measured RMS radii and the simulated ones.

The maximum radius of the electron cloud can be extracted from Fig. 5-8 for an electron clouds drift the whole detector depth (collection time = 3ns). Table 5-7 shows the RMS and the maximum values as a function of energy. The difference between the mean and maximum values increases with increasing the attenuation length in silicon. Figure 5-17 shows the plot of the RMS and the maximum values of the electron clouds.

Table 5-7: The RMS and the maximum radius of the electron clouds in the energy range 5-21.6 keV.

X-ray Energy (keV)	RMS (µm)	$\sigma_{max}(t = 3ns)$ (µm)	Difference (µm)
5.0	9.535	9.750	0.215
8.46	10.365	11.051	0.686
12.0	10.760	12.127	1.367
18.0	11.085	13.492	2.407
21.6	11.645	14.199	2.554

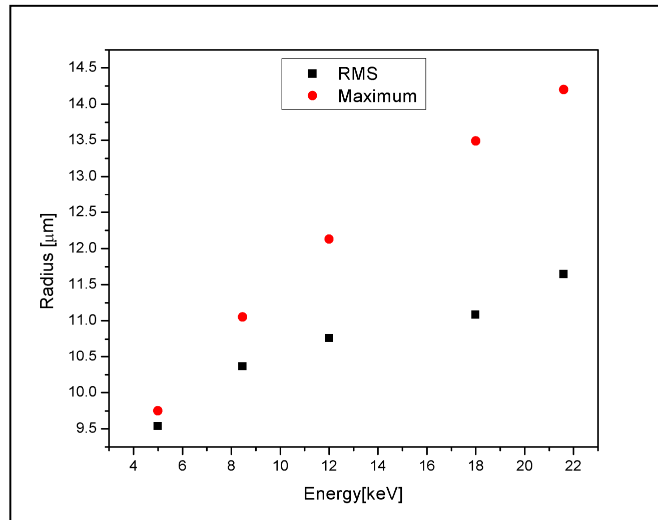

Fig.5-17: Plot for the RMS and the maximum radius of the electron cloud in the energy range 5-21.6 keV.

D. Experimental Challenges

C.1- Off Center Hit

One of the challenges faced during the trials to measure the charge cloud size was the mechanical vibrations resulting from the beats delivered to the detector from the cooling pump. The 2Hz frequency vibration even magnified when the detector situated on the top of the stepping motor as shown in Fig 5-18 (A). The setup is modified later on to decouple this disturbance by overlaying the detector on two scanning motors as depicted in Fig 5-18 (B).

The vibration caused the charge clouds not to be located in one position rather oscillating along the direction of propagation, Fig.5-19. The charges thus are smeared and spread into a number of pixels which worsen the position resolution. The resulting scan profile is affected and the cloud size appeared bigger than the actual size. Figure 5-20 illustrate the difference between two separate measurements; one measurement in the charge transfer direction (left) and another measurement in the line direction (right). The measurements performed with X-ray energy of 12.0 keV and 7 μm scan steps. The applied temperature was 193 K and the depletion voltage was -230V. The RMS radius of the charge cloud in the charge transfer direction is 15.46 μm and in the line direction is 10.76 μm.

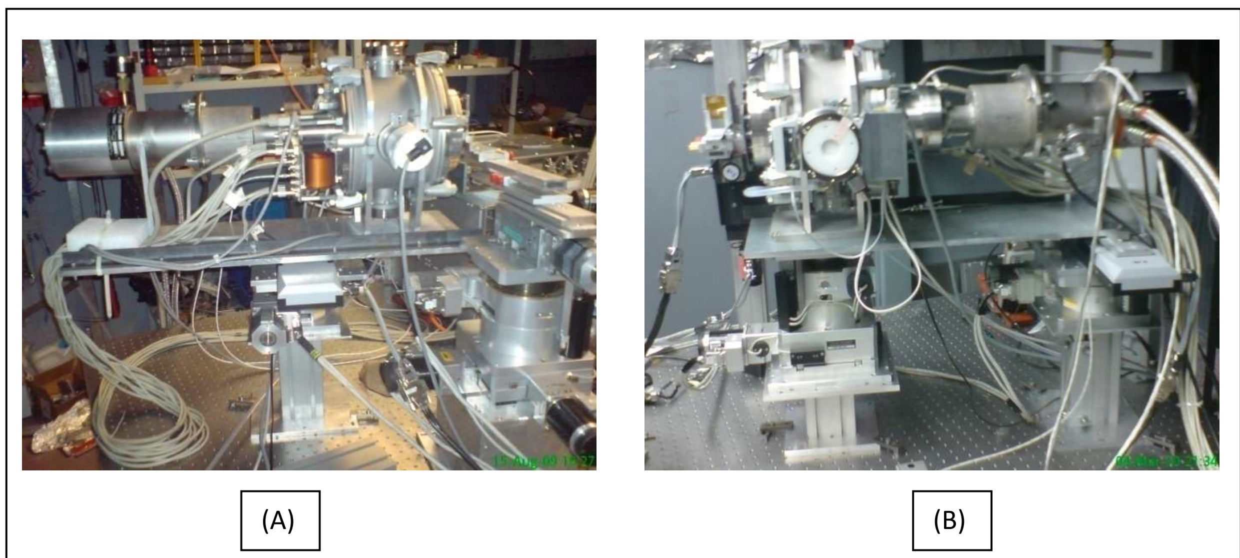

Fig.5-18: Two different experimental setups: (A) The detector is placed on the top of one stepping motor and (B) the detector on the top of two motors. The image from the EDR Beamline in BESSY-Berlin

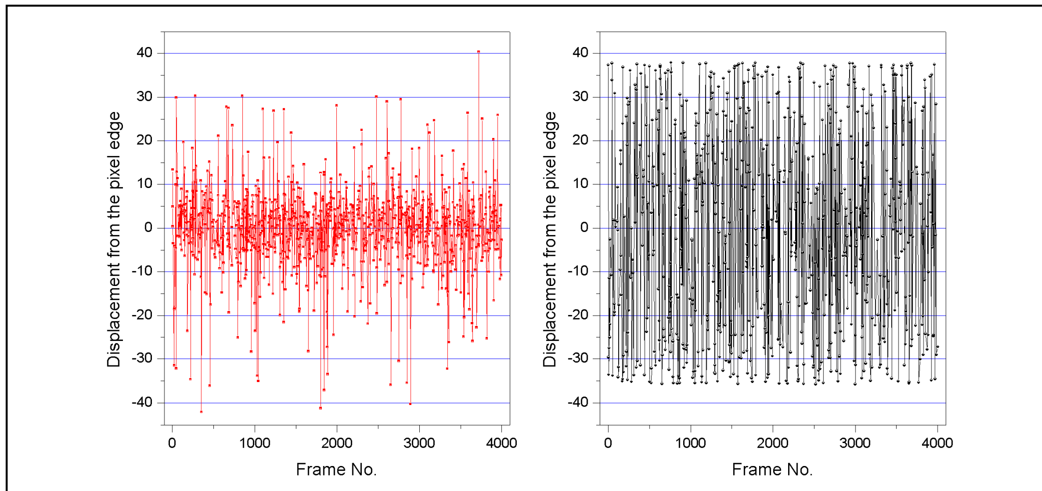

Fig.5-19: The effect of the oscillations delivered to the detector from the cooling pump. The measurement was taken at the edge between two pixels and the data in the plots are the center of mass of the double split events. Left, there are no oscillations. Right, with oscillations.

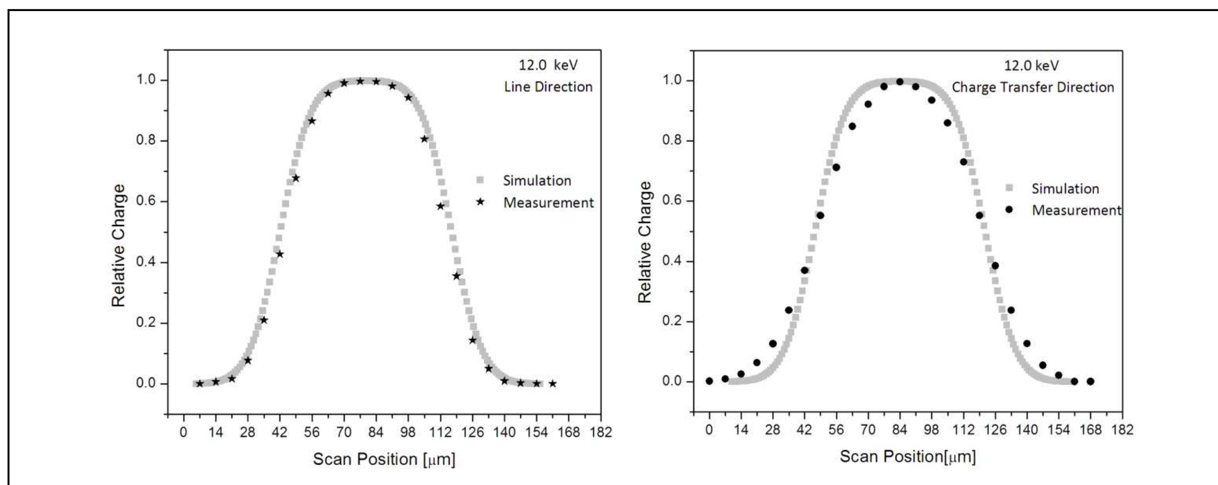

Fig.5-20: Scan profiles using X-ray energy of 12.0 keV: (left) the measurement in the line direction which is close to the simulated profile. (Right) the measurement in the charge transfer direction which is strongly affected with the mechanical vibration in its direction.

As an approach to correct for this effect via the software, the measured data can be de-convolution with a mathematical model considering the vibration behavior. The measured data indicates that the hit location is not localized; therefore the periodic time of the oscillation is very short. The displacement from the mean location in a time (t) can be described mathematically by a sinusoidal function:

$$Y(t) = A \sin \omega t \quad (1)$$

where A is the impulse amplitude and ω is the uniform angular velocity. The rate of change of the displacement is:

$$V(t) = \frac{\Delta Y}{\Delta t} = A\omega \cos \omega t \quad (2)$$

Using the identity $sin^2\omega t + cos^2\omega t = 1$, Eq.1 gives

$$cos\omega t = \sqrt{1 - \left[\frac{Y(t)}{A}\right]^2} \quad (3)$$

Substituting Eq.3 in Eq. 2 gives

$$\Delta t = \frac{\Delta Y}{A\omega\sqrt{1-\left[\frac{Y(t)}{A}\right]^2}} \quad (4)$$

This function may be drawn in one dimension array and convoluted with the simulated Gaussian distribution resulting in new Gaussian distribution with degraded resolution as depicted in Fig. 5-21. If the scan is carried over the degraded Gaussian distribution, the resulting scan profile will match the measured one as illustrated in Fig.5-21(D) when the amplitude A in equation (4) equals18 μm.

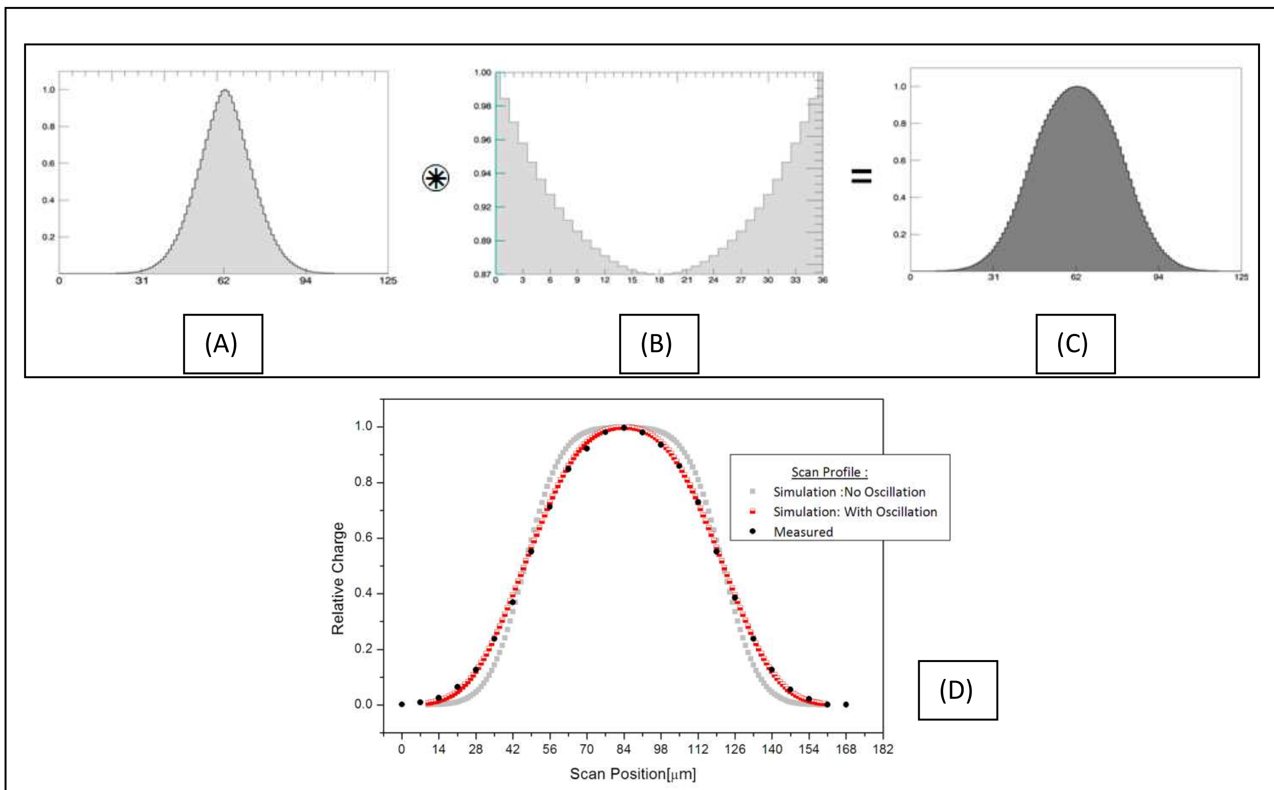

Fig.5-21: Simulation output for the convolution process of Gaussian distribution related to the charge cloud size generated from x-ray photons of 12.0 keV. (A) Input Gaussian distribution [FWHM=25.072μm], (B) normalized model of Equation 4[Y-axis is Δt, X-axis is Y(t) and A equals18 μm] and (C)is the degraded Gaussian distribution [FWHM = 36.91μm]. The scan profiles are compared in (D): No oscillation related to the Gaussian distribution in (A) and with oscillation is for (B) and the measured profile as in Fig.5-9(left).

C.2- Charge Cloud Size for the Piled up Photons

The energy spectrum depicted in Fig. 5-1-A shows different reflected energy peaks from the monochromator in addition to the peaks of pile up events. The event rate per frame in this experiment is 0.6. The strong pileup events at 30 keV are possibly from the strong reflection of 15 keV photons. The resulting charge cloud size of such an event depends on the way they interacted between each other during the drift to the potential minimum and the numerical model cannot explain this complex behavior. The RMS values are presented in Table 5-8. They show an improved in the spatial resolution by 9% compare to the simulated values. Although these values are in the expected spatial resolution range, the effect has no clear explanation.

It is known that the hole current is moving towards the back side with a velocity three time slower than the electron's one. This current might cause the charge cloud to experience less expansion and shrink consequently in size provided that in the experiment the X-ray track is the same for all detected photons. Another possible explanation might be due to the polarization of the reflected beam which may affect the shape of the initial electron cloud. The detection of X-ray polarization with a charge couple device has been experimentally performed [ref.15] and showed that the primary charge cloud size can reflect the polarization vector of the incident x-ray.

Table 5-8: Measured RMS radii for the 3rd, 4th harmonic reflections and the strong pileup at 30keV as depicted in Fig. 5-1(A)

X-ray Energy (keV)	RMS_X Line Direction (µm)	RMS_Y Charge Transfer Direction (µm)
15.0	8.96	9.90
20.0	10.95	10.49
30.0	10.48	10.17

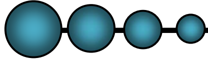

6. Conclusions and Outlook

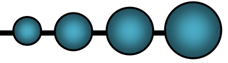

The spatial response of the fully depleted pnCCD detector of thickness 450μm and pixel size of 75μm*75μm is quantified as a function of the incident angle of the X-ray beam for a selected photon energy from the range [5.0-21.6] keV. The energy resolution of the detector is also determined according to the photon energy.

The measurements of the inclined X-ray track of 40°, 30° and 0° of the 12.14 keV photons give the following conclusions:

1. The charge distribution in the pixel array of the detector is proportional to the incident angle (θ). The projected length L is $= L_{\perp} * \tan\theta$, where $L_{\perp}$ is the thickness of the detector. The number of the collected charges in the projected pixels falls linearly with the distance away from the central pixel (the pixel that meet the crossing point of the incoming beam and the vector normal to the surface) due to the exponential behavior of the photon absorption at this energy.
2. The RMS radius of the electron cloud reduces as the interaction position of the photon gets closer to the pixel array. For a given collection time (t), the electron cloud radius is determined as follows :

$$\text{Radius}(t) = \sqrt{10.617 \left[\frac{\mu m^2}{ns}\right] * t \ + \ 55.274 \left[\frac{\mu m^2}{ns^{2/3}}\right] * t^{2/3}}$$

   A maximum difference of 2.544 μm in the radius [Table 5-2] is found when the incident angle is 40° and 1.558 μm [Table 5-4] when the incident angle is 30°.
3. The mutual electrostatic repulsion dominates the cloud expansion over the diffusion at any collection time less than 5.8ns [Figure 5-7].
4. The results show that the cloud expansion is dependent on the applied depletion voltage. The cloud size is increased due to the long collection time.

The relation between the photon energy and the size of the electron cloud was studied with a perpendicular beam direction with respect to the back surface of the detector. The following results are obtained:

1) The RMS radius of the electron clouds varies from 9.535µm to11.645µm in the energy range [5.0-21.6] keV and collection time of ~3ns. Therefore, the average position resolution of 10.6µm can be used to determine the interaction position of the photons in this energy range.
2) The spatial resolution of the detector in this energy range is 25µm which covers 1/3 the pixel size.

The measured energy resolution confirms that the noise level in the detector is low. The measured energy resolution is essentially dependent on the number of the generated electron. The energy resolution for 5 keV and 21.6 keV photopeaks are 147 eV and 284 eV respectively. The following formula can be used to determine the energy resolution (FWHM) of the detector at a given photon energy (E):

$$FWHM\ (eV) = 2.356 * \sqrt{0.686\ eV * E + 617.77\ eV^2}$$

The numerical models are confirmed by the experimental results. They explain the physical processes which are occurred in the detector depending on the electron mobility, the electric field, the device temperature, the deposited energy and the incident angle. The simulation model which describes the distribution of the charge clouds due to the inclined incident angle shows that the image formed in the detector array are affected by the pixel size. The simulation shows the comet-like structure in a fine grid of cell size 1/75 the pixel size of the detector and this structure cannot be seen in the pixels of the detector. The maximum deviation of 5% between the measured and the simulated charge cloud size is obtained. The models can be used to estimate the spatial resolution for different detector and experimental parameters.

The results of this thesis are beneficial for detector development and image processing:

I. The pixel can be designed three times less than the actual size without losing the spatial resolution of the detector in the energy range studied.
II. The digital images formed by the detector can be spatially enhanced to resolve finer structures by utilizing sub-pixel resolution analysis. As an example, the center of mass of the events can be determined from the pixels indices and then the data can be reconstructed in a new 2D array of finer pixel size.
III. The original size of the object can be obtained by the deconvolution method. The simulation models proposed in this thesis can be used as a deconvolution kernel in the analysis. Parallax effect in the images can be corrected as well by the same method.

IV. The pattern of the split events, mainly the rejected events in the measurements, can be further studied according to the incident angle of the beam and the detector depth. The simulation models can be modified to produce images in three dimensions for different possible patterns. This may help to get as much information as possible from the measurements.

References

[1] L. Strüder, P. Holl and G. Lutz, "Device modeling of fully depletable CCDs", Nucl. Instr. And Meth. A253:386-392,1987.

[2] E. Gatti and P. Rehak ,in Proc. 2nd Pisa Meeting on Advanced Detectors,Grosetto, Italy(1983) Nucl.Inst. and Meth. 225 (1984)608-614.

[3] L. Strüder, P. Holl and G. Lutz, "Development of fully depletable CCDs for high energy physics applications", Nucl. Instr. And Meth. A257:594-602,1987.

[4] N. Kimmel , "Analysis of the charge collection process in solid state X-ray detectors", PhD dissertation 2008, department of physics/University of Siegen.

[5] E. Pinotti et al. ,"The pn-CCD on-chip electronics". Nucl.Instr and Meth. A326:58-91,1993.

[6] S. Herrmann, W. Buttler, R. Hartmann, P. Holl, N. Meidinger, and L. Strüder ." Mixed signal pnCCD readout ASIC for the future X–ray astronomy mission eROSITA". Nucl.Sci. Symp. B 2007Conference Record, 3:2398–2403, 2008.

[7] R. Hartmann, W. Buttler, H. Gorke, S. Herrmann, P. Holl, N. Meidinger, H. Soltau,and L. Strüder." A high speed pnCCD detector system for optical applications". Nucl.Instr. and Meth. A 568:118–123, 2006.

[8] G. Lutz, "Semiconductor Radiation Devices", Springer verlag, Berlin/ Heidelberg/ New York, 2nd edition, 2001.

[9] Adir Bar-Lev, "Semiconductors and Electronic Devices", Prentice-Hall International, London, 1979.

[10] Thomas. L Floyd, "Electronic Devices", Pearson Education International, New Jersey, 2005.

[11] XCOM: Photon Cross Sections Database (http://physics.nist.gov/cgi-bin/Xcom/xcom2)

[12] Dr. Robert Hartman, Max-Plank Institute and the PN-sensor (München). Detector related technical discussion and manufacturing details.

[13] Joachim E. Trümper and Günther Hasinger, "The Universe in X-Rays", Springer-Verlag, Berlin/ Heidelberg, 2008. Section 7.3,"Fully Depleted Back-Illuminated pnCCDs" by L. Strüder and N.Meidinger.

[14] Andritschke R., Hartner G., Hartmann R., Meidinger N., Striider L., "Data Analysis for Characterizing pnCCDs**".** IEEE Nuclear Science Symposium Conference Record (2008).

[15] H. Tsunemi et al . " Detection of X-ray polarization with a charge coupled device". Nucl.Instr. and Meth. A321:629–631, 1992.

[16] Alig R. C.,Bloom S. And Struck C.W.,"Scattering by ionisation and phonon emission in semiconductors",Physics Reviw B, Vol.22(1980),P. 5565.

[17] Lechner P.,Hartmann R.,Soltau H.,Strüder, "Pair creation energy and Fano factor of silicon in the range of soft X-rays". Nucl.Instr and Meth. A377: 206-208,1996.

[18] Lowe B. G.,Sareen R. A.," A measurement of the electron-hole pair creation energy and the Fano factor in silicon 5.9 keV X-rays and their temperature dependence in the range 80-270K", Nucl.Instr and Meth. A576,2007.

[19] Selberherr Siegfried,"Analysis and simulation of semiconductor devices".Springer Verlag, Wien/New York,1984

[20] Canali C.,Majni G.,Minder R. and Ottaviani G., "Electron and hole drift velocity measurements in Silicon and their empirical relation to electric field and temperature".IEEE transactions on electrons devices ED-22,P:1045-1047,1975.

[**21**] Jacoboni C.,Canali C.,Ottaviani G. and Alberigi Quaranta A., "A review of some charge transport properties of silicon". Solid State Electronis,Vol22.P.77-89,1977.

[**22**] Arora N. D., Hauser J. R. , Roulston D. J., " Electron and Hole Mobilities in Silicon as a Function of Concentration and Temperature".IEEE Transactions on electron devices,vol. ED-29,P:292:295,1982.

[**23**] Grove A. S.:"Physics and Technology of semiconductor Devices". New Yourk:Wiley, 1967.

[**24**] Everhart T.E., Hoff P. H.,"Determination of Kilovolt Electron Energy dispersive vs Penetration Distance in Solid Materials", J. Appl. Phys. 42, 5837 (1971)

[**25**] Fitting H.J.,Glaefeke H., and Wild W.,"Electron penetration and energy transfer in solids",phys.Status Solidi A,v.43,p.185,1977.

[**26**] Hobbie R.K.,Roth B.J., "Intermediate physics for medicine and biology",Springer,4th edition,2007.

[**27**] Gatti E., Longoni A., Rehak P., and Sampietro M., "Dynamics of electrons in drift detectors", Nucl.Instr and Meth. A253.P: 393-399, 1987.

[**28**] Leitenberger W. et al ," Application of a pnCCD in X-ray diffraction: a three-dimensional X-ray detector". J. Synchrotron Rad. 15:P.449-457, 2008.

[**29**] Supplementary graphs from Wolfram Leitenberger : EDR Beamline-BESSY II .

[30] Spieler , Helmuth, " Semiconductor Detector Systems",Springer,1st edition,2005.

Acknowledgments

The track to reach to this page has been full of challenges, but this thesis would have not been successful without all the people who contributed in teaching and supporting me. To all of them my sincere and deep gratitude.

I would first like to thank my ‘doktorvater’ Prof. Dr. Albert Heinrich Walenta. It has been an invaluable opportunity for me to have my PhD with you. I have been inspired and enriched after every single discussion with you. I am deeply grateful for your constant support. It has been a privilege to be your student.

I would like to acknowledge the advice and the support from Prof. Dr. Ullrich Pietsch.

I am deeply indebted to Prof. Dr. Hans Dieter Dahmen. You always encouraged and supported me. I will never forget your exceptional and enjoyable physics lectures during my postgraduate study in the University of Siegen. Because of you, I was able to approach the oriental mind to the cultural values of life in Germany.

I would like to express my gratitude to Prof. Dr. Lothar Strüder for offering me the chance in the first half a year of my doctoral study to be at the MPI-HLL of the Max-Plank Institute in Munich, and to get the essential experience in dealing with the pnCCD detector.

Dr. Robert Hartmann, thank you very much for being kind and constructive with me during the time in MPI-HLL. I highly appreciate the time you dedicate to teach me and to build up my experience in handling the detector. The fruitful discussion with you and the technical support are pretty unique and considerable.

Dr. Werner Schenk, without you it would not have been the same! I deeply thank you for your guidance and generous support. I will never forget the endless discussion about science, and life! They sped up my work and made my steps successful.

I would like to thank Dr. Wolfram Leitenberger for the assistance in building the experimental setup and facilitating the required equipments during the experiments in the EDR-beamline of BESSY II.

Special thanks to Mr. Guido Schmidt and Mr. Rainer Neumann from the mechanical workshop for their help.

I would like to thank my colleagues Mrs. Andrea Brombach, Mr. Dieter Junge, Mr. Dieter Gebauer, Amgad Osman and Oliver Rübsamen for the friendship and all the support they gave me.

I would like to express my gratitude to my ex-colleagues Dr. Kivanc Nurdan and Dr. Tuba Conka Nurdan for their advices, guidance and encouragement.

Raffaellina mia … I've never got such a tasty Italian coffee before I met you. Together we walked high to our goals and we made it true. Let us enjoy the taste of the success and the coffee together again and again!!!

And last, but not least, to my parents, my sisters and my brothers. To say 'shokran jazelan' is not enough. You gave me the deep love and support that no grateful words can describe. I dedicate this thesis to all of you.